Rate-Dependent Adhesion and Friction in Gelatin

by

Wonhyeok Lee

A dissertation submitted in partial fulfillment of

the requirements for the degree of

Doctor of Philosophy

(Mechanical Engineering)

at the

UNIVERSITY OF WISCONSIN–MADISON

2025

Date of final oral examination: 07/28/2025

The dissertation is approved by the following members of the Final Oral Committee:

Melih Eriten, Professor, Mechanical Engineering

Dan Negrut, Professor, Mechanical Engineering

Christian Franck, Professor, Mechanical Engineering

Corinne Henak, Associate Professor, Mechanical Engineering

Alejandro Roldán Alzate, Associate Professor, Biomedical Engineering

ACKNOWLEDGMENTS

I would first like to express my deepest gratitude to my Ph.D. advisor, Dr. Melih Eriten, for his exceptional guidance throughout my research, career development, and personal growth. The achievements and knowledge I have gained during my Ph.D. at this great university are largely thanks to his support and mentorship.

I am also sincerely grateful to my defense committee members—Dr. Dan Negrut, Dr. Christian Franck, Dr. Corinne Henak, and Dr. Alejandro Roldán Alzate—for their valuable insights and constructive feedback during my oral dissertation defense, which significantly improved the quality of my work.

My heartfelt thanks go to my past and current labmates—Dr. Lejie Liu, Dr. Karthik Yerrapragada, Uraching Chowdhury, Haocheng Yang, Peilai Li, Kyobeom Ku, Xin Wei, Liam Sullivan-Konyn, Jon Brooks, Reid Milton, and Ryan Vandewiele—as well as to my collaborators, Dr. Timothy Truster, Agnila Ghosh Surovi, and James Rice. Your support has been invaluable in helping me complete my degree. I am especially thankful to Kyobeom Ku for the many fruitful discussions that enriched my research.

I am deeply grateful to my loving wife, Jinsol Lee. Her unwavering support has given me strength and motivation during the most challenging moments of my Ph.D. journey. I extend my heartfelt

appreciation to my parents, parents-in-law, sister, brothers-in-law, and sister-in-law for their endless encouragement. Special thanks to my friends in Madison—Jinsol Seo, Jungjin Ku, Dr. Chulwoong Kim, and Hu Jeffrey Hangchuan—as well as to my master's advisor, Dr. Yong Tae Kang, and my mentor, Dr. Sungsoo Kim.

Finally, I gratefully acknowledge the financial support for my Ph.D. dissertation provided by the National Science Foundation (CMMI-2224380 and CMMI-CAREER-1554146).

— Wonhyeok Lee

CONTENTS

LIST OF FIGURES

ABSTRACT

Gels are composed of polymer networks that are either chemically or physically crosslinked, or entangled, and swollen with a solvent. This unique structural composition imparts both bulk poro-viscoelastic properties and distinctive interfacial dynamics. At the interface, polymers can form bridge-like bonds—akin to hook-and-loop fastener—while the solvent can act as a lubricant. These combined bulk and interfacial characteristics give rise to complex yet unique tribological behaviors when gels interact with solid surfaces. Due to these compositions and unique properties, gels are widely utilized in applications such as soft robotics, drug delivery systems, and soft adhesives. Moreover, understanding the interfacial behavior of gels is critical not only for these technologies but also for fields like tissue mechanics and the food industry, where gels share compositional and structural similarities with biological tissues and food materials. In all these contexts, a deep understanding of surface interactions and interfacial properties is essential for accurate modeling and improved performance.

In this dissertation, gelatin is employed as a model physical gel to investigate its adhesive and frictional behavior when in contact with a glass surface. Compared to chemically crosslinked gels such as polyacrylamide hydrogels, gelatin exhibits pronounced bulk viscoelasticity in addition to poroelasticity. These bulk poroviscoelastic properties, combined with com-

plex interfacial dynamics, result in highly rate-dependent behavior during both peeling (adhesion tests) and shearing (friction tests). The primary objective of this work is to experimentally investigate the rate-dependent adhesion and friction of gelatin and to understand the underlying physical mechanisms. A key limitation in many previous studies is the lack of direct observation of the contact area, despite its critical role in tribological phenomena. To address this, custom-built adhesion and friction testers were developed, each integrated with an *in-situ* contact imaging module. This imaging capability enables real-time tracking of contact area and shape evolution during both adhesion and friction tests. The *in-situ* imaging approach allows for detailed exploration of peeling behavior—capturing its magnitude, directionality, and rate—as well as micro-slippage during pre-sliding, including its spatial heterogeneity, magnitude, and rate. This novel integration of imaging with mechanical testing provides a more comprehensive understanding of the interfacial mechanics in gelatin.

In adhesion experiments, the unloading rate was found to be the dominant factor influencing the apparent work of adhesion, while poroelastic diffusion during dwelling contributed secondarily through a suction effect. The Persson and Brener viscoelastic crack propagation model captured the rate-dependent behavior in gelatin well. Further investigation into transient peeling revealed that while crack velocity increased monotonically, the energy release rate exhibited non-monotonic behavior due to crack acceleration, viscoelastic dissipation, and size effects. A viscoelastic

crack propagation model qualitatively reproduced these trends but highlighted the need for incorporating interfacial rate-dependency. In friction studies, the pre-sliding regime was explored in detail. The results showed that static friction and contact area reduction are strongly rate-dependent. Two distinct regimes—full stick and partial slip—were identified, with energy dissipation occurring primarily through partial slip in the latter. The Cattaneo-Mindlin theory qualitatively described the observed partial slip behavior, despite its assumptions of elasticity, small deformation, and constant contact area. Overall, this work provides a comprehensive experimental framework for understanding the coupled bulk and interfacial mechanisms governing adhesion and friction in soft materials. Finally, possible future directions to further advance the field were discussed. These include efforts to disentangle bulk and interfacial contributions to rate-dependent adhesion in gels, and to investigate rate-dependent adhesion and friction in multi-asperity contact conditions, which are more representative of real-world soft interfaces.

1.1 Backgrounds

Hydrogels

A gel is a soft, hydrated material composed of a polymer network swollen with a solvent. It combines solid-like properties originating from a polymer network and fluid-like properties stemming from a solvent. The polymer network gives it its elasticity, and the solvent allows for fluid flow and diffusion. This complex and bi-phasic composition of gels presents unique characteristics in contact mechanics. Hydrogels are gels with water used as the solvent. In this dissertation, the focus is specifically on hydrogels, although the term gels and hydrogels are used interchangeably.

Chemical and physical gels

Depending on the type of crosslinking that holds the gel network together, two types of gels exist: physical gels (reversible gels) and chemical gels (covalent gels).

In chemical gels, the monomers build blocks of polymers and contain reactive functional groups that can undergo polymerization reactions. The chemical crosslinking agents are added to the mixture of solvent and polymer. The crosslinkers react with the polymer chains and form cova-

lent bonds between them. As a result of the crosslinking reactions, a 3D connected network is formed. These reactions may occur during polymerization (*in-situ* crosslinking) or as a post-polymerization treatment (post-crosslinking). The resulting networks are strong and permanent, which leads to the nature of irreversibility, stability, and elasticity of gels (Winter, 2001). A common example of a chemical gel is polyacrylamide (PAAm) hydrogel, which is widely used in the production of contact lenses and mechanics studies.

Physical gels do not contain chemical crosslinks within their polymer networks. However, this does not imply the absence of covalent bonds altogether. The atoms within each individual polymer chain are held together by strong covalent bonds. These polymer chains are formed through polymerization, a process in which small monomer units are chemically bonded to create long molecular chains. The typical size of monomers (e.g., amino acid for gelatin) is 0.3-0.5 nm, and a single chain with a size of 15–300 nm consists of 50-1000 monomers (Hudson, 1994). However, the real size of a single chain could be much smaller than this due to the entanglement, coiling, and folding. In physical gels, these chains formed by the numerous monomers themselves are held together by weaker physical bonding such as van der Waals interactions. In some polymers containing specific functional groups such as hydroxyl(-OH) or amide(-NH), hydrogen bonding can occur. This hydrogen bonding is stronger than van der Waals interactions but weaker than covalent

bonding (Baumberger et al., 2006a). Another mechanism helping network formation and stability is physical entanglement. The polymer chains when entangled with each other, create physical crosslinks and restrict chain movement. Gelatin and alginates are typical examples of physical gels.

Gelatin

Gelatin is a type of physical gel derived from the partial hydrolysis of collagen heated to 40–100°C (Poppe, 1992). Collagen itself is composed of three polypeptide chains wound together in a triple-helix structure, which provides mechanical strength and structural integrity to connective tissues such as skin, bones, tendons, and cartilage (Poppe, 1992). During hydrolysis, the fibrous and insoluble collagen protein is broken down into smaller peptide chains or individual amino acids (Wu et al., 2023). Upon cooling again, these chains in gelatin can partially reassemble into triple-helix-like junction zones, mimicking the native collagen structure. Unlike chemical gels that rely on permanent covalent crosslinking, gelatin forms a reversible network through physical interactions, primarily hydrogen bonding and chain entanglement. This network is biocompatible and thermoreversible; i.e., gelatin solutions form gels upon cooling and revert to sol upon heating; properties that underpin its widespread use in food, pharmaceutical, and biomedical applications. Gelatin is typically derived from mammalian sources and is classified into two main types based on its

extraction method: Type A and Type B. Type A gelatin is obtained through acid hydrolysis of collagen, commonly sourced from porcine skin, while Type B gelatin is produced via alkaline hydrolysis, usually from bovine hides or bones. In this dissertation, Type A gelatin powder derived from porcine skin, with a Bloom value of 300, is utilized. The Bloom value (BV) is a standard measure of gel strength, with commercial gelatin typically ranging from 50 to 300 Bloom units (Ahmed, 2017). Detailed procedures for determining the Bloom value are outlined in Ref. (International, 2016).

Gel elasticity

Elasticity in gels originates from different physicochemical principles compared to elasticity in typical engineering materials. For instance, in metal and ceramic, the elasticity arises from the changes in the internal energy of the material. When the material is deformed, the atoms are displaced from their equilibrium positions. This leads to changes in the potential energy stored in the bonds. These changes induce restoring forces referred to as energetic elasticity. For soft materials as rubber and gels, the changes in the internal energy are relatively small. In contrast, the change in free energy by the change of entropy is significant. When the material is stretched, the chains are pulled into more ordered states, reducing their conformational entropy. The restoring force that restores the material back to its original shape upon unloading is due to the tendency of the system to maximize entropy (2nd law of thermodynamics). In other words, the

decrease in entropy due to deformation creates a thermodynamic driving force that acts to restore the material to its original, higher entropy state. Entropic elasticity plays a crucial role in understanding the elastic behavior of rubber and gels. For instance, materials with a higher density of crosslinkers have shorter polymer chains between crosslinking points. These shorter chains have fewer possible configurations, which limits the amount of elastic (entropic) energy they can store. As a result, increasing the number of crosslinks makes the material stiffer but also less tough (Lake and Thomas, 1967).

Poroelasticity

The entangled and/or crosslinked polymer chains form a porous network, which can be characterized by the mesh size. According to de Gennes, the mesh size of gels ζ is determined by the balance between the elastic restoring forces of the polymer network and the thermal energy of the system (De Gennes, 1979). Specifically, the mesh size scales with the shear modulus and temperature, and is also influenced by the solvent viscosity through its effect on polymer dynamics, given by:

$$\zeta \sim \left(\frac{k_b T}{G}\right)^{1/3}, \tag{1.1}$$

where k_b, T, and G are the Boltzmann constant, absolute temperature, and the shear modulus. In general, a stiffer network (higher modulus)

corresponds to a smaller mesh size, while higher temperatures tend to increase thermal fluctuations and expand the mesh. In hydrogels, water exists in two primary forms (Yoshida et al., 1993). The first type is bound water, which is either adsorbed onto or trapped within the polymer chains. This water is closely associated with the polymer network and does not move freely. The second type is free water, which resides in the pores of the gel and can migrate relatively easily from one region to another. The balance between bound and free water significantly influences the gels' mechanical properties, swelling behavior, and transport characteristics.

Gel poroelasticity describes the coupled mechanical and fluid transport behavior in gels. When a porous gel network is deformed, volumetric strains drive the diffusion of the free solvent through the interconnected pores. This interaction between the elastic deformation of the solid phase and the viscous flow of the fluid gives rise to time-dependent mechanical responses. The rate of solvent migration depends on pore (mesh) size, network stiffness, and solvent viscosity. At short timescales, the gel behaves more elastically as the fluid has little time to redistribute, while at longer timescales, fluid flow leads to stress relaxation and a more viscous or dissipative response. The poroelastic solvent diffusion can be characterized by the diffusivity or permeability of gels. Diffusivity in a gel refers to how fast molecules (like water) spread through the gel matrix. According to de Gennes (De Gennes, 1979), the diffusivity D of a solute in a polymer

network can be estimated as:

$$D \sim \frac{k_b T}{\eta_s \zeta}, \tag{1.2}$$

where η_s is the solvent viscosity. Furthermore, the permeability μ_p is related to the diffusivity through the following expression (Hu et al., 2010):

$$D = \frac{2(1-\nu)}{1-2\nu} \frac{G\mu_p}{\eta_s}, \tag{1.3}$$

where ν is the Poisson's ratio of the gel. These relations highlight the coupling between mechanical and transport properties in poroelastic materials. When a gel is in contact with an opposing surface and has a contact radius a, the effective poroelastic relaxation time constant τ_{PE} can be approximately estimated as:

$$\tau_{\mathrm{PE}} \sim \frac{a^2}{D}. \tag{1.4}$$

This relation reflects the time scale over which fluid redistributes within the gel in response to mechanical loading. For gels with water solvent, the typical value of D ranges from 10^{-9} to 10^{-11} m^2/s (Ohmori, 1989; Rockwell et al., 2023; Penke et al., 1998). For contact areas ranging from 1 mm to 10 mm in this dissertation, the poroelastic relaxation time constant is estimated to be between 10^4 and 10^6 seconds (assuming $D = 10^{-10}$ m^2/s), which is significantly slower than the viscoelastic relaxation time of gelatin, typically less than 0.1 seconds(Yengul et al., 2019; Normand and Ravey,

1997).

Viscoelasticity

The viscoelasticity of gels is often attributed to the entanglement and reptation of polymer chains. These entanglements act as physical crosslinks, restricting chain mobility and impeding the flow of polymers past one another. This internal resistance to motion is commonly described as friction between polymer chains, which contributes to the material's viscous behavior. Reptation is a mechanism that describes the motion of polymer chains as they move in a snake-like fashion through a network of entanglements (De Gennes, 1971). When subjected to an applied stress, polymer chains tend to align and stretch out along the direction of the stress, and exhibit elastic behavior temporarily. Over time, as the entangled chains rearrange themselves, polymer chains move by reptating along their length within the constraints of the entangled networks, and the stress is relaxed, and the material exhibits viscous flow.

Typically, chemical gels are considered to exhibit minimal viscoelastic behavior due to their strong crosslinking restricting the reconfiguration of polymer chains under mechanical loading or deformation. In contrast, physical gels such as gelatin are known to exhibit pronounced viscoelasticity. In gelatin, the collagen molecules form a triple-helix structure, and the resulting networks are entangled rather than chemically crosslinked. This complex yet flexible network, stabilized by weaker physical interactions,

allows for structural rearrangement under loading, thereby giving rise to viscoelastic behavior (He et al., 2020). However, some studies(Baumberger et al., 2006a; Baumberger and Ronsin, 2009) argue that the bulk viscoelasticity of gelatin may be negligible, primarily due to their low polymer content relative to water. For instance, experimental observations often show that the loss modulus is significantly smaller than the storage modulus, suggesting limited energy dissipation through viscoelasticity (Ahmed, 2017; Normand and Ravey, 1997; Yengul et al., 2019). Instead, it has been proposed that viscous drag between the solvent and the polymer network at smaller scales plays a more dominant role in the mechanical response of these systems such as in the rate-dependent fracture problems.

Contact mechanics

Hertzian contact

Hertz (Hertz, 1881) solved the contact problem of elastic deformation of two spheres with radii R_1 and R_2 pressed against each other with a load of P. Hertz solution is only applicable to homogenous isotropic, linear elastic material response, smooth surfaces, and small deformations without adhesion and friction. The contact radius a and the deflection δ in Hertzian solution have a kinematic relation $a = \sqrt{R\delta}$, the effective/composite radius R is $1/R = 1/R_1 + 1/R_2$, where R_1 and R_2 are the radii of two spheres, and the pressure distribution is given by $p(r) = p_0\sqrt{1 - r^2/a^2}$, where

p_0 is the maximum contact pressure at $r = 0$. By integrating the contact pressure over the contact area, p_0 is given by $p_0 = 1.5\overline{p} = 3P/2\pi a^2$, where $\overline{p}$ is the mean contact pressure. The contact area is determined by the material stiffness, the effective radius, and the normal load as $a = (3PR/4E^*)^{1/3}$. Here, E^* is the contact modulus (or effective modulus) given by $1/E^* = (1-\nu_1^2)/E_1 + (1-\nu_2^2)/E_2$, where ν_1, ν_2, E_1, and E_2 are the Poisson's ratios and elastic moduli of contacting spheres. In this dissertation, contact occurs either between a spherical glass indenter and a flat gelatin substrate (adhesion test), or between a flat glass surface and a spherical gelatin sample (friction test). The Young's modulus of glass is approximately 65 GPa, which is significantly higher than that of gelatin. Thus, the glass is treated as a rigid body in both configurations.

Adhesion

Adhesion describes the attractive (tensile) forces that act between different materials, typically at the interface. For example, when peeling tape from a box, if the tape detaches cleanly without any residue, the failure occurs at the interface between the tape and the box—this is known as adhesive failure. Adhesion can arise from various mechanisms, some of which contributes to what is known as apparent adhesion. The primary mechanisms of adhesion include: chemical bonding, physical interaction (e.g., van der Waals force), electrostatic interaction, mechanical interlocking and interlocking of polymer chains, and suction (Sauer, 2016). Among these,

chemical bonding and van der Waals interactions operate over very short distances —typically within a few nanometers or even less than 1 nanometer— qualifying them as short-range adhesion. In contrast, mechanisms such as electrostatic forces can act over much larger distances, extending up to several centimeters, and are therefore considered long-range adhesion. In the context of gel adhesion discussed throughout this dissertation, the focus will be on short-range adhesion. The work of adhesion $\Delta\gamma$ is commonly used to quantify the strength of adhesive interactions between two surfaces or molecules. It is calculated based on the surface energies of the two materials, γ_1 and γ_2, and their interfacial energy γ_{12}, using the relation:

$$\Delta\gamma = \gamma_1 + \gamma_2 - \gamma_{12}. \tag{1.5}$$

In the special case where the two surfaces are made of identical materials, the interfacial energy is typically assumed to be zero, i.e., $\gamma_{12} = 0$, leading to:

$$\Delta\gamma = 2\gamma_1. \tag{1.6}$$

Significant efforts to incorporate adhesion into Hertzian contact mechanics emerged in the 1970s (Johnson et al., 1971; Derjaguin et al., 1975). Notably, in 1971, Johnson et al. (Johnson et al., 1971) introduced a seminal contribution to the field with the JKR model, which extended contact mechanics to include adhesion between elastic spheres. Building on the Hertzian contact theory for elastic spheres, Johnson et al. su-

perimposed the effects of adhesive interactions —modeled similarly to those in a cylindrical punch problem— onto the Hertzian solution. In the case of a cylindrical punch, the contact pressure distribution is given by: $p(r) = P/\pi\sqrt{a^2 - r^2}$, where P is the applied load, and r is the radial coordinate within the contact area. This pressure profile exhibits a singularity at the contact edge ($r \to a$) and reaches its minimum at the center of the contact area ($r \to 0$). The authors assume that the contact radius with adhesion, denoted as a_1, is larger than the non-adhesive contact radius a_0, due to the presence of attractive surface forces. Based on this assumption, the contact is modeled such that in the region $r \leq a_0$, the contact is governed by Hertzian theory, where a compressive traction is applied. In the annular region $a_0 < r \leq a_1$, a tensile traction is applied, modeled using the elastic contact solution of a flat-ended cylindrical punch. The total contact pressure distribution is obtained by superposing the pressure fields from these two models. First, the kinematics based on the superposition approach is given by:

$$\delta = \frac{a^2}{R} - \sqrt{\frac{2\pi\Delta\gamma a}{E^*}}, \tag{1.7}$$

where the first term arises from the kinematic relation of the Hertzian model, and the second term represents the additional displacement due to surface adhesive interactions, modeled using the cylindrical punch solution. To determine the equilibrium state, the total energy U_T of the system is evaluated as the sum of the elastic strain energy U_E, the mechanical

potential energy U_M, and the surface energy U_S. Minimizing the total energy with respect to the contact radius yields the equilibrium solution for adhesive contact between elastic spheres. Applying the equilibrium condition $\mathrm{d}U_T/\mathrm{d}a_1 = 0$ yields the final form of the JKR equation:

$$a^3 = \frac{3R}{4E^*}\left[P + 3\pi\Delta\gamma R + \sqrt{6\pi\Delta\gamma RP + (3\pi\Delta\gamma R)^2}\right]. \tag{1.8}$$

The JKR solution can also be derived using linear elastic fracture mechanics (LEFM), by considering the stress intensity factor associated with the singular contact pressure at the edge of the contact area. This alternative derivation is detailed elsewhere (Maugis and Barquins, 1978; Greenwood and Johnson, 1981). From Eq. 1.8, the pull-off force is predicted as: $F_{\mathrm{pull-off}} = 1.5\Delta\gamma\pi R$. The JKR model serves as an asymptotic solution in the limit where the Tabor parameter $\mu_t \equiv \left(\Delta\gamma^2 R/E^{*2}Z_0^3\right)^{1/3} \gg 1$, with Z_0 being the equilibrium separation distance at which the potential energy is minimized (Tabor, 1977). A large Tabor parameter ($\mu_t \gg 1$) corresponds to systems with compliant materials, large probe radius R, and/or high work of adhesion $\Delta\gamma$. At the other asymptote where $\mu_t \ll 1$, the Derjaguin, Muller, Toporov (DMT) theory (Derjaguin et al., 1975) is more appropriate. In the intermediate regime between these two limits, the Maugis–Dugdale (M-D) model (Maugis, 1992) provides a smooth transition by incorporating a cohesive zone model approach, analogous to the Dugdale model used in fracture mechanics (Dugdale, 1960). Further

details on the DMT theory and the M-D model can be found in Refs. (Derjaguin et al., 1975; Maugis, 1992).

In this dissertation, gelatin is used the common material used. It has a relatively low modulus E, typically ranging from a few kilopascals to a few hundred kilopascals depending on temperature, concentration, and solvent constituents (Ahmed, 2017). Additionally, the probe radius used in the experiments is sufficiently large, approximately $R \approx 10$ mm. These conditions justify the application of the JKR theory for most of the problems studied in this work.

Although these models enhance our understanding of adhesion mechanics, they are fundamentally based on elastic material behavior and therefore do not account for rate effects. Numerous studies have demonstrated that many polymers and multiphasic soft materials such as gels and biological tissues exhibit rate-dependent adhesion (Han et al., 2020c; Smith and Callow, 2006; Zhang et al., 2017). This behavior can arise from various mechanisms such as plasticity, viscoelasticity, and poroelasticity, and interfacial bond dynamics. To model rate-dependence in adhesion, crack propagation in viscoelastic medium has been studied extensively since the 1980s (Johnson, 1987; de Gennes, 1996; Persson and Brener, 2005).

Friction

Friction arises when there is relative tangential motion at an interface, requiring energy to overcome interactions or to deform materials, and is

typically accompanied by energy dissipation. At the atomic scale, adhesive forces such as van der Waals interactions, chemical bonding, and hydrogen bonding between molecules can contribute to frictional resistance. At the microscale, friction can result from mechanical interlocking between surface asperities and from plowing of a harder surface into a softer one, which may induce significant plasticity. These deformation mechanisms serve as additional sources of friction. In soft materials such as gels and rubbers, friction can also arise from the adsorption and detachment of polymer chains during relative motion (Gong, 2006; Brochard-Wyart and de Gennes, 2007). This dynamic interaction between polymer chains and the contacting surface generates resistance to sliding and contributes to the overall frictional behavior. Classical Coulomb friction model describes the phenomenological behavior of friction using the relation: $F_t = \mu P$, where F_t is the friction force, P is the normal load, and μ is the coefficient of friction. In this model, μ represents the resistance to relative motion and is assumed to be independent of sliding velocity, normal force, and other state variables. As the friction force builds up, the shear stress across the contact area increases. When the shear stress reaches the shear strength of the interface, sliding initiates. This model provides a simple yet effective framework for understanding frictional behavior in many engineering and physical systems.

The Cattaneo-Mindlin model (Mindlin, 1949; Cattaneo, 1996) extends the classical Coulomb friction law to the Hertzian contact problem under

tangential loading. The model begins with a Hertzian contact formed under a constant normal load P, and then a tangential force F_t is applied quasi-statically while maintaining P constant. The theory treats the interface as a constraint on relative tangential displacements. As F_t increases, the shear traction $q(r)$ at the edge of the contact area reaches the local frictional limit $\mu p(r)$, where $p(r)$ is the normal contact pressure distribution. Since $p(r)$ decreases toward the edge of the contact area ($r \to a$), sliding initiates at the periphery. As the tangential load continues to increase, the slip region propagates inward toward the center of the contact area. When the entire contact area is involved in slip, the system reaches the fully sliding regime. This model captures the transition from partial slip to full sliding and provides a description of frictional contact in elastic bodies. The Cattaneo-Mindlin model excludes the effects of adhesion on friction and assumes that the contact radius a remains constant during tangential loading. This simplification allows the model to focus solely on the redistribution of shear traction and the evolution of the slip region under increasing tangential force.

In 1977, Savkoor and Briggs (Savkoor and Briggs, 1977) extended the JKR model to incorporate the effects of adhesion in frictional contact. Their work investigated how a tangential force influences the adhesive contact area between two elastic solids. Both the theoretical model and experiments on rubber-on-glass contacts clearly demonstrated a reduction in contact area as the tangential force F_t increases. While the contact

radius decreases, the shape of the contact area remains circular rather than becoming elliptical. In contrast, several studies have reported a reduction in contact area under tangential loading that results in an elliptical rather than circular shape (Misra and Huang, 2011; Papangelo et al., 2019; Sahli et al., 2019). This reduction in contact area is interpreted as a peeling process, analogous to crack propagation at the interface. According to Savkoor (Savkoor, 1992), this peeling phase is stable and reversible, and occurs without any slip or partial slip. It is followed by a transition phase, during which the contact area remains constant and the interface continues to resist slip. Finally, the system enters the slipping phase, where slip initiates at the edge of the contact and progressively propagates toward the center. This final phase is characterized by irreversible deformation and energy dissipation.

Abovementioned models, espcially Cattaneo-Mindlin model, assume local shear strength of the interface preventing slip is proportional to local normal tractions, and proportionality constant; i.e., coefficient of friction, is constant. In practice, the friction coefficients μ are documented to depend on sliding speed, evolves over time at rest or during sustained motion, and is dependent on loading history. To address this, rate-and-state friction (RSF) model is developed (Dieterich, 1979; Ruina, 1983):

$$\mu = \mu_0 + a \ln \frac{V}{V_0} + b \ln \frac{\theta}{\theta_0}, \tag{1.9}$$

where V is the slip rate, and θ is a state variable. a, b are empirical constants controlling rate and state sensitivity. The state variable includes the contact aging effect and history of sliding. In gels, the bond dynamics at the interface can be incorporated into the rate-and-state friction (RSF) framework. For example, polymer chains in gels can form bonds with an opposing surface (e.g., glass) through hydrogen bonding or van der Waals interactions. These polymer chains exhibit viscoelastic or plastic behavior. The formation of interfacial bonds requires a finite amount of time, often referred to as the healing time, which typically ranges from 10^{-6} to 10^{-5} seconds (Brochard-Wyart and de Gennes, 2007). During sliding, these bonds can be stretched, detached, and re-formed, leading to pronounced rate-dependent and history-dependent frictional behavior.

1.2 Motivation

Poroviscoelastic (PVE) materials exhibit a combination of viscoelastic relaxation of polymer chains and poroelastic diffusion of solvent, resulting in complex time- and rate-dependent mechanical behavior. Gelatin, a physically crosslinked hydrogel, serves as a model soft multiphasic material to investigate how these two relaxation mechanisms influence adhesion and friction under varying mechanical conditions. Understanding the adhesion and frictional behavior of soft materials such as gelatin is essential for a wide range of applications, including the food industry,

tissue engineering, soft robotics, and soft adhesives. In these contexts, the mechanical response is influenced not only by the bulk properties of the material but also by interfacial dynamics that evolve over time and vary with the rate of loading and unloading. For example, cartilage in human joints—structurally and mechanically similar to gelatin—experiences sliding velocities ranging from approximately 10^{-3} to 10^{-2} mm/s during activities like standing up, and from 1 to 10 mm/s during running. To better understand and optimize performance in these applications, it is crucial to investigate the rate-dependent adhesion and frictional behavior of soft materials across this velocity range.

Previous studies have shown that loading/unloading rate significantly affect adhesion and friction in soft materials. However, the interplay between viscoelastic and poroelastic effects remains poorly understood especially in adhesive behavior in gelatin. In addition to this, most prior research on soft material adhesion has focused on steady-state or quasi-static detachment, often neglecting the transient dynamics that occur during peeling. In particular, the effects of crack acceleration and boundary conditions on the instantaneous energy release rate have not been thoroughly established. In the study of friction, the pre-sliding regime—where partial slip and interfacial deformation occur before full sliding—is often overlooked. Most existing studies emphasize the fully sliding regime, despite the fact that pre-sliding plays a critical role in determining the onset of motion and energy dissipation. Moreover, conventional friction models

rarely account for rate-dependent interfacial behavior or the evolution of contact area during pre-sliding for gelatin. This dissertation is a systematic investigation to address these gaps in the literature. Another key limitation in prior works is the lack of direct observation of the contact interface, which is essential for understanding the underlying mechanics of adhesion and friction. To address this, a major contribution in this dissertation is the integration of a high-resolution *in-situ* contact imaging module into custom-built adhesion and friction testers. This imaging capability enables real-time visualization of contact area evolution, crack propagation, and interfacial slip—providing critical insights that are not accessible through force measurements alone. This dissertation features both experimental tools and analytical modeling to explore the effects of bulk poro-viscoelasticity and bond dynamics at the interface. The key findings such as the rate-dependent crack propagation, non-monotonic energy release behavior, and velocity-strengthening friction highlight the need for integrated models that account for both bulk and interfacial dynamics.

1.3 Outline of the Dissertation and Main Findings

Chapter 2

Chapter 2 presents a detailed investigation into the poroviscoelastic (PVE) behavior of gelatin and its influence on rate-dependent adhesion. A series of probe-tack experiments were conducted using a custom-built setup that allowed precise control over loading, dwelling, and unloading conditions. The main contributions of the part of the study reported in this chapter are:

- The crack (contact edge) velocity is strongly dependent on the unloading rate and increases monotonically during peeling.
- The unloading rate has a dominant influence on gelatin adhesion, while the effect of dwelling time is secondary.
- Crack propagation models developed for viscoelastic solids can be effectively applied to poroviscoelastic materials like gelatin.
- The dwelling time effect on adhesion arises from poroelastic diffusion during loading and dwelling—commonly referred to as the suction effect—which also exhibits rate-dependent behavior.

This work has resulted in two publications and one paper currently in preparation.

- Lee, W. and Eriten, M., 2024. Poroviscoelastic relaxations and rate-dependent adhesion in gelatin. *Soft Matter*, 20(23), pp.4583-4590
- Yerrapragada, K., Yang, H., Lee, W., & Eriten, M. (2024). Characterization of drying-induced changes in moduli and internal stresses in a constrained gel using laser vibrometry. *Soft Matter*, 20(4), 813-822.
- Rice, J., Volety, S., Lee, W. , Eriten, M., Pirasteh, A. , Hernando, D. & Roldán-Alzate, A., Characterization of a Tissue-Mimicking Liver Flow Phantom for Use in Magnetic Resonance Elastography and Diffusion Weighted Imaging MRI Validation Experiments (in prep)

Chapter 3

Chapter 3 investigates the transient behavior of rate-dependent adhesion in gelatin, focusing on the complex interplay between crack propagation dynamics and viscoelastic dissipation during adhesive contact. Building on previous experimental work discussed in Chapter 2, the study revisits probe-tack tests involving the monotonic unloading of a spherical glass probe from a gelatin surface. The main contributions of the part of the study reported in this chapter are followings:

- The instantaneous energy release rate exhibits non-monotonic behavior during the peeling process in gelatin, while the crack velocity increases monotonically.
- The viscoelastic crack propagation model shows good qualitative agreement with experimental observations in the instantaneous energy release rate during peeling process.
- The non-monotonic behavior is attributed to crack acceleration, bulk viscoelasticity, and size effects.
- The model has limitations in fully explaining the behavior, indicating the need to incorporate a rate-dependent interfacial model in addition to bulk viscoelasticity.

This work has resulted in one submitted paper and another currently in preparation.

- Lee, W. and Eriten, M., 2025. A Note on Transients in Rate-dependent Adhesion of Gelatin, *Tribology Letters*, (submitted)
- Ku, K., Lee, W., and Eriten, M., Transient Dissipation in Viscoelastic Contact, (in prep)

Chapter 4

Chapter 4 presents a detailed investigation into the rate-dependent frictional behavior of gelatin in the presliding regime. A custom-built friction

tester was developed, instrumented with an in-situ contact imaging module to capture the evolution of contact area and local slip during shear loading. The main contributions of the study are:

- The static friction force exhibits velocity-strengthening behavior over the driving velocity range $U = [0.01\text{–}10]$ mm/s.
- The contact area shrinks during the pre-sliding regime, showing strong rate-dependence: higher driving velocities lead to greater area reduction.
- The Cattaneo-Mindlin theory captures the partial slip behavior observed during pre-sliding.
- The energetic analysis reveals that slippage contributes more significantly to pre-sliding friction than peeling.

This work has resulted in one paper currently in preparation.

- Lee, W. and Eriten, M., Rate-Dependent Friction during Pre-sliding in Gelatin, (in prep)

Chapter 5

Chapter 5 summarizes the key findings of the work presented in Chapters 2 through 4. The chapter also discusses the challenges and unresolved issues related to rate-dependent adhesion and friction in gelatin. The main

findings and identified limitations provide important directions for future research. My previous work has contributed to this direction by investigating how surface patterns generated by spinodal decomposition and amplified Rayleigh–Taylor instability affect contact mechanics using boundary element method (Lee, W. and Eriten, M., 2023. Real area of contact and tractions on the patterned surfaces generated by spinodal decomposition and amplified instability. *Frontiers in Mechanical Engineering* 9, p.1253207). Additionally, a collaborative study explored experimental advancements in characterizing surface topography for rough surfaces (Pradhan et al., 2025. The surface-topography challenge: A multi-laboratory benchmark study to advance the characterization of topography. *Tribology Letters*, (accepted)). These efforts have laid the groundwork for extending the research group's capabilities toward the study of multi-asperity contact, enabling future investigations into more realistic and application-driven contact scenarios.

2 CHAPTER2. POROVISCOELASTIC RELAXATIONS AND RATE-DEPENDENT ADHESION IN GELATIN*

(*Reprinted from Soft Matter. This material is reproduced in accordance with the publisher's policy. © The Royal Society of Chemistry)

2.1 Introduction

Hydrogels are poroviscoelastic (PVE) materials that consist of a polymer network swollen with water (Baumberger et al., 2006b). The polymer network can be formed by physical or chemical crosslinks(Zhang et al., 2008). When deformed, the polymer network exhibits a time-dependent stress-strain response and PVE relaxations (Ferry, 1980; Lakes, 2009); the polymer chains reconfigure and reach a new equilibrium: viscoelastic relaxation, and the solvent diffuses through the polymer networks due to pressure gradient: poroelastic relaxation (Cheng, 2016; Schulze et al., 2017). In a PVE material, those relaxations can occur concurrently (Chan et al., 2012) and influence adhesion and fracture. For instance, several studies have explored the influence of contact time on adhesion in hydrogels (Lai et al., 2019; Reale and Dunn, 2017; Michel et al., 2019; Serrano, 2019), in cartilage (Han and Eriten, 2018a), in mucin gel (McGhee et al., 2019) and adhesives on hydrated biological tissues (Li et al., 2017a). Those studies report that adhesion increases with contact (holding/dwelling)

time thanks to suction effect caused by an unbalanced osmotic pressure over the contact (Reale and Dunn, 2017; Han et al., 2019; McGhee et al., 2019). Moreover, Michel et al. (Michel et al., 2019) demonstrated that with contact time, freely available water over the contact between a dry hydrogel film and liver tissue transports into the hydrogel. This leads to enhanced solid-solid contact and adhesion. A similar adhesion mechanism was proposed by Lai et al. (Lai and Hu, 2021) where the amount of polymer chains adhering to the counter surface and thus pull-off forces increase with contact time. Moreover, adhesion measured on PVE materials depends on unloading rates as observed in cartilage (Han et al., 2019), insect feet (Labonte and Federle, 2015), oil-swollen foams (Liu et al., 2022), and epithelial cells (Esfahani et al., 2021). For explaining the rate-dependence, fracture and adhesion mechanics of viscoelastic solids has been promising. Whether due to deformation kinematics local to contact edges (Schapery, 1975; Hui et al., 1992; Greenwood and Johnson, 1981; Greenwood, 2004) or viscoleastic dissipation (de Gennes, 1996; Persson and Brener, 2005; Persson, 2021) during peeling, higher unloading rates are shown by those models to increase the apparent work of adhesion in viscoelastic materials. The mechanisms governing the contact time and rate-dependent adhesion in PVE materials are more complicated as diffusion and relaxation mechanisms can be coupled. In this work, we will examine adhesion of gelatin on a glass probe at broad time scales relevant to PVE relaxations. This way, we hope to decouple the influences

of poroelastic diffusion and viscoelastic relaxations, and obtain dominant mechanisms leading to rate-dependent adhesion in multiphasic materials.

In particular, we conduct adhesion tests on gelatin at various unloading rates and hold times that trigger only non-inertial response of the gels; i.e., crack (contact edge) velocities remain much lower than shear wave velocity. We also characterize PVE time constants, and correlate the enhancement of gel adhesion to the degree of relaxation. Besides, we capture contact images to analyze contact kinematics, and its link to local viscoelastic response and thus enhancement of adhesion. Our results indicate that PVE response localized under the rigid probe leads to an order of magnitude increase in the apparent work of adhesion. Furthermore, that enhancement correlate well with contact kinematics such as crack velocities and tip (contact edge) opening during separation. Those observations corroborate well with the scaling laws predicted by existing crack propagation theories in viscoelastic materials. So-called suction effect due to increasing dwelling times has a second order effect on adhesion compared to the viscoelastic enhancement. Those results are essential in better understanding and control of adhesion in soft multiphasic materials.

2.2 Methods and Analyses

Sample preparation

Gelatin samples are prepared by blending 5 w/v% of gelatin powder from porcine skin (G2500 Type A, Sigma Aldrich, Inc.) with water. This concentration is chosen considering the transparency and stiffness required for the imaging module, contact size, and load cell specifications. The blend is heated to 60°C and mixed at 150 rpm for 30 minutes to achieve a homogeneous solution. The solution is then cooled to 45°C while being stirred in an ambient condition. To remove bubbles from the solution, it is placed in a vacuum chamber (1.5 gal, Vevor) connected to a vacuum pump (3.6 CFM, 1/4 HP, Vevor). The pressure is kept at 20 kPa until all visible bubbles in the solution have been removed. Then, the solution is poured into a petri dish (50 mm radius and 15 mm thickness) and cured in a refrigerator for 2 hours at 5°C. Before mechanical testing, the sample is allowed to equilibrate at room temperature ($T = 23$°C) for 10 minutes.

Adhesion tests

Adhesion tests are conducted in a custom-built probe tack tester, sketched in Fig. 2.1(a).

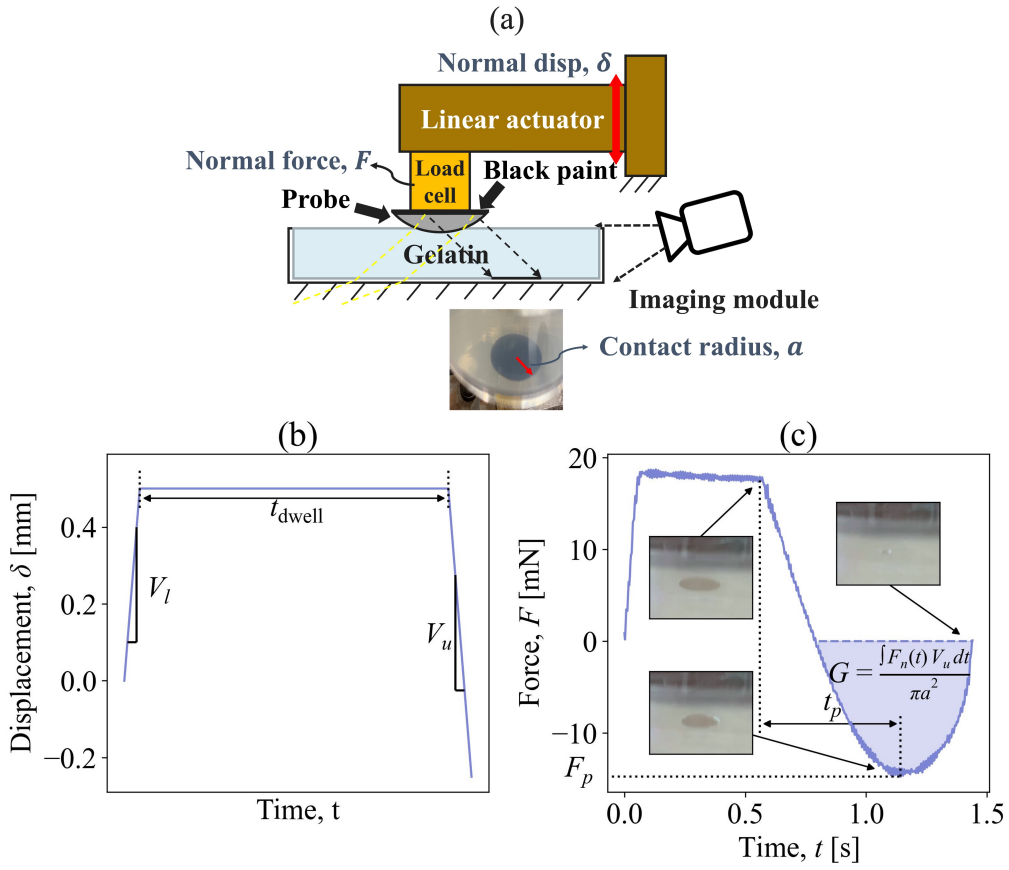

Figure 2.1: (a) The sketch of the experimental setup and a contact image captured by the imaging module, and (b) A representative normal displacement δ profile used in the adhesion experiments. The loading rate of $V_l = 10$ mm/s, the unloading rates of $V_u = \{0.01, 0.1, 1, 10\}$ mm/s, and the dwell times of $t_{\text{dwell}} = \{0.5, 100, 200\}$ s are used in the experiments. (c) A representative force measurement obtained from the adhesion experiment at a dwelling time of $t_{\text{dwell}} = 0.5$ s and unloading rates of 1 mm/s. Inset figures in (c) show the evolution of the contact area during unloading corresponding to the beginning of unloading, pull-off, and right before full-separation. The contact radius at the beginning of unloading is 2.9 mm.

A motorized linear actuator (VT-75, Physik Instrumente, 2 μm resolution) is used to apply the normal displacement δ in y direction. A stiff bar extending from the actuator carries a low-capacity miniature S-beam load cell (LSB200, 10 g capacity, FUTEK, Inc, 50 μN resolution) to measure the normal force F and a plano-convex glass lens (Edmund Optics, Inc.) with a tip radius of $R = 10.54$ mm to be used as the probe. The probe is impermeable and can be assumed rigid thanks to the six order of magnitude contrast in glass and gel moduli. The plane-side of the probe that is attached to the load cell has a radius of 6.35 mm.

Before each test, we center and fix the sample below the probe. Then, we lower the probe until the first moment of contact as detected by the contact imaging (see §2.2 for details). Once the surface is identified, the probe is retracted to a close but noncontact position relative to the sample surface. The surface detection step enables faster loading and consistent contact areas during dwelling portion of the actual adhesion tests. The actual adhesion tests consist of three steps: loading, dwelling and unloading, as depicted in Fig. 2.1(b). Initially, the probe is indented into the surface by 0.5 mm at 10 mm/s. The loading duration ~ 0.05 s is much smaller than the viscoelastic relaxation time constant $\tau_{\mathrm{VE}} = 0.222$ s, as estimated from the relaxation response (see Appendix A). An indentation of 0.5 mm results in a contact radius $a \approx 2.9$ mm, as measured by the contact imaging module. Given that the contact radius is significantly smaller than the dimensions of the gelatin sample (50 mm radius and 15 mm

thickness), the boundary effects are negligible. After loading, the probe is held stationary at 0.5 mm displacement for dwelling times $t_{\text{dwell}} = 0.5$, 100 and 200 s. During this time, the hydrogel's solid networks reconfigure quickly (viscoelastic relaxation) under deformation, while the water diffuses slowly away from the highly stressed contact zone (poroelastic relaxation). Since we conduct all testing in ambient conditions, dehydration of the gelatin samples is inevitable. To limit water losses to within 5 wt.%, we finish all testing within a few hours. That is why we set the longest dwelling time to 200 s. Note that we measure the poroelastic time constant as 87.3 s (see Appendix A) and so 90% of the poroelastic relaxation occurr within 200 s, and thus enable us to study the influence of broad degree of poroelastic relaxations on adhesion. At the end of the dwelling period, the probe is retracted until full separation, at different unloading rates $V_u =$ 0.01, 0.1, 1, and 10 mm/s. The lower bound of unloading rate $V_u = 0.01$ mm/s is determined considering the enhancement of work of adhesion. In preliminary experiments, the apparent work of adhesion at $V_u < 0.01$ mm/s shows a similar value to the one at $V_u = 0.01$ mm/s. The upper bound $V_u = 10$ mm/s is chosen to ensure the crack velocity is sufficiently below the shear wave speed of gelatin $V_s \sim 2$ m/s, thereby restricting our experiments to the range of subsonic cracks and non-inertial material response. Between each test, we allow the sample to equilibrate for $t_{\text{break}} > t_{\text{dwell}}$ and monitor its weight to ensure that the sample does not undergo more than 5 wt.% dehydration.

We repeat adhesion tests four times for each dwelling time and unloading rate (totally 48 tests), while monitoring the normal force F at a sampling frequency of 400 Hz. Fig. 2.1(c) presents examples of force measurements from the adhesion tests at 0.5 s dwelling time and 1 mm/s unloading rates. From those measurements, we extract the pull-off force F_p and the apparent work of adhesion G as the measure of adhesive strength. As shown in Fig. 2.1, we estimate the latter by equating the apparent work needed for full separation to the tensile work done on the probe; i.e., $\pi a^2 G = V_u \int F_n dt$.

Contact imaging and kinematics

During the adhesion tests, we capture videos of the contact from a tilted position above the sample at 30 fps for 0.01 mm/s and 0.1 mm/s unloading cases, and at 240 fps for 1 mm/s and 10 mm/s with 20 μm/pixel resolution, using a smartphone camera (Fig. 2.1(a)). Black paint applied to the plane-side of the probe absorb light and thus provide a dark/bright contrast between contacting and non-contacting parts of the gel surface. For instance, the inset figures in Fig. 2.1(c) show images of the contact region at unloading rate of $V_u = 1$ mm/s and dwelling time of $t_{\text{dwell}} = 0.5$ s. In Fig. 2.1(c), the inset figures correspond to the start of unloading, the maximum pull-off force F_p, and right before full separation, respectively. Because of the tilted camera view, the contact areas appear elliptical instead of circular. Nevertheless, we calibrated the camera images against

known physical lengths along the center of the sample so that we could record contact diameter, $2a$ as the length of the major axis of the ellipse. Note that in addition to the poroviscoelastic relaxation time scales, there is another time scale at which delayed contact peeling (crack opening) or formation (crack closure) can occur in rate-dependent materials (Müller and Müser, 2023). For soft materials at the mm contact sizes, that time scale is orders of magnitude larger than the poroviscoelastic time constants that we observed in gelatin. Hence, we have not observed any significant change in contact area during dwelling portion of our tests. We track the evolution of contact radii over the duration of unloading and then define the crack velocity $V_c = |da/dt|$ at the instance of pull-off. To lessen the influence of noise, a spline derivative with a smoothing parameter $s = 5$ is used to compute the crack velocities.

2.3 Results and Discussions

Enhancement of gel adhesion

Fig. 2.2(a) and (b) illustrate the variation in pull-off force F_p and apparent work of adhesion G as a function of unloading rate V_u at different dwelling times. As a measure of repeatability, four repetitions of each case are encapsulated in the shaded strips. The apparent work of adhesion $G = 74.8\ \mathrm{mJ/m^2}$ that we measured at $t_{\mathrm{dwell}} = 0.5\ \mathrm{s}$ and $V_u = 0.01\ \mathrm{mm/s}$

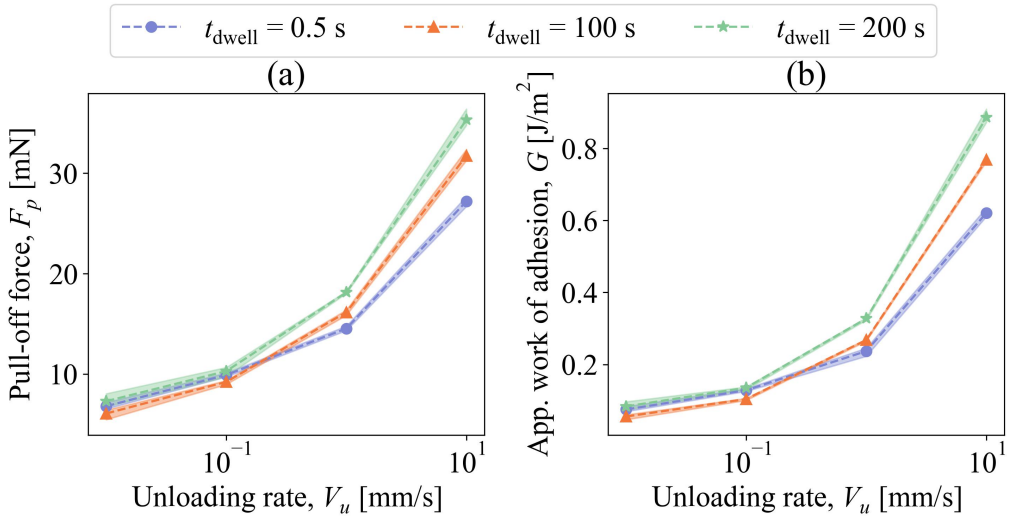

Figure 2.2: Results of the adhesion experiments: (a) The pull-off force F_p plotted against the unloading rate V_u. (b) The apparent work of adhesion G plotted against the unloading rates. The shaded area in the plots represents the range between the maximum and minimum values.

is comparable to the thermodynamic work of adhesion $\Delta\gamma \sim 85\ \mathrm{mJ/m^2}$ found by Khakalo et al. (Khakalo et al., 2017) for a type A porcine skin gelatin ($\sim$ 10 to 20 w/v%). Therefore, we will take $G = 74.8\ \mathrm{mJ/m^2}$ as a reasonable estimate of thermodynamic work of adhesion $\Delta\gamma$ in the upcoming analysis. The largest apparent work of adhesion that we recorded is $G = 886\ \mathrm{mJ/m^2}$, which is about one-third the cohesive strength reported as the fracture energy ($\sim 2500\ \mathrm{mJ/m^2}$) by Baumberger et al. (Baumberger et al., 2006a) for a type A porcine skin gelatin (5 w/v%) at quasistatic crack velocities.

Both adhesion measures reveal strong enhancement with unloading

rates V_u; e.g., $\sim$ 5-fold and 10-fold increase in pull off force and apparent work of adhesion, respectively. Increasing dwelling times t_{dwell} contributes to that enhancement but rather weakly compared to the unloading rates. This dependence on unloading rate and dwelling time is in line with previous observations of (Serrano, 2019; Cedano-Serrano et al., 2019), where more than an order of magnitude increase in work of adhesion (from 60 to 1000 mJ/m^2) was obtained in Milli-Q water between poly(MAETAC-co-AAm) hydrogel and a PAA hydrogel thin film when the unloading rate was increased from 1 to 1000 $\mu m/s$. The same authors also found that increasing contact time from 1 to 1200 s lead to 2-fold increase in work of adhesion of the same materials. Maximum enhancement that we observed due to increasing dwelling time is 40%; e.g., the apparent work of adhesion G increases from 621 to 886 mJ/m^2 at $V_u = 10$ mm/s, as t_{dwell} increases from 0.5 to 200 s. Glass-probe on gel configuration that we tested can lead to different contact physics, especially poroelastic effects when compared to the gemini configuration that Ref.(Serrano, 2019) studied. Similar configuration-dependent differences were shown in friction and lubrication properties of polyacrylamide gels (Dunn et al., 2015).

Viscoelastic enhancement

Contact kinematics and its dependence on unloading rates and dwelling times could potentially explain the enhancement observed in adhesion. We plot the evolution of contact radius during unloading stage of the tests

at $t_{\text{dwell}} = 0.5$ s for different unloading rates in Fig.2.3(a). For illustration

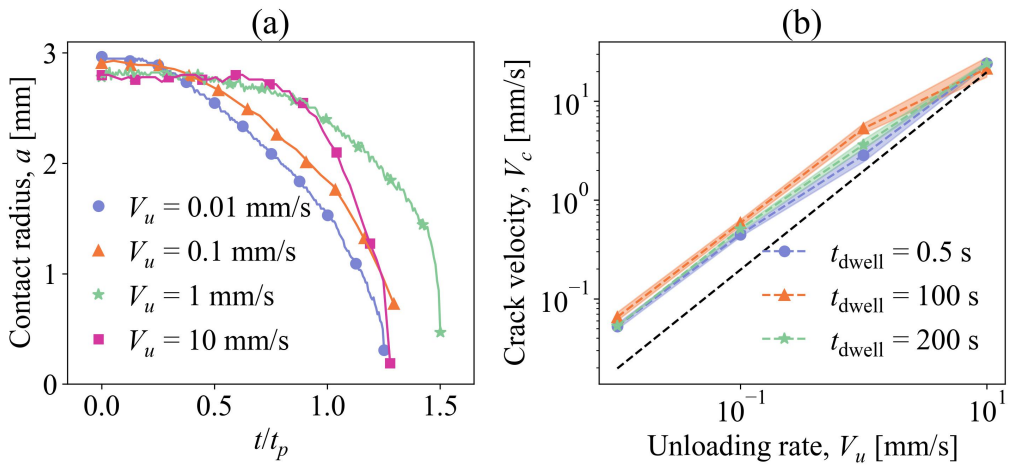

Figure 2.3: Representative (a) evolution of the contact area a as a function of time t during unloading at a dwelling time of $t_{\text{dwell}} = 0.5$ s. The values of $t_p = \{57.2, 6.20, 0.588, 0.143\}$ correspond to unloading rates of $V_u = \{0.01, 0.1, 1, 10\}$ mm/s, respectively, where t_p is the time when $F = F_p$. (b) The theoretical (represented by the dashed line) crack velocity via viscoelastic JKR model and experimentally estimated (represented by the scatter plot) crack velocity V_c as a function of the unloading rate V_u. The shaded area in the plots represents the range between the maximum and minimum values.

purposes, time is normalized by t_p, where $t_p = \{57.2, 6.20, 0.588, 0.143\}$ is the duration from the start of unloading to the instant when pull-off force F_p is reached. Since time is normalized, the slope of Fig. 2.3(a) is scaled with t_p. Notably, contact radii at pull-off $a_{t=t_p}$ are larger for larger unloading rates. This observation corroborates the numerical work by Afferrante et al. (Afferrante and Violano, 2022). Fig. 2.3(b) shows the crack velocities $|da/dt|_{t=t_p}$ measured at different V_u and $t_{\text{dwell}} = 0.5, 100, 200$ s.

The crack velocities range from 0.05 to 30 mm/s residing well below sonic regime. Besides, the crack velocities exhibit approximately power law scaling with the unloading rates; i.e., $V_c \propto V_u^{0.8}$. To inspect it quantitatively, we project on Fig. 2.3(b) the theoretical crack velocities estimated via viscoelastic JKR model after Greenwood and Johnson (Johnson et al., 1971; Greenwood, 2004; Violano et al., 2021b):

$$V_c = \left|\frac{da}{dt}\right| = \left|\frac{da}{d\delta}\frac{d\delta}{dt}\right| = \left|\frac{da}{d\delta}V_u\right| = V_u / \left(\frac{2a}{R} - \sqrt{\frac{\pi\Delta\gamma}{2aE^*}}\right) \tag{2.1}$$

Here, the apparent work of adhesion $G = 74.8$ mJ/m^2 estimated at $t_{\text{dwell}} = 0.5$ s and $V_u = 0.01$ mm/s is used for $\Delta\gamma$, $E^* = E/(1-\nu^2) = 12.5$ kPa is the reduced modulus estimated from the gel's response to initial loading, and $a = 2.9$ mm is imaged at the start of unloading. Since the denominator of the last expression of Eq. 2.1 is independent of V_u, the theory predicts $V_c \propto V_u$, which is very close to the power law that we obtained experimentally. Besides, quantitative match between the theoretical and experimental contact kinematics suggests the dominance of viscoelastic crack propagation in the unloading phase of the adhesion tests. This is also reflected in the weak dependence of crack velocities to t_{dwell} and thus poroelasticity. We then compute Deborah number $De = \{0.004, 0.034, 0.216, 1.842\}$ as $\tau_{\text{VE}}/(a/V_c)$, which is a measure of the fluidity of materials at different unloading rates $V_u = \{0.01, 0.1, 1, 10\}$ mm/s. We assume $a = 2.9$ mm is constant for all cases, and V_c is inde-

pendent of t_{dwell} for calculation of De. a/V_c is an average time it takes for the crack to propagate over the whole contact. For the slowest unloading $V_u = 0.01$ mm/s, the crack propagates very slowly compared to the viscoelastic relaxation, resulting in $De \ll 1$ and expectedly a fully-relaxed material behavior. In contrast, at the fastest unloading rate $V_u = 10$ mm/s case, the crack opening is faster than viscoelastic relaxation, and the material in the vicinity of contact acts like an unrelaxed elastic solid during unloading. This wide range of expected viscoelastic response prompted us to further inspect crack propagation in viscoelastic media.

For instance, Persson and Brener (Persson and Brener, 2005) assumes that the energy flow to the crack tip can be considered as the apparent work of fracture and can be expressed as the sum of work of fracture and viscoelastic dissipation. Since the latter stems from dissipation capacity of the viscoelastic material (say loss modulus), which itself depends on strain rates, apparent work of fracture is found to change with crack velocity. Applying this idea to power-law relaxation response commonly-observed for rubber compounds between rubbery and glassy time scales, Persson and Brener listed the following relation for the enhancement of work of fracture and crack velocities for various viscoelastic models:

$$\beta_W = \frac{G}{\Delta\gamma} \sim \left(\frac{V_c}{V_{c,0}}\right)^{\alpha} \tag{2.2}$$

Here, $V_{c,0} \ll V_c$ is the characteristic velocity that determines the lower

end of strain rates (frequencies) involved in crack propagation as $V_{c,0}/r_0$, and r_0 is the crack tip radius for quasistatic crack propagation. Note that similar enhancement of work of fracture with crack velocities were shown experimentally on gelatin samples (Baumberger et al., 2006b; Naassaoui et al., 2018). Taking multiple relaxations into account in dynamic modulus $E(\omega)$ of the viscoelastic material:

$$\frac{1}{E(\omega)} = \frac{1}{E_\infty} + \int_0^\infty \frac{H(\tau)}{1 - i\omega\tau}\, d\tau \tag{2.3}$$

Persson and Brener predicted the scaling power in Eq.2.2 $\alpha = (1-s)/(2-s)$ where, $H(\tau)$ is real and positive spectral density function of relaxation times τ; the viscoelastic solid exhibits power-law relaxation with $H(\tau) \sim \tau^{-s}$, and $0 < s < 1$. The power-law relaxation response is known to hold for transition from glassy to rubbery response regimes, as well as for critical sol-gel transitions in gels (Winter and Chambon, 1986; Winter, 1987). Using Eq.2.3, one can show that $E(\omega) \sim \omega^n$ in those transition regimes with $n \sim 1 - s$. Typically, $n \approx 0.5$ for gelation with excessive crosslinks, and $n = 0.6$ to 0.7 for gelation without chemical crosslinks (Winter, 1987). Experimentally, n is found to range from 0.5 to 0.7 for gelatin 5-10 w/v% at room temperature (Ferry, 1980; Hsu and Jamieson, 1993; Kokol et al., 2021; Ahmed, 2017). This range of n values corresponds to the scaling power α ranging from 0.33 to 0.41. In Fig. 2.4(a), we plot β_W as a function of $V_c/V_{c,0}$ for all 48 measurements, and obtain a scaling power of 0.39 ($V_{c,0}$ is

the average of crack velocities obtained at the slowest unloading case). So,

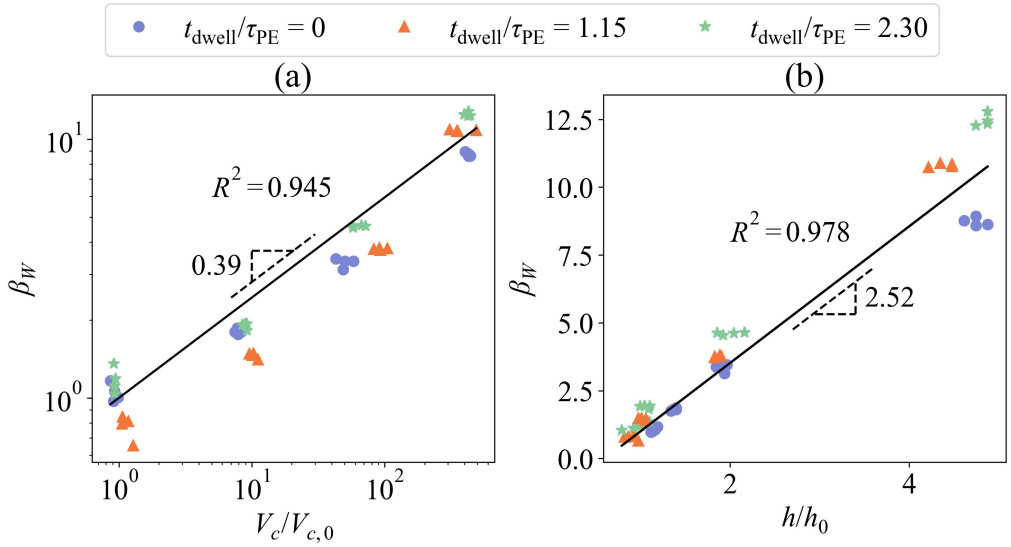

Figure 2.4: Correlation of (a) the enhancement of work of adhesion with the crack velocity ($\beta_W \sim (V_c/V_{c,0})^{0.39}$ with $R^2 = 0.945$), and (b) the enhancement of work of adhesion with the vertical extension ($\beta_W \sim h/h_0$ with $R^2 = 0.978$).

the rate-dependent enhancement that we measured in work of adhesion resides within Persson and Brener's power-law scaling of rate-dependent work of fracture. The scaling law given in Eq. 2.2 applies also for narrower relaxation spectra. For instance, scaling power $\alpha = 0.5$ for standard linear solids with a single time constant τ_0; i.e., $H(\tau) \sim \delta(\tau - \tau_0)$ (Persson and Brener, 2005; Müser and Persson, 2022). With the current setup, we measured the relaxation response (see Appendix A) and identified a single relaxation time constant τ_{VE} to explain the evolution of force at time scales much shorter than poroelastic time constant τ_{PE}. However, an improved

tester (rheometer) is needed to monitor relaxations at broader time scales, and obtain a possible power-law relaxation spectrum (see for instance (Hsu and Jamieson, 1993; Kokol et al., 2021)). To the best of our knowledge, a thorough study that investigates the links between relaxation spectrum and rate-dependent adhesion is missing in the literature. Our findings in line with the Persson and Brener model propose a direct link.

Persson and Brenner model also predicts that the increase in crack tip radius r is linearly proportional to the enhancement of work of fracture of viscoelastic materials; i.e., $\beta_W \propto r/r_0$ regardless of the relaxation spectrum. In our experiments, we use the displacement history and tilted view of the imaging module to estimate the maximum vertical extension of gel h before full separation (see Appendix A). We use the vertical extension as a measure of crack tip radius r due to the difficulties in measuring the crack tip radius with the current imaging module. In Fig. 2.4(b) we plot β_W as a function of h/h_0 for all 48 measurements (h_0 is the average of vertical extensions obtained at the slowest unloading case). Enhancement in work of adhesion correlates linearly with the vertical extensions, re-confirming that viscoelastic deformations, associated dissipation and crack tip kinematics can explain the observed rate-dependence of adhesion. Scaling of enhancement of adhesion with crack velocities and vertical extensions changes negligibly with t_{dwell} suggesting second order influence of poroelastic diffusion on rate-dependent adhesion. More discussion of that subtle influence will follow in §2.3.

Poroelastic enhancement

To better understand the influence of poroelastic diffusion, we plot in Fig. 2.5 β_F and β_W as a function of $t_{\text{dwell}}/\tau_{\text{PE}}$ for different $De = \tau_{\text{VE}}/(a/V_c)$. The term $t_{\text{dwell}}/\tau_{\text{PE}}$ can be thought of as the reciprocal of Péclet number (Pe), quantifying the extent of solvent migration away from the contact region during dwelling. We observe more enhancement of the work of adhesion as $t_{\text{dwell}}/\tau_{\text{PE}}$ increases at $\tau_{\text{VE}}/(a/V_c) = 1.842$ and 0.216. On the other hand, at $\tau_{\text{VE}}/(a/V_c) = 0.004$ and 0.034, the enhancement of work of adhesion is nearly independent of $t_{\text{dwell}}/\tau_{\text{PE}}$ and shows almost constant values. The effect of t_{dwell} on gel adhesion can be explained by the suction effect(Reale and Dunn, 2017). As the dwelling time increases, the solvent under the contact slowly diffuses away until a new equilibrium state is reached (Schulze et al., 2017). This diffusion creates a difference in concentration, leading to the buildup of pressure gradient in longitudinal direction under the contact. Consequently, more force and energy are required to separate the surfaces. For slow unloading cases, the effect of dwelling time on adhesion is minimal. This is because the solvent that diffused away from the contact area has sufficient time to diffuse back and balance the pressure gradient caused by unloading; i.e., negligible suction effect. On the other hand, at higher unloading rates $V_u = 1, 10$ mm/s, the longer the dwelling time, the higher the pull-off force F_p and work of adhesion G due to increased poroelastic diffusion. For those cases,

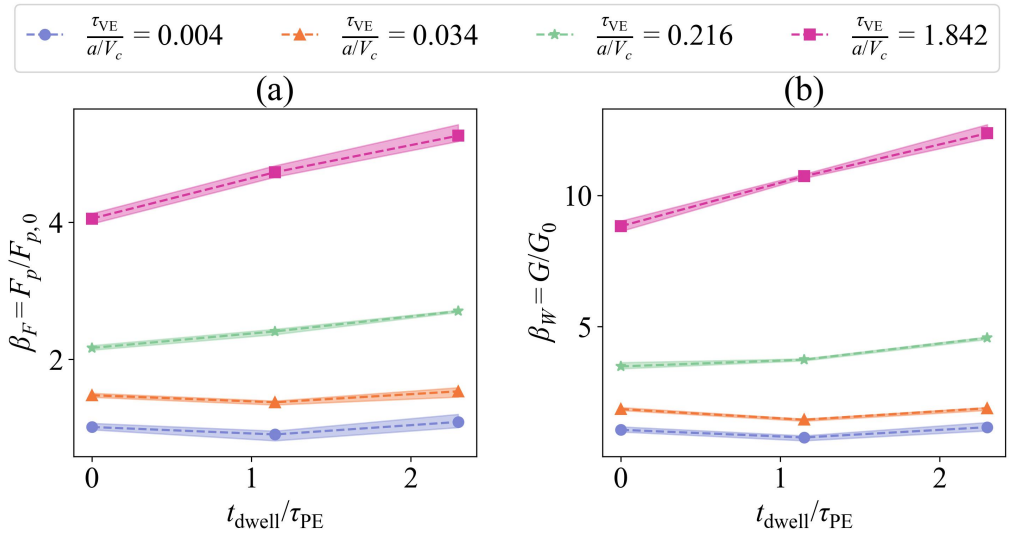

Figure 2.5: The enhancement of adhesion as a function of the normalized holding time $t_{\text{dwell}}/\tau_{\text{PE}}$, based on (a) pull-off force F_p and (b) apparent of work of adhesion G at different $\tau_{\text{VE}}/(a/V_c)$. The shaded area in the plots represents the range between the maximum and minimum values.

the solvent does not have sufficient time to balance the pressure gradient because the interfacial crack propagates through the whole contact much quicker than solvent diffusion; e.g., $(a/V_c)/\tau_{\text{PE}} \sim 1.39 \times 10^{-3}$ for $V_u = 10$ mm/s case.

Gelatin samples exhibit only 40% additional enhancement in apparent work of adhesion with increasing dwelling times at high unloading rates. Much larger enhancement was reported on other types of hydrogels (Reale and Dunn, 2017; Lai and Hu, 2021). For instance, Lai et al. (Lai and Hu, 2021) reported around 4 fold increase in pull-off forces as a function of holding time for wide range of indentation depths (4-30 μm) on 10%

polyacrylamide (pAAm). Unloading times for their experiments were also much smaller than the poroelastic time constant, which suggests that above-mentioned suction effect is possible. The contact loads employed in those tests and associated hydrostatic stresses localized to contact can be estimated as $\sigma_{\text{hyd}} \approx$ 2-5 kPa , which is smaller than the osmotic pressures reported for polyacrylamide $\Pi_{\text{pAAm}} \approx$ 11kPa (Schulze et al., 2017). Poroelastic diffusion will be negligibly small under those loading conditions (Schulze et al., 2017; Shoaib and Espinosa-Marzal, 2018) and thus cannot explain the observed enhancement. This also corroborates with Lai et al.(Lai and Hu, 2021)'s proposal for the mechanism of enhancement: hydrophobic backbone of the polyacrylamide and polystyrene probe pushes the water away from the interface only locally and facilitates more solid-solid bonding. We do not anticipate a similar mechanism in our study as both the glass probe and gelatin samples are hydrophilic. In our tests, the maximum hydrostatic stress beneath the contact is approximately $\sigma_{\text{hyd}} \approx$ 1.1 kPa for all cases, where $\Pi_{\text{gel}} \approx$ 1 kPa (Northrop and Kunitz, 1926). For the fast unloading cases, water does not have time to diffuse back and balance the pressure gradient caused by unloading, and thus suction effect is expected. This can be quantified by the ratio of crack propagation time and poroelastic relaxation time constant; i.e., $(a/V_c)/\tau_{\text{PE}}$, which is 1.17×10^{-2} and 1.39×10^{-3} for $V_u = 1$ and 10 mm/s, respectively, and thus very negligible back-diffusion is expected to occur in those cases. Reale et al. (Reale and Dunn, 2017) reported 5-fold increase in ap-

parent work of adhesion on polyacrylamide gels with increasing dwelling times. In their tests, the maximum hydrostatic stress beneath the contact is around $\sigma_{\text{hyd}} \approx 18$ kPa $> \Pi_{\text{pAAm}} \approx 11$kPa; i.e., larger areal fraction beneath the probe experiences poroelastic suction upon unloading compared to our tests, explaining the greater dwelling-time-induced enhancement compared to ours. Since gelatin exhibits more brittle response than polyacrylamide(Yerrapragada et al., 2023; Li et al., 2014), increasing contact pressures to much greater values than osmotic pressure can lead to local failure, and complicate mechanical response at pull-off.

Another influence of t_{dwell} on gel adhesion could be the change in the solvent/solid fraction around the contact. Increasing t_{dwell} means more solvent diffusion away from the contact, and thus relatively higher solid fraction beneath the probe. When surface energies between probe-on-solvent and probe-on-solid network differ considerably, such changes in solid fraction can influence the total work of adhesion. For instance, Jha et al.(Jha et al., 2022) showed that areal oil-fraction dependence in work of adhesion measured on glass-on-PDMS (polydimethylsiloxane) swollen with silicone oil at different fractions. That influence is expected to be minute for the gelatin samples that we studied here. This is because the surface energies reported for collagen films extracted from various sources (31.4-38.6 mN/m, ref.(Michalska-Sionkowska et al., 2021)) and 4% porcine gelatin gels (37.5 mN/m, ref.(Wang and Hartel, 2022)) are very close and thus relative areal fraction of solid/solvent is not expected

to change the work balance at different dwelling times.

2.4 Conclusion

In this work, we investigated rate-dependent adhesion and its relation to poroviscoelastic response of gelatin. In particular, we conducted adhesion tests on gelatin samples via a custom-built spherical glass probe tack tester and an in-situ imaging module, and revealed correlations between poroviscoelastic relaxations and the enhancement of work of adhesion. We controlled the unloading rates to achieve a broad range of crack (contact edge) velocities that were below sonic regime, and observed an order of magnitude enhancement in the work of adhesion. Power-law scaling between enhancement of work of adhesion and crack velocities followed closely the scaling of work of fracture in viscoelastic materials (the Persson and Brener model). The vertical extensions that we found during adhesion tests scaled linearly with the enhancement of work of adhesion. Similar scaling was predicted for crack tip radius and work of fracture in viscoelastic medium; validating that viscoelastic deformations, and associated dissipation and crack tip kinematics govern the observed rate-dependent enhancement of adhesion in gelatin. We also varied the dwelling times and thus degree of poroelastic diffusion beneath the probes, and studied their influence on adhesion. We observed about 40% additional enhancement of the work of adhesion with increasing dwelling times for fast cracks. For

slow cracks, the dwelling times did not influence the work of adhesion. Those observations were in line with the suction effect previously reported elsewhere: when the interfacial cracks are faster than diffusion rates, the solvent does not have sufficient time to balance the pressure gradient and that leads to increase in adhesion. Pull-off and contact forces that we employed lead to hydrostatic stresses sligthly greater than the osmotic pressure of the gelatin. Therefore, dwelling-time-induced enhancement is minute compared to the viscoelastic enhancement. In summary, our results point at viscoelastic relaxations as the dominant mechanism governing the rate-dependent enhancement of adhesion in gelatin. Therefore, tuning relaxation spectrum of gels by chemistry, concentration and ambient conditions could provide a desirable rate-dependence in adhesion. Since adhesion and friction are inherently correlated to each other for soft multiphasic materials, e.g. ref. (Han and Eriten, 2018a), tuning friction response is also possible in a similar fashion.

3 CHAPTER3. TRANSIENTS IN RATE-DEPENDENT ADHESION OF GELATIN*

(*This work has been submitted to Tribology Letters and is currently under review)

3.1 Introduction

Adhesive contact in soft materials are ubiquitous in various natural and engineering systems. For instance, articular cartilage, a soft multi-phasic material cushioning joints, is known to exhibit the rate-dependent adhesion and adhesive friction (Han and Eriten, 2018b; Han et al., 2020c; Benson et al., 2024). Other examples of soft adhesive contacts can be seen in indenter-foam dampers (Han et al., 2020b; Liu et al., 2022; Dalisay et al., 2022), soft robotic grippers (Shintake et al., 2018; Yi et al., 2024), food industry (Vandenberghe et al., 2017; Li et al., 2017b), biomechanics (Dunn et al., 2013), biosensors (Erfkamp et al., 2019; Xu et al., 2024), and bio-adhesives (Michel et al., 2019; Nam et al., 2024; Ma et al., 2024; Wang et al., 2024). Typically in soft adhesive contacts, more external work and force are required to separate surfaces at higher retraction rates primarily due to rate-dependent (poro-viscoelastic) energy dissipation (Persson and Brener, 2005; Greenwood and Johnson, 1981). Between the 70s and the early 2000s, several fracture-mechanics-based models were postulated for

the viscoelastic adhesive contacts (Schapery, 1975; Greenwood and Johnson, 1981; de Gennes, 1996; Persson and Brener, 2005; Gent and Schultz, 1972). Those models focus on non-inertial regime of crack growth (unloading/retraction speeds significantly smaller than shear wave speeds c_s, i.e., $V_u \ll c_s$ in Figs. 3.1a, b), adopt simple relaxation dynamics of the material response (e.g., single relaxation time scale in (Greenwood and Johnson, 1981) and power-law relaxation in (Persson and Brener, 2005)), and explain contributions of dissipation to the apparent work of fracture and adhesion. When adhesive peeling occurs much more quickly or more slowly than relaxation time scales, the material response can be considered as unrelaxed or fully-relaxed, respectively. Hence, work of adhesion and pull-off forces can be estimated from conventional adhesion models (e.g., JKR model for short range adhesive interactions (Johnson et al., 1971)). In between those asymptotes (moderate peeling rates), the energy dissipation by the viscoelastic deformations is no longer negligible and often larger than the surface energy. This behavior is well described by the S-curves presented in Refs (Greenwood and Johnson, 1981; Greenwood, 2004; Persson and Brener, 2005; Persson, 2021), also shown in Fig. 3.1(c) for $k = E_\infty/E_o = 0.1$. Here, G and $\Delta\gamma$ are the apparent and thermodynamic work of fracture/adhesion, respectively, and $\hat{v}$ is the normalized crack velocity (Greenwood, 2004). This so called S-curve is only applicable to half-space geometry. Extensions to finite-sized domains show deviations from the S-curve (Persson, 2017).

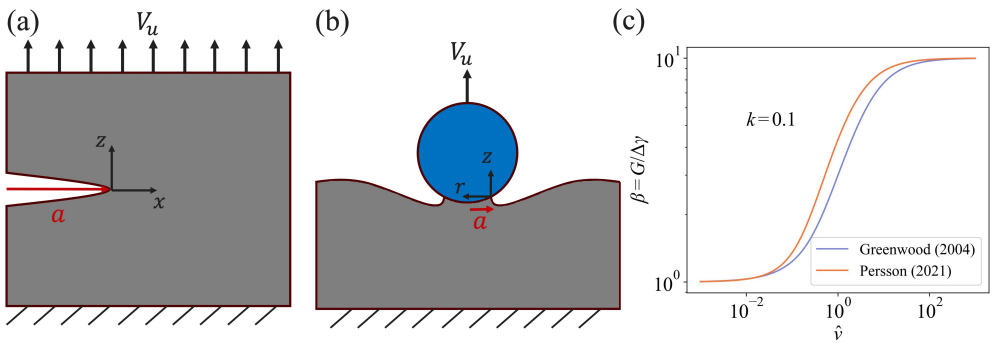

Figure 3.1: (a) Crack propagation with Mode I opening. a represents the crack length. (b) Crack propagation in the spherical adhesive contact. a denotes the contact radius. (c) S-curve illustrating the rate-dependent work of adhesion in viscoelastic half-space with the relaxation degree $k = E_\infty / E_0 = 0.1$ from Refs (Greenwood, 2004; Persson, 2021).

The most typical loading used in fracture testing is Mode I loading as shown in Fig. 3.1(a)(ASTM International, 2018), where the sample is considered to be under plane stress or strain conditions, and the crack is assumed to propagate in perpendicular direction to loading (e.g., x-direction in Fig. 3.1(a)) and reach steady velocities quickly for viscoelastic materials (Knauss, 1969). In the probe tack experiments as in Fig. 3.1(b), the crack kinematics is more complicated. The interfacial crack kinematics is coupled to probe motion nonlinearly often leading to interfacial crack acceleration until snap off (Haiat et al., 2003; Liu et al., 2018; Violano et al., 2021a; Afferrante and Violano, 2022; Argatov et al., 2023; Lee and Eriten, 2024; Argatov et al., 2024; Tricarico et al., 2025). Because of that, rate-dependence of apparent work of adhesion measured by probe tack testers is reported with respect to a representative crack velocity; typically

the crack velocity measured at the instance of pull-off (maximum tensile) force (Lee and Eriten, 2024; Violano and Afferrante, 2022; Müser and Persson, 2022; Maghami et al., 2024). Since rate-dependence in work of adhesion is expressed in crack velocities V_c (e.g., the Gent-Schultz law (Gent and Schultz, 1972), $G(V_c) = \Delta\gamma + C\log(V_c/V_c^*)$), non-stationary crack velocities infer transients in crack-driving energetics during a probe tack experiment. There are numerous examples of those transients in the literature: Argatov et al. studied rate-dependent decohesion process between a cylindrical punch and an elastic substrate using Gent-Schultz law (Argatov et al., 2023; Gent and Schultz, 1972); oscillatory response of viscoelastic contacts where crack velocities range from positive (opening) to negative (closing) values even in a single loading cycle were explored in (Greenwood and Johnson, 2006; Wahl et al., 2006; Dalbe et al., 2013; Shui et al., 2020; Yi et al., 2024; Tricarico et al., 2025). A major assumption in those studies is that the constitutive relation between crack velocities and apparent work of adhesion holds even when crack velocities change instantaneously. That assumption surely fails during two instances of those transients: at the initiation of crack propagation (around zero crack velocities) and close to full separation, when crack velocities can increase unstably often leading to snap off. In the latter case, even if snap off instability is suppressed, the contact radius is small so that there is limited material volume ahead of crack tip for viscoelastic dissipation; referred to as finite-size effect (de Gennes, 1996; Persson, 2017). For instance, large

oscillations around resonances documented in Refs. (Shui et al., 2020; Yi et al., 2024; Tricarico et al., 2025) would lead to rapid orders of magnitude change in crack velocities and large reductions in contact radius; and so potential deviations are expected from crack velocity-energetics relations such as Gent-Schultz law(Gent and Schultz, 1972). To the best of our knowledge, no prior study had documented and commented on those potential deviations during transients.

Here, we document those transients in a monotonically unloaded spherical probe on gelatin. In particular, we report the transients in energetics and crack velocity experimentally. Particularly in Section 3.2, we first present the experimental observations in line with our previous work(Lee and Eriten, 2024) and discuss the change of crack velocity and the instantaneous work of adhesion. We estimate the instantaneous crack velocity from the images of the contact area and compute the instantaneous work of adhesion using JKR theory(Johnson et al., 1971). In Section 3.3, we adapt de Gennes' thought model (de Gennes, 1996), incorporating minor modifications to account for viscoelastic losses and finite-size effects during peeling, in order to interpret our experimental results. The model yields the evolution of instantaneous work of adhesion, and we compare that evolution with experiments. We find deviations in the crack energetics and velocity during initiation of crack propagation and close to full separation, and the model captures most of those observations. In Section 3.3, we discuss the limitations and assumptions of the experiments and model.

Our results demonstrate the importance of transients during peeling in probe tack adhesion tests in soft poroviscoelastic materials. A predictive adhesive contact model should incorporate transients especially if the application involves crack initiation and close-to-full-separation states.

3.2 Experimental Results

In our previous study(Lee and Eriten, 2024), we conducted probe-tack adhesion tests for 5 w/v% porcine gelatin (G2500 Type A, Sigma Aldrich, Inc.) as shown in Fig. 3.2(a). To ensure reproducibility and provide context for the new analyses, we briefly revisit the experimental methodology below. A glass probe with radius $R = 10.54$ mm first was indented on optically smooth and flat gelatin samples (50 mm radius and 15 mm thickness). The indentations were conducted at 10 mm/s with 0.5 mm of maximum depth δ followed by 0.5 s of dwelling(holding) time. The probe was then unloaded at four different unloading rates $V_u = 0.01, 0.1, 1, 10$ mm/s until full-separation. The tests were repeated four times at each unloading rate. The linear actuator has large accelerations (≈ 300 mm/s^2). At $V_u = 10$ mm/s, it takes around 0.03 s to reach 10 mm/s with around 0.15 mm of displacement, ensuring that we have $V_u = 10$ mm/s in tensile regime ($F \leq 0$). The force F was measured by a load cell attached to the probe with 50 ¯N resolution at 400 Hz sampling frequency. A LVDT sensor (resolution 0.1 ¯m) measured the displacement of the linear actuator at

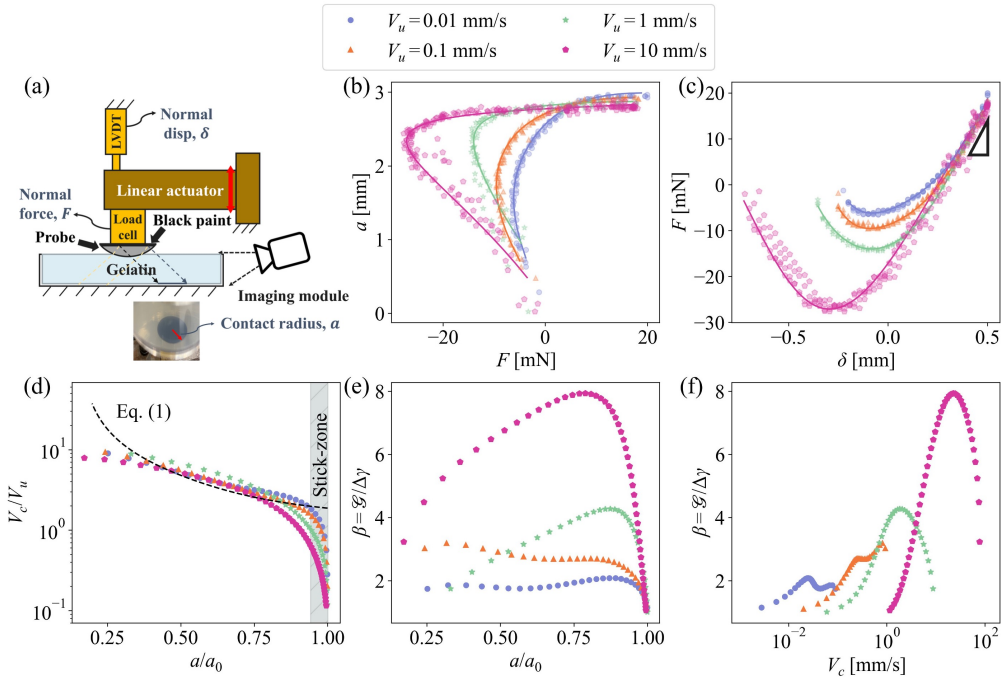

Figure 3.2: (a) The sketch of the experimental setup and a contact image captured by the imaging module. (b) The contact radius a as a function of force F (tensile negative) and (c) the force F as a function of displacement δ for different unloading rates V_u. (d) Representative V_c/V_u vs. a/a_o curve for different unloading rates. The black dashed line is plotted by Eq. 3.1(Violano et al., 2021b). Representative normalized energy release rate $\mathcal{G}/\Delta\gamma$ as a function of (e) the dimensionless contact radius a/a_0 and (f) the crack velocity V_c. $\Delta\gamma_o$ corresponds to the thermodynamic work of adhesion as $\Delta\gamma = \int Fd\delta/\pi a_o^2 = 0.07\,\mathrm{J/m^2}$ for $V_u = 0.01$ mm/s. $a_o \approx 2.95$ mm is the initial contact radius before unloading. V_c and G are estimated from the contact radius reached 5% reduction of its initial contact radius a_o. The experimental data is from Ref (Lee and Eriten, 2024) for 5 w/v% porcine gelatin hydrogel.

400 Hz sampling frequency. The stiffness of the load cell was 1000 N/m, about 20-fold the contact stiffness, and hence, the displacement of the actuator δ was close to the total deformation of the gelatin. The reduced

modulus of gelatin $E^* = 12.5$ kPa is estimated from the loading curve (Lee and Eriten, 2024) (Poisson's ratio $\nu \approx 0.49$). The relaxed modulus value is close to the modulus estimated at low frequency ($E = 12$ kPa, assuming $\nu \approx 0.49$) for 5 wt% gelatin in Ref(Baumberger et al., 2002). We employed an imaging module (spatial resolution 20 ¯m/pixel; 240 fps for 1 mm/s and 10mm/s; 30 fps for 0.01 mm/s and 0.1 mm/s) to trace the contact radius a evolution during unloading (see Ref(Lee and Eriten, 2024) for more details on the experiments). In an earlier paper, we had presented rate-dependent pull-off force and work of adhesion in gelatin only as a function of crack velocities at pull-off. As discussed above, this representation fails to reveal the transients in both kinematics and energetics of peeling in a probe-tack experiment. In this study, we present the evolution of forces, displacements, crack velocities and contact radii during each probe-tack experiment, and explore the link between instantaneous crack velocities and work of adhesion. Our findings that include accelerating cracks despite non-monotonic energetics contradict the rate-dependence of work of adhesion measured at steady-state conditions, and thus show the importance of transients stemming from nonlinear kinematics and loading history.

The experimental data for F, a, and δ are shown in Fig. 3.2(b-c). Fig. 3.2(b) shows the contact radius a as a function of the force F for the different unloading rates. To compensate for the different sampling rates used for a and F, a quadratic interpolation was conducted between data points.

The scatter points in Fig. 3.2(b–c) represent data from four experimental repetitions, while the solid line corresponds to an interpolated curve from one representative trial selected among them. In Fig. 3.2(c), the slope of $F - \delta$ around the start of unloading curve (a small right triangle) delivers the contact stiffness of the material. The stiffness for four different unloading rates are almost identical(a remains almost constant in the initial regime of the unloading at around 3 mm). This tells that the unloading rate may be sufficiently slow for the bulk deformation, and that the bulk behavior of the material exhibits less rate-dependency within the range of unloading rates $V_u = [0.01 - 10]$ mm/s (Greenwood and Johnson, 2006).

Fig. 3.2(d) shows the crack velocity $V_c = |da/dt|$ normalized by the unloading rate V_u as a function of contact radius a/a_0 at different unloading rates, where a_0 is the initial contact radius. As shown in Fig. 3.2(b), the contact was stuck (Violano et al., 2021b) during the initial stage of unloading. In this regime, the contact radius remained almost constant at a_0 and thus the crack velocity $V_c \approx 0$ due to viscoelastic dissipation and delayed fracture at the contact edge. As a result, the evolution of contact radius and crack velocity in this regime can deviate from classical elastic predictions such as those of JKR theory. We identified the regime where the contact radius reduces by 5% of its initial value a_0 to be the stick-zone as shown in Fig. 3.2(d). The dashed line in Fig. 3.2(d) represents the theoretical kinematic relation between crack and probe motions; V_c/V_u in

the JKR limit given as (Violano et al., 2021b)

$$V_c/V_u = \left(\frac{2a}{R} - \sqrt{\frac{\pi\Delta\gamma}{2aE^*}}\right)^{-1}. \tag{3.1}$$

Here, the thermodynamic work of adhesion, $\Delta\gamma = 0.07\,\mathrm{J/m^2}$, is estimated from Fig. 3.2(c) using $\pi a_0^2\Delta\gamma = \int F, d\delta$ for $F \leq 0$ at $V_u = 0.01$ mm/s. Measurements at lower unloading velocities yielded nearly identical results, and thus the value obtained at 0.01 mm/s is taken as the thermodynamic work of adhesion. In our previous work (Lee and Eriten, 2024), we computed the apparent work of adhesion G as $\pi a_0^2 G = \int F, d\delta$ for $F \leq 0$, and found G shows a power-law dependence on the representative crack velocity $V_{c,p}$ at the instant of pull-off, with an exponent of 0.39 for gelatin. This finding closely agrees with theoretical predictions reported in Ref(Persson and Brener, 2005). Note that during transients, the ratio of $\Delta\gamma$ to E^* is expected to be a function of V_c. Interestingly, V_c/V_u at all unloading cases cluster around theoretical V_c/V_u predictions except for the beginning of the unloading (initiation) and close to the full separation; $a/a_0 > 0.9$ and $a/a_0 < 0.4$, respectively. The mismatch between the experimental value and the theoretical value in $a/a_o > 0.9$ or $a/a_o < 0.4$ is likely to stem from the poro-viscoelasticity of the gelatin, i.e., rate-dependent $\Delta\gamma/E^*$. The largest crack velocity 70 mm/s measured at $V_u = 10$ mm/s was about two orders of magnitude smaller than the shear wave speed; $c_s \approx 1.7$ m/s (shear modulus 3 kPa and density 1000 $\mathrm{kg/m^3}$), which ensured that

the inertia was negligible. Besides, the cracks accelerated monotonically during peeling. This implies that the instantaneous work of adhesion G and so enhancement of apparent work of adhesion β will also vary significantly during peeling. Since we do not have full-field measurements in the experiments such as crack opening or local strain, we cannot estimate actual crack-driving energetics and exact work of adhesion instantaneously. However, using the measured force and contact radius evolution, we can obtain instantaneous change in potential energy of the system per unit reduction in contact area; similar to J-integral concept. We define that quantity as instantaneous energy release rate $\mathcal{G} \equiv d\Pi/dA$, where Π is the potential energy of the system, and A is the contact area $A = \pi a^2$. Here, for viscoelastic materials, $\mathcal{G}$ is known to depend on the crack velocity thanks to viscoelastic dissipation (Schapery, 1975, 1989; McCartney, 1977). However, as stated above, we do not have a viable way to quantify losses in the gel. Instead, motivated by Greenwood and Johnson (Greenwood and Johnson, 2006), we assume that the bulk dissipation was negligible and the energy dissipation localized near the crack tip. Considering elastic bulk deformation with the relaxed modulus $E^*_\infty = E_\infty/(1-\nu^2) = 12.5$ kPa and large probe radius R used in the experiments lead to short-range adhesion assumption to hold as in the JKR model (Tabor, 1977; Johnson et al., 1971). Accordingly, elastic strain energy U and the mechanical work

done W are given as(Johnson et al., 1971)

$$U = \frac{45F^2R + 16a^6E^{*2}/R}{180E^*aR}, \tag{3.2}$$

$$W = \frac{3F^2R + 2Fa^3E^*}{6E^*aR}. \tag{3.3}$$

Expressing the potential energy as $\Pi = U - W$, the following equation for the energy release rate is obtained:

$$\mathcal{G} \equiv \frac{d\Pi}{dA} = \frac{d\Pi}{2\pi ada} = \frac{\left(4E^*a^3/3R - F\right)^2}{8\pi E^*a^3}. \tag{3.4}$$

Fig. 3.2(e-f) shows the variation of $\mathcal{G}$ as a function of normalized contact radius a/a_0 and crack velocity V_c. The energy release rate $\mathcal{G}$ is normalized by $\Delta\gamma$, which represents the thermodynamic work of adhesion estimated at the slowest unloading rate (Lee and Eriten, 2024). The transient behavior of β with the increase of the crack velocity exhibits distinct contrast to the S-curve shown in Fig. 3.1(c). As the peeling proceeds, the energy release rate evolved non-monotonously: at initial stages of peeling, it increased up to a maximum value and closer to the full separation decreased. At low unloading rates, the energy release rate $\mathcal{G}$ exhibits local maxima; however, it remains approximately constant throughout most of the peeling process. This trend is particularly evident at unloading rates of $V_u = 0.01$ and 0.1 mm/s. At higher unloading rates 10 mm/s, the maximum $\mathcal{G}$ is reached earlier at around $a/a_0 \approx 0.8$. Moreover, the crack velocity at which $\mathcal{G}$

begins to turn over is not constant but varies with the unloading rate. This result contradicts the theoretical predictions of viscoelastic crack propagation models that account for finite-size effects (Persson, 2017; de Gennes, 1996). We hypothesize that the non-monotonic evolution of $\mathcal{G}$ arises from crack acceleration and finite-size effects, specifically the shrinkage of the contact area. At low unloading rates, the viscoelastic dissipation zone is small and confined to the crack tip. At high unloading rates, the dissipative zone grows and becomes comparable to a_0 very quickly. Hence, reduction in $\mathcal{G}$ starts at earlier stages of peeling when $a \approx 0.8a_0$. Besides, the maximum $\mathcal{G}$ values increased from 2 to 8 times $\Delta\gamma$ with the unloading rate. The increase in the maximum energy release rate is in line with the expected increase of viscoelastic dissipation with the unloading rate (Persson and Brener, 2005). The trends observed in the evolution of $\mathcal{G}$ and the crack velocity at which $\mathcal{G}$ begins to turn over in our experiments can be qualitatively explained using a simple conceptual model inspired by de Gennes (de Gennes, 1996).

3.3 Discussion

Qualitative comparison with de Gennes' viscoelastic crack propagation model

For qualitative examination, we compare our experimental results in ERR to the theoretical model developed by de Gennes(de Gennes, 1996) by employing SLS model. We assume that the normal traction $\sigma = \sigma_{zz}$ acts over the process zone during crack propagation (e.g., Dugdale-type tensile traction(Dugdale, 1960; Maugis, 1992) at the edge of the contact area), and the energy is dissipated by viscoelasticity around that process zone. With those definitions, when the crack propagates by da for the time instant dt, instantaneous energy balance can be written as

$$2\pi a\dot{a}\mathcal{G} = 2\pi a\dot{a}\Delta\gamma + 2\pi a \int \sigma\dot{\varepsilon}2\pi r dr, \tag{3.5}$$

where $\Delta\gamma$ and $\mathcal{G}$ are the thermodynamic work of adhesion and the energy release rate (or the apparent work of adhesion). The first term on the right hand side comes from the surface energy term to create the new surface $dA = 2\pi a da$, whereas the second term accounts for the viscoelastic dissipation as the crack propagates. The modifications will be in estimation of the viscoelastic dissipation and bounds of the dissipation integral. According to Refs (Persson and Brener, 2005; Persson, 2017; Saulnier et al.,

2004), the lower and upper cut-offs of the frequency in the dissipation term are determined by $|\dot{a}|/a$ and $|\dot{a}|/\rho$, respectively (ρ is the crack tip radius). Those cut-offs can be incorporated in Eq. 3.5 to yield

$$\beta = \frac{\mathcal{G}}{\Delta\gamma} = 1 - \alpha E_o \int_{\dot{a}/a}^{\dot{a}/\rho} \mathrm{Im}\left\{\frac{1}{E(\omega)}\right\}\frac{1}{\omega}d\omega. \tag{3.6}$$

where α is a constant of order unity. Note that in our experiments, asymptotic values of β as $a \to a_0$ and $a \to \rho$ correspond to initial and final stages of peeling, respectively. One can define the bandwidth of viscoelastic dissipation as the difference between the bounds of integral, i.e., $\Delta\omega \sim |\dot{a}|(1/\rho - 1/a_0)$. Since crack tip radius is expected to be much smaller than the initial contact radius, at the initial stages of peeling $a \approx a_0$, $1/\rho - 1/a_0$ is large, but $\dot{a} \approx 0$. Therefore, the dissipation bandwidth $\Delta\omega \approx 0$, which results in no enhancement in work of adhesion, i.e., $\beta \approx 1$. Similarly, close to separation, $a \to \rho$, $\Delta\omega \to 0$, and thus $\beta \to 1$. In between those two asymptotes, enhancement of work of adhesion β must attain a maximum value when $\rho < a < a_0$. That aspect of the model qualitatively matches the experimental observations shown in Fig. 3.2(e).

To estimate β from Eq. 3.6, one needs the function form of $E(\omega)$; the rheological response of the material around the process zone. Standard linear solid model (SLS model) is often used to approximate the rheological response of gels and elastomers for simplicity (Benkherourou et al., 2000; Ottone et al., 2005; Yengul et al., 2019), but a more robust way would

be to explore broader relaxation spectra as observed in measurements via rheometry (VanDonselaar et al., 2023; Han et al., 2020a), elastography (Budelli et al., 2016; Yengul et al., 2019), AFM (Nia et al., 2013; Hellwig et al., 2016), and creep tests (Higgs and Ross-Murphy, 1990; Normand and Ravey, 1997). For simplicity and brevity, we will also use the SLS model, where $\text{Im}\{1/E(\omega)\} = \frac{-\tau\omega}{E_0 k[1+(1+k)^2\tau^2\omega^2]}$ with $k = E_\infty/E_0$, and E_0, E_∞, and τ are the unrelaxed and relaxed moduli, and the relaxation time constant. When we substitute that expression into Eq. 3.6 and evaluate the integral, we obtain the enhancement of work of adhesion $\beta = \mathcal{G}/\Delta\gamma$ as

$$\beta = 1 + \frac{2}{\pi k(1+k)}\left[\tan^{-1}\left((1+k)\eta|\hat{a}'|\right) - \tan^{-1}\left((1+k)\frac{|\hat{a}'|}{\hat{a}}\right)\right]. \quad (3.7)$$

where we set $\alpha = 2/\pi$ to ensure that at high crack velocities $\dot{a}$ and large contact radius a, $\beta \approx 1/k$ as predicted by theoretical models (Greenwood, 2004; Persson and Brener, 2005), and employed non-dimensional variables $\hat{t} = t/\tau$, $\hat{a} = a/a_0$, and $\eta = a_0/\rho$. Note that a_0 is the initial contact radius and $\hat{a}' = d\hat{a}/d\hat{t}$ is the dimensionless crack speed. To numerically study Eq.3.7, we prescribe the evolution of the contact radius during peeling as $\hat{a} = 1 - \text{De}^2\hat{t}^2$. This simple quadratic form is motivated by experimental observations reported in our previous work (Lee and Eriten, 2024), which suggest that the contact radius decreases approximately parabolically with time. Here, De is the dimensionless Deborah number, defined as the ratio of the relaxation time τ to the characteristic peeling

time t_p, such that $\hat{a} = 0$ when $\hat{t} = 1/\mathrm{De}$. Substituting that $\hat{a}$ in Eq. 3.7, the enhancement of work of adhesion turns into a function of the non-dimensional time as $\beta = \beta\left(\hat{t}; \mathrm{De}, \eta, k\right)$. As mentioned above, that function takes a value of 1 in the peeling initiation and close to full separation regimes regardless of the parameters De, η, k. So, between those two limits lies a $\hat{t}_{\max}$, $0 \leq \hat{t}_{\max} \leq 1/\mathrm{De}$, when β reaches a maximum value, $\beta_{\max}$. The value of that maximum enhancement and at what contact radius $\hat{a}_{\max}$ it occurs depend on the parameters De, η and k.

Fig. 3.3(a) and (b) show contour plots of $\hat{a}_{\max}$ and $\beta_{\max}$ for a range of De, η values. To obtain those contour maps, we set $1/k = 10$ which covers the maximum enhancement of work of adhesion that we reported in our earlier work (Lee and Eriten, 2024). η corresponds to small crack tip radii relative to initial contact radius, and De values covers slow to fast peeling regimes relative to relaxation times around the crack tip. Contact radii where maximum enhancement is reached, $\hat{a}_{\max}$ qualitatively illustrate the finite-size effect during peeling, i.e., if maximum enhancement is reached at the initial stages of peeling $\hat{a}_{\max} \approx 1$. The subsequent reduction in instantaneous release rate is due to the finite-size effect. That regime occurs when $\mathrm{De} \gtrsim 10^{-2}$ corresponding to fast unloading or crack velocity. In contrast, at low unloading rates $\mathrm{De} \lesssim 10^{-3}$, $\hat{a}_{\max} \approx 0$ and thus, finite-size effect is observed only at the close-to-separation stage. For that part of the contour map, $\hat{a}_{\max}$ depends only on η, scaling by $\hat{a}_{\max} \sim \eta^{-0.5}$. As expected, in the limit of very small Deborah number and crack tip radius

ρ, a typical JKR contact without any finite-size effect is recovered. The contours of $\beta_{\max}$ are shown in Fig. 3.3(b) for the same ranges of η and De values. At constant η, $\beta_{\max}$ tends to increase with De, i.e., unloading rates. This tendency is consistent with the experimental observations shown in Fig. 3.2(e-f). At constant De, $\beta_{\max}$ increases with η as well. Both tendencies can be explained by the dissipation bandwidth, defined as the difference of upper and lower bounds of the integral in Eq. 3.6; $\Delta\omega \sim |\dot{a}|(1/\rho - 1/a_0)$. This can be normalized as $\tau\Delta\omega \sim |\hat{a}'|(\eta - 1)$. Recognizing $\eta \gg 1$ and substituting $\hat{a}' = -2\mathrm{De}^2\hat{t}$ into that expression yields $\tau\Delta\omega_{\max} \sim 2\mathrm{De}^2\hat{t}_{\max}\eta$ for the normalized dissipation bandwidth at the instant of $\beta_{\max}$. Except for extreme values of De, i.e., very high and slow unloading rates, $\hat{t}_{\max} \sim 1/\mathrm{De}$; so, $\tau\Delta\omega_{\max} \propto \mathrm{De}\,\eta$, as do the $\beta_{\max}$ values for the same ranges of De and η.

The experimental results shown in Fig.3.2 are projected on Fig. 3.3(a-b) via the following assumptions. Since the experiments could not resolve the radius or viscoelastic relaxations around the crack tip, i.e., τ, k and ρ, projections can only be reasoned through matching observed $\beta_{\max}$ values with reasonable combination of De and η. Given that the elasto-adhesive length $\mathcal{G}/E$ and the crack-tip radius ρ are of the same order of magnitude for soft viscoelastic materials (Creton and Ciccotti, 2016), ρ is estimated using the the elasto-adhesive length, i.e., $\mathcal{G}/E$. For instance, markers A through D match the experimental $\beta_{\max}$ values observed at $V_u = 0.01, 0.1, 1, 10\,\mathrm{mm/s}$, respectively. The De and η values of those markers were found respectively

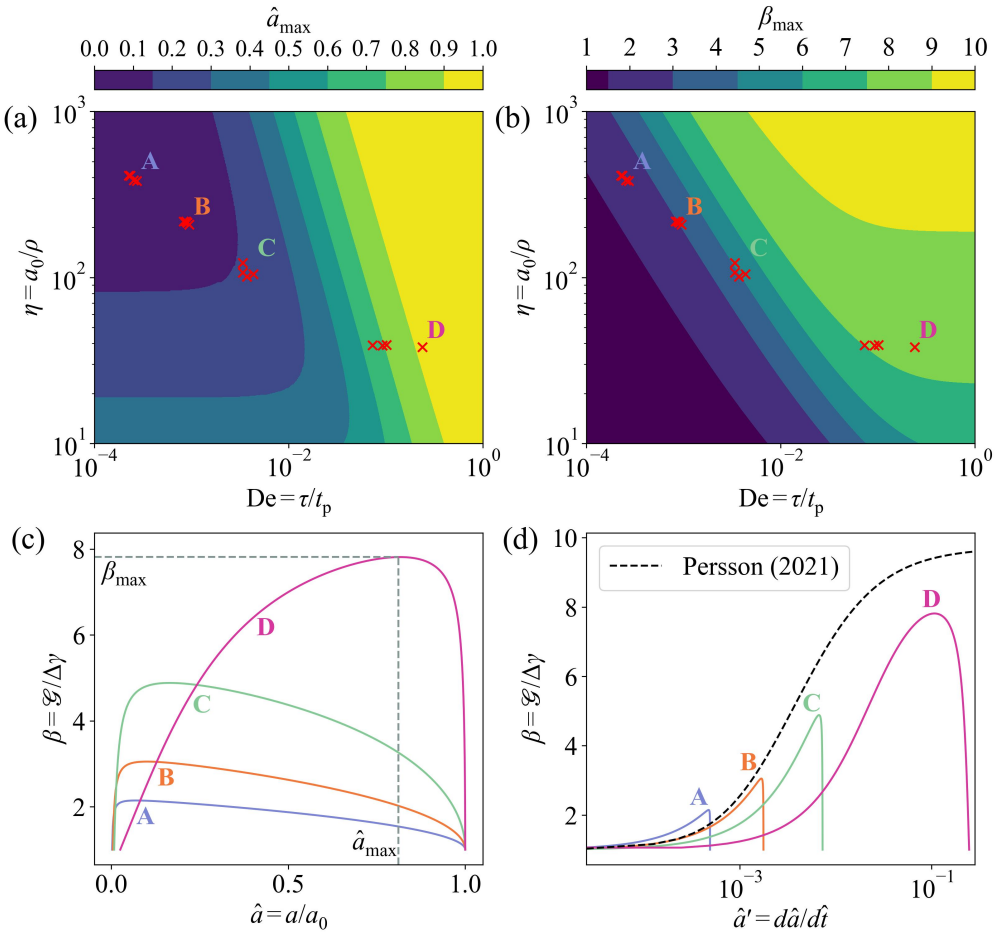

Figure 3.3: Contour plots of $\hat{a}_{max}$ (a) and β_{max} (b) as a function of both $\eta = a_0/\rho$ and $De = \tau/t_p$. Experimental results for gelatin from Ref. (Lee and Eriten, 2024) are projected to the contour plot as markers. Markers A to D corresponds to the unloading rates in order from $V_u = 0.01$ mm/s to $V_u = 10$ mm/s. The evolution of $\beta = \mathcal{G}/\Delta\gamma$ as a function of the normalized contact radius $\hat{a} = a/a_0$ (a) and the normalized crack velocity $\hat{a}' = d\hat{a}/d\hat{t}$ for A to D. The normalized energy release rate β as a function of $\hat{a}$ (c) and $\hat{a}'$ (d) for markers A to D.

through relative peeling times $\{72, 7.6, 0.85, 0.14\}$ s observed in the experiments and effective elasto-adhesive lengths $\bar{\mathcal{G}}/E$, where $\bar{\mathcal{G}}\pi a_0^2 = \int F d\delta$

for $F \leq 0$ in Fig. 3.2(c). Note that De is inversely proportional to the peeling times and the elasto-adhesive lengths represents an upper bound estimate for ρ. So, the placement of experimental markers on Fig. 3.3(a-b) should be taken as a crude approximation. The peeling durations from the experiments and the estimated De values result in the relaxation time constants $\tau < 0.02$ s that agree with the ranges reported in the literature. For instance, Yengul et al.(Yengul et al., 2019) employed shear wave elastography and torsional vibration rheometry to explore the rheological behavior of tissue-mimicking gelatin over wide range of frequency (1-1000 Hz) and fitted the response to the SLS model. The estimated relaxation time constant τ ranges from 0.001 to 0.002 s. In another example, Normand and Ravey(Normand and Ravey, 1997) conducted creep measurements on gelatin and reported two relaxation time scales: one at around 0.02 s and the other at 1000 s. The former is believed to be associated with relaxation at the network scale, which can be interpreted as the viscoelastic time constant relevant to the peeling experiments.

Figs. 3.3(c) and (d) show the evolutions of β as a function of normalized contact radius $\hat{a}$ and crack velocities $\hat{a}'$, corresponding to a representative marker to each A through D in Fig. 3.3(b). Both evolutions capture qualitatively the experimental observations presented in Fig. 3.2(e) and (f), with maximum mismatch for $V_u = 1$ mm/s case, marker C. This discrepancy is attributed to the assumption of linear elasticity in the calculation of $\mathcal{G}$, whereas the actual material is poro-viscoelastic and exhibits

multiple relaxation time constants. As a result, time-dependent effects become more pronounced at higher unloading rates, leading to deviations from the model prediction. In Fig. 3.3(d), the dashed line represents the S-curve behavior applicable to half-space geometry (no finite-size effect) (Persson, 2021). In drawing that line, we employed the SLS model and parameters consistent with the values used for markers A to D ($k = 0.1$, $\tau = 0.003$ s, $a_0 = 2.95$ mm, and $\rho = 7.4$ ¯m). Note the striking differences between the transient β and S-curve behavior especially at the end of peeling process when crack velocities are high and $\hat{a} \to 0$. This is due to the finite-size effect where β undergoes small changes for most of the peeling process except for right before the full separation when it suddenly drops to 1. The start of peeling where crack tip accelerates significantly also exhibits minor deviations from the S-curve behavior. The maximum β values reached, however, follow the S-curve trend with crack tip velocities. In summary, the simple model allowed for qualitatively description of the transients that we observed in the energy release rate during probe-tack experiments. When the finite-size effect is present in similar practical contact cases, enhancement of adhesion cannot be defined constitutively (e.g., by the Gent-Schultz law (Gent and Schultz, 1972)), but rather would depend on peeling kinematics and contact geometry.

Assumptions and limitations

It is worth revisiting the assumptions and limitations of the preceding analysis and model. First, viscoelastic relaxation degree, time constant(or spectrum), and crack tip radii were not observed directly, but rather were set crudely to match some auxiliary information gathered from the experiments. For instance, we set $k = 0.1$ considering the maximum enhancement of work of adhesion that we reported at 10 mm/s unloading rates in an earlier work (Lee and Eriten, 2024). However, there could be more enhancement at unloading rates higher than 10 mm/s. In addition, we assume that the crack tip radius ρ scales with the elasto-adhesive length scale $\bar{\mathcal{G}}/E$. However, the crack tip radius should also exhibit transients, as instantaneous release rate and modulus are expected to vary during peeling. We employ SLS model to represent viscoelastic response around the crack tip. For most of the viscoelastic materials, however, it is well-known that multiple (at least ten) relaxation time scales are needed for accurate modeling of viscoelastic response(Knauss, 2015). Recent work done by Maghami et al.(Maghami et al., 2024) shows sensitivity of rate-dependent adhesion to broadband nature of relaxations. Transients that we report here are also expected to be sensitive to relaxation time scales.

Relating the energy release rate $\mathcal{G}$ to the external work rate estimated from the experiments is only justified for De $\ll 1$, where the peeling process is sufficiently slower than viscoelastic time scales and thus the

viscoelastic dissipation in the bulk can be neglected. This assumption fails for fast unloading (crack velocity) cases, where De $\gtrsim$1, and so bulk dissipation is significant. To recover the transients for that regime, numerical methods can be used to obtain relative contribution of bulk dissipation to the instantaneous release rate $\mathcal{G}$. Additionally, full separation in the experiments takes place instantly (snap-off) at finite contact radii $\hat{a} \approx 0.2$ as shown in Fig. 3.2. Since snap-off instabilities aren't modeled in the thought model, the parts of the transients shown in Fig.3.3c right before the end of peeling couldn't be related to physical observations. Lastly, in the current study, we assume that the rate-dependent adhesion is solely due to crack-tip viscoelasticity. However, diffusion of water with the gel network; i.e., poroelasticity can also trigger dissipative response, alter energy release rates to the contact edge, and thus lead to rate-dependent changes in adhesion. For a given contact radius in our experiments, the poroelastic relaxation time scales $\tau_{\mathrm{PE}} \sim 100$ s, which is comparable to the duration of unloading only at the slowest unloading rate $V_u = 0.01$ mm/s (≈ 70 s) (Lee and Eriten, 2024). Much smaller time scales will also play role when diffusion is confined to mesh or crack tip radius length scales as shown in Refs(Baumberger et al., 2006b; Michel et al., 2019). Physics-based modeling of those local and global mechanisms require resolution of broad spatiotemporal scales. An attempt is given in Ref (Shen and Vernerey, 2020), where de/bonding dynamics in a transient gel network is tied to rate-dependent fracture response of a macroscopic pure-shear

sample. Similar studies are needed to fully reveal the links between local transients and the global ones that we observed in adhesion of gelatin.

3.4 Conclusion

In this work, we reported the transient, rate-dependent adhesion behavior observed during the monotonic unloading of a spherical probe from gelatin. In particular, we presented the instantaneous external work required for peeling and the evolution of contact edge (crack) velocities, experimentally captured from the initiation of propagation to full separation. As peeling progressed, crack velocities increased monotonically, partially following the nonlinear kinematic relation between crack and probe motions, but with significant deviations near the onset of propagation and close to full separation. In contrast, the instantaneous external work rate evolved non-monotonically: it initially increased from the thermodynamic limit to a peak enhancement value, then decreased again toward the thermodynamic work of adhesion as separation neared completion. To explain these trends, we incorporated finite-size effects into de Gennes' viscoelastic crack propagation model, assumed a simple time evolution for the contact radius, and computed the evolution of the instantaneous enhancement of work of adhesion, β, as a function of the nondimensional parameters De and η. Here, De characterizes the ratio of the viscoelastic relaxation time to the total peeling duration, while η represents the ratio

of the initial contact radius to the crack tip radius. A parametric study of the transients in β was conducted and compared against experimental trends in the instantaneous external work rate. The simulated evolution of β qualitatively matched the experimentally observed trends in external work rate with respect to contact radius and crack velocity, highlighting the importance of initiation and finite-size effects in the energetics of adhesive peeling in gelatin. While several prior studies (e.g., Refs(Mandriota et al., 2024; Saulnier et al., 2004)) have addressed rate- and size-dependent effects in soft adhesion, they typically focus on steady-state or quasi-static peeling scenarios. In contrast, our work captures the full transient dynamics of a single peeling event, where energetics/crack-driving forces evolve non-monotonically due to a combination of nonlinear kinematics and rapidly varying crack-driving forces. We observe that rate-dependent responses near the crack tip and finite-volume effects are triggered at different stages of peeling, leading to distinct energetic regimes. Notably, the instantaneous relationships between crack speed and energy release rate (ERR) deviate significantly from those predicted by steady-state models. The transitions, including short- to long-range adhesion shifts near the crack tip, underscore the limitations of existing models in capturing the full complexity of unsteady peeling. By revisiting earlier models considering these observations, we aim not only to contextualize our findings but also to emphasize the need for new frameworks that can accommodate the rich transient behavior observed in soft adhesive systems. Lastly,

we outlined the limitations and assumptions of our model and proposed future directions for establishing stronger correlations among various rate-dependent mechanisms and transient adhesion behaviors. Once fully understood, these mechanisms may be harnessed to tune the apparent adhesive properties of soft multiphasic materials, even under dynamic loading conditions.

4 CHAPTER 4. RATE-DEPENDENT FRICTION DURING PRE-SLIDING IN GELATIN*

(*This work is documented for the submission to an academic journal.)

4.1 Introduction

How does sliding in gels initiate and progress under shear? What mechanisms govern static and sliding friction in gels? The answers of these questions are critical in reliable operation of numerous applications including biomedical devices (Zhang et al., 2022), soft robotics (Asawalertsak et al., 2023), tissue engineering (Han et al., 2019), and food processing (Corvera-Paredes et al., 2022). Gels, as soft, multiphasic materials composed of polymer networks swollen with solvent, exhibit unique interfacial behaviors when in contact with solid substrates such as glass. At the interface, polymer chains can form transient bonds through hydrogen bonding or van der Waals interactions, contributing to the complexity of their frictional response. The frictional response of gels depends on shear rate, normal pressure, and loading history, and thus is highly nonlinear and challenging to understand and formulate (Yamamoto et al., 2014; Yaqoob et al., 2013; Reale and Dunn, 2017; Han and Eriten, 2018a; Gong, 2006; Baumberger et al., 2002).

Prior studies on gel friction have focused on the full sliding regime,

where the entire contact interface undergoes relative motion. In this regime, gel friction typically exhibits a non-monotonic dependence on sliding velocity —initially strengthening, then weakening, and strengthening again at higher speeds. This behavior is well captured by the repulsion–adsorption model proposed by Gong et al. (Gong, 2006), where polymer chains with polar groups (e.g., $-$OH, $-NH_2$, $-$COOH) form transient bonds with the opposing surface via hydrogen bonding or van der Waals interactions. These bonds form and rupture on microsecond timescales, and under shear, the chains stretch and detach, modulating friction in a manner reminiscent of Schallamach's rubber friction model (Schallamach, 1963). At higher velocities, solvent migration under stress alters interfacial hydration, leading to transitions between lubricated and dry friction regimes. Shoaib et al. (Shoaib and Espinosa-Marzal, 2018) identified two distinct lubrication regimes in polyacrylamide hydrogels, marked by non-monotonic friction–velocity relationships and stick–slip behavior. Their work highlights the role of polymer dynamics, mesh size, and interfacial interactions in governing transitions between adsorption- and viscous-dominated friction. Surface properties also play a critical role. Meier et al. (Meier et al., 2019) showed that hydrogels synthesized in hydrophobic molds develop brushier, and more hydrated surfaces with lower velocity-independent friction.

Beyond the molecular scale, continuum models address friction through bulk material responses and surface interactions. Persson and colleagues

(Persson, 1998; Persson and Tosatti, 2013) proposed a model that incorporates both viscoelastic bulk hysteresis and surface adhesion. Although originally developed for rubber friction, this framework offers valuable insights into the mechanisms governing gel friction at macroscopic scales. While the studies mentioned above have primarily focused on viscoelastic dissipation in the polymer network, other research has emphasized the role of poroelasticity—particularly the coupling between fluid flow and network deformation—in shaping the frictional behavior of gels. Reale and Dunn (Reale and Dunn, 2017) demonstrated that water exudation under load modulates adhesion and friction through poroelastic relaxation. Similarly, Delavoipière et al. (Delavoipière et al., 2018) showed that friction in thin hydrogel films is governed by poroelastic drainage, with transitions between regimes controlled by the Péclet number. Their model reveals that pore pressure unbalance generates lift forces, altering contact geometry and dissipating energy primarily through fluid flow at the contact edges.

While extensive research has focused on the sliding regime of gel friction, the pre-sliding regime has received comparatively limited attention. However, the pre-sliding regime is critical because it often involves the highest tangential stresses, which can precipitate material or structural failure. Moreover, it governs the onset of motion, energy dissipation, and interfacial stability. Our previous study (Han and Eriten, 2018a) investigated the role of poroelastic relaxation-dependent adhesion in the

pre-sliding response of cartilage, employing a slip-based failure model inspired by Savkoor (Savkoor, 1992) and Brochard-Wyart & de Gennes (Brochard-Wyart and de Gennes, 2007). The study demonstrated a linear correlation between resistance to slip-based failure and the work of adhesion. The cartilage and hydrogel share similarities in their structure and mechanical behavior, and the findings in pre-slididng response of cartilage can offer the deeper insights into the frictional mechanisms governing pre-sliding in hydrogels. However, it lacked direct experimental evidence of peeling and/or slippage at the interface. *In-situ* contact imaging could provide valuable insights into the stick-slip transition, evolution of contact area, and the extent of partial slip during the pre-sliding phase. Additionally, the study did not address rate-dependence, a key factor in the behavior of poro-viscoelastic materials like cartilage and hydrogel. To the best of our knowledge, the pre-sliding frictional response of gelatin, particularly its rate-dependence and slip characteristics remains unexplored in the literature.

In this study, we investigate the rate-dependent frictional behavior of gelatin in the pre-sliding regime using a custom-built friction tester with *in-situ* contact imaging. By tracking the motion of surface defects (treated as tracers) within the contact area, we quantify the evolution of local displacement, slip, and contact area under varying driving velocities. We compare experimental observations with theoretical predictions from the Cattaneo-Mindlin model (Cattaneo, 1996; Mindlin, 1949) to assess the

applicability of classical friction models to soft gel systems. Our findings reveal that the energy dissipation in the pre-sliding regime is primarily governed by partial slip rather than peeling by quantifying the extent of partial slip and peeling and estimating the associated energy losses. These results underscore the need for a new framework that integrates interfacial dynamics (slippage) and fracture process (peeling), offering a more comprehensive understanding of gel friction across regimes. This paper is organized as follows: Section 4.2 describes the sample preparation, experimental setup, and image-based analysis methods. Section 4.3 presents the measured friction forces, local displacement fields, partial slip behavior, and contact area evolution. We identify three distinct regimes of shear-induced contact evolution and discuss their implications. Finally, Section 4.4 summarizes the key findings and highlights the broader significance of understanding pre-sliding friction in soft gels.

4.2 Methods and Analyses

Sample preparation

Gelatin powder (G2500 Type A, Sigma Aldrich, Inc.), derived from porcine skin, is used to prepare a 10% w/v gelatin solution. The powder is mixed with deionized water and heated to $60^{\circ}C$ while stirring at 150 rpm using a magnetic stirrer for 30 minutes, ensuring a homogeneous solution. After

heating, the solution is cooled to $45^{\circ}C$, then degassed using a vacuum pump at 20 kPa until all air bubbles are removed. The degassed solution is poured into a hemispherical silicone mold with a radius of 18 mm. The exposed surface is covered with a flat, optically smooth glass plate (Glass A). The mold is placed in a refrigerator at $5^{\circ}C$ for 2 hours to allow the gelatin to set. Upon removal, the gelatin sample is carefully peeled from the mold. Due to the hydrophobic nature of the silicone mold and the hydrophilic nature of the glass, detachment occurs preferentially at the gelatin–silicone interface. To prevent dehydration, the sample is enclosed in a plastic container with a wet sponge and allowed to equilibrate at room temperature ($23^{\circ}C$) for 24 hours.

Friction tests

For friction tests, we develop a custom-made tester with an *in-situ* contact imaging as shown in Fig. 4.1(a). The gelatin hemispheres are fixed onto a substrate coated with black paint to enhance visualization of the contact area. A flat, optically smooth glass plate (Glass B) is mounted on Slider A, and thus is free to move in the z-direction. This configuration allows Glass B to apply a normal load on the gelatin solely through its dead weight. The combined weight of Slider A and Glass B generates a normal force of $F_n = 1.44$ N. Slider A is engaged with Slider B, which permits free movement in the x-direction, enabling Glass B to shear over the gelatin surface. Both sliders (LSP1390, MISUMI) are precision ball sliders with an

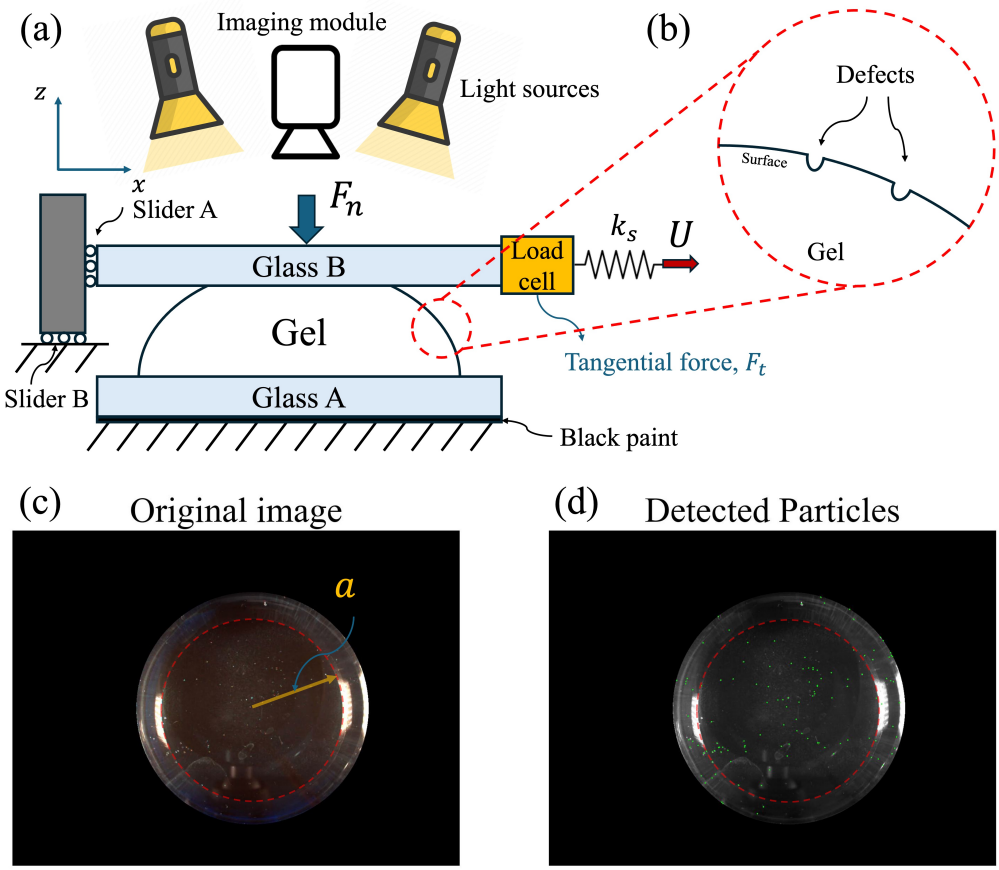

Figure 4.1: (a) The sketch of the experimental setup for friction tests and the zoom-in surface of the gels with small defects. The defect size is around 10-20 μm, while the radius of gel R is 18 mm, and the initial contact radius a_0 is around 14 mm. The sketch is not to scale. (c) The real image of the gel and its contact area with small dots (particles) where the light is scatters at the defects, and (d) the detected particles with green dots through the particle detection algorithm.

extremely low friction coefficient. Independent air tests (without contact with the gelatin) reveal a friction coefficient of approximately $\mu \approx 0.01$ for driving velocities U ranging from 0.01 mm/s to 10 mm/s. This value is

significantly lower than the friction coefficients observed during gelatin contact tests, which range from 0.25 to 1 depending on U. A load cell (LSB201, 8.9 N capacity, FUTEK Inc., resolution 18 mN) is mounted at the tip of Glass B to measure the tangential force F_t in the x-direction. The load cell has a stiffness of 88 kN/m, which is orders of magnitude greater than the estimated contact stiffness $k_c \approx 167$ N/m. This ensures that most deformation occurs at the gelatin–glass interface rather than within the load cell. Tangential force data is collected at 400 Hz. A linear actuator (VT-75, Physik Instrumente, 2 μm resolution) is connected to the load cell via a steel wire with a diameter of 3.2 mm. The stiffness of the steel wire is approximately $K_s \approx 4$ MN/m, leading to negligible wire extension during transmission of motion from the actuator to the loading plate (Glass B). The actuator pulls the wire in the x-direction at various driving velocities U (0.01 mm/s to 10 mm/s) to investigate the rate-dependent frictional behavior of the gelatin until a fully sliding regime is reached. The actuator accelerates at approximately 300 mm/s^2, reaching 10 mm/s in about 0.03 s, which is significantly shorter than the loading duration at $U = 10$ mm/s (approximately 1.6 s). This ensures that pre-sliding response is obtained at constant shear rates. At higher velocities ($U \gtrsim 10$ mm/s), material failure is observed near the trailing edge of the contact area. According to Hamilton (Hamilton, 1983), for frictional contact under constant normal load in elastic materials, the maximum tensile stress occurs at the trailing edge and is estimated as $\approx F_{t,s}/a^2 \approx 7$ kPa, where $F_{t,s}$ and a are the static

friction force and the contact radius, respectively for $U = 10$ mm/s. This value is comparable to the tensile strength of gelatin-based hydrogels (Yousefi-Mashouf et al., 2023). Due to the large contact radius a, slow poroelastic diffusion, and minimal viscoelasticity in gelatin (Yengul et al., 2019; Baumberger et al., 2002), the creep in the z-direction is negligible during the test duration. This enables that the pulling direction remains nearly horizontal throughout the tests and the normal load F_n is constant throughout the experiments.

Contact area, local displacement and slip measurements

An imaging module (U3-3040CP-C-HQ, IDS Imaging Development Systems) and LED light sources are positioned above Glass B to observe changes in contact shape and slip during tangential loading. The imaging system provides a spatial resolution of 40 μm/pixel. The temporal resolution is selected based on the driving velocity U and the loading durations: 5, 30, 60, and 70 fps are used for $U = 0.01$, 0.1, 1, and 10 mm/s, respectively. Light from the LED sources passes through the contact area and is absorbed by the black paint beneath Glass A, rendering the contact region dark in the captured images. In contrast, light is scattered or reflected in non-contact regions, allowing clear visualization of the contact boundary and its evolution during loading. The gelatin surface contains numerous small defects, such as dimples, with sizes ranging from 10–20 μm (see Appendix B for microscopic images of the gel and mold surfaces). The gelatin

is optically transparent and no internal bubbles are observed. Given that the defects are much smaller than the penetration depth of the gel (a few millimeters) and the gelatin is soft, their influence on frictional and contact behavior can be neglected (the ratio of defect size to the penetration depth $\lesssim 0.01$) (Greenwood and Tripp, 1967). These defects scatter and reflect light, appearing as small bright dots in the images. Due to the light diffraction and scattering, the size of bright dots in the image is usually larger than the real size of the defects ranging from around 100 μm to 300 μm, which are larger than the spatial resolution of the imaging module.

These dots are used to track displacements and slip across the contact area during shearing. In this study, we refer to these features as *particles*, although they are not physical particles but rather visual artifacts resembling particles in the images. We employ particle detection and tracking algorithms to monitor the displacement of particles at each frame. Each frame is processed to isolate bright particles using intensity thresholding and contour detection to find the particle's shape and compute the center positions. The particle position from the previous frame are matched to current frame using a spatial tree structure (cKDTree from SciPy), which efficiently finds the closest particle within a defined maximum displacement for frame-by-frame particle tracking. The maximum displacement is chosen considering the motion of glass and the frame per second. Fig. 4.1(c) shows a typical image from the imaging module, where the red dashed line indicates the contact edge, and the contact radius a is defined

accordingly. Figure 4.1(d) displays the detected particles after applying the detection algorithm. Detected particles fall into four categories: particles within the contact area; particles outside the contact area; particles on Glass A; particles on Glass B. Only particles within the contact area are used for displacement analysis. After detection, we manually verify and filter out particles outside the contact area or those that escape the contact region during shearing. We thoroughly examined each particle's position in both the initial and final frames of the pre-sliding phase. Particles that are found outside the defined contact area in either frame are excluded from further analysis. Particles that remain stationary (e.g., fixed on Glass A) are also excluded. Particles that move identically to the linear actuator (i.e., without slip) are used to define the glass displacement vector, denoted as $\mathbf{G}$. These particles may be originated from the defects of Glass A and B. Particles lost during tracking are discarded. The remaining particles are used to compute the local displacement vector δ_i for each particle i within the contact area. The number of trackable particles ranges from 30 to 40. Fig. 4.2 illustrates the particle motion and the methodology for extracting local slip behavior. The displacement vector of particle i, $\delta_i(t)$ and the glass motion $\delta_G(t)$ are shown in Fig. 4.2. We then define the cumulative local slip vector of particle i, as $\mathbf{\Delta S}_i(t) \equiv \delta_G(t) - \delta_i(t)$. To quantify the relative motion between a spherical gel and a flat glass, it is essential to understand the local slip behavior at the contact level. The Cattaneo-Mindlin (CM) model provides the fundamental framework for

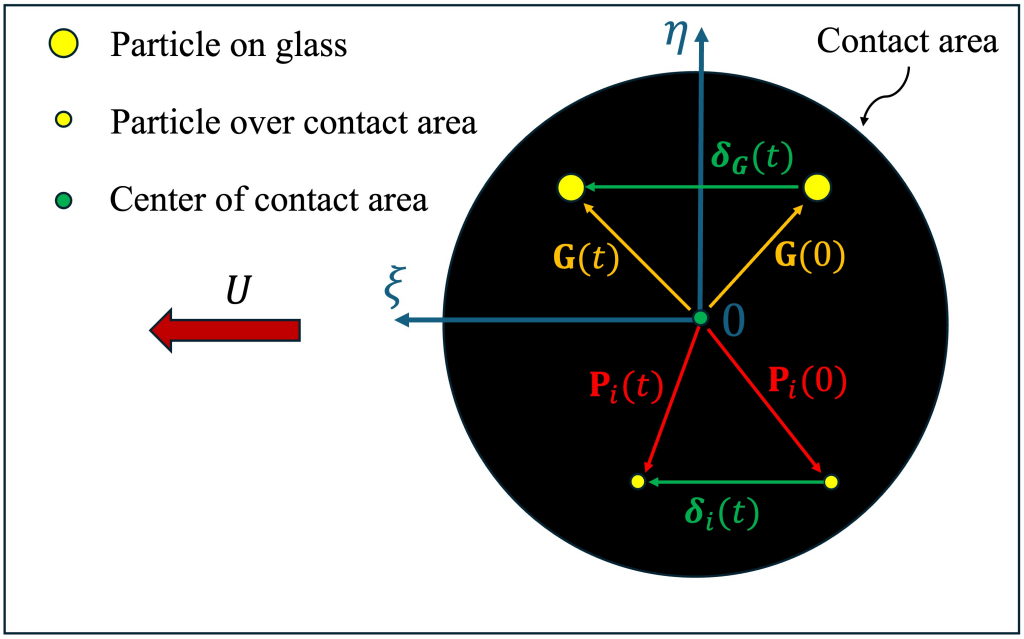

Figure 4.2: The sketch of the particle motion vectors $\mathbf{P}_i$ and glass motion $\mathbf{G}$, and the displacement vector of the particles and the glass motion.

describing the elastic contact and the microslip. According to CM model, the slip amount in ξ and η directions in Fig. 4.2 are given by

$$\Delta S_\xi \approx \frac{3\mu F_n}{16Ga}(2-\nu)\left[\left(1-\frac{2}{\pi}\sin^{-1}\frac{c}{r}\right)\left(1-2\frac{c^2}{r^2}\right)+\frac{2}{\pi}\frac{c}{r}\left(1-\frac{c^2}{r^2}\right)^{0.5}\right] \tag{4.1}$$

$$\Delta S_\eta \approx 0 \tag{4.2}$$

, where c is the sticking area computed as $c = a\left(1 - F_t/\mu F_n\right)^{1/3}$. Here, μ is the friction coefficient where the tangential traction $q(\xi,\eta)$ cannot exceed $\mu p(x,y)$ in the sticking region (Johnson, 1987). Note that the equation is

valid only over $c \leq r \leq a$. The friction coefficient μ in our case is assumed to be the driving velocity dependent $\mu = \mu(U)$.

4.3 Results and Discussions

Friction force

Fig. 4.3(a-d) shows the evolution of tangential force at driving velocities $U = [0.01 - 10]$ mm/s. The Savitzky-Golay filter is used to get smoother signal of F_t with a polynomial of degree 3. The window length was selected based on the duration of the tests, corresponding to 7001, 3001, 201, and 51 data points for velocities $U = 0.01$, 0.1, 1, and 10 mm/s, respectively. The normal load $F_n = 1.44$ N, and the mean normal contact pressure $F_n/(a^2\pi)$ is around 2.3 kPa. As the linear actuator drives the glass motion in x-direction, the tangential force builds up from 0 to certain static friction force $F_{t,s}$. $F_{t,s}$ increases by around 3.5 folds by changing driving velocity from 0.01 mm/s to 10 mm/s. This increase in static friction force by the loading rate is similar to the increase in pull-off force by increasing unloading rate from 0.01 to 10 mm/s in our previous study for gelatin (~ 5 folds increase) (Lee and Eriten, 2024). The difference between 5 folds and 3.5 folds increase may come from the different mode of fracture, the sample size, the boundary effect, and the partial slip in pre-sliding. After reaching $F_{t,s}$, the slowest driving velocity $U = 0.01$ mm/s exhibits stick-slip oscilla-

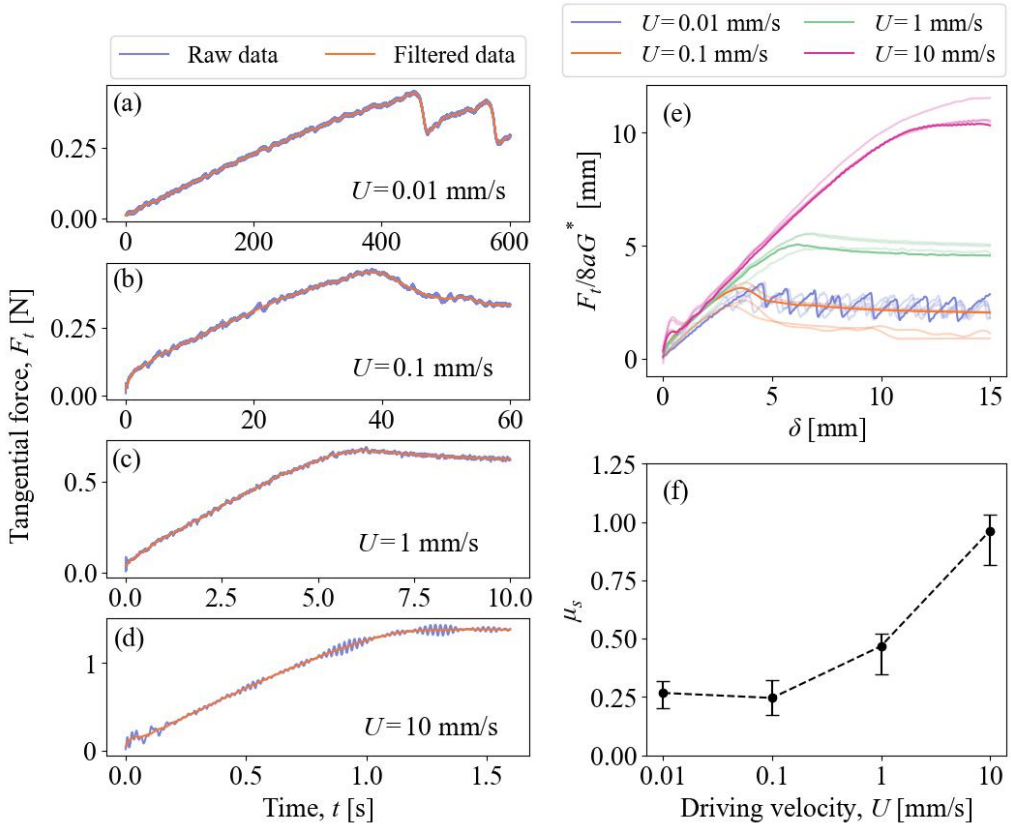

Figure 4.3: (a-d) The tangential force over time for the driving velocities $U = [0.01 - 10]$ mm/s with (orange) and without (blue) filtering. (e) Estimated relative displacement without slippage $F_t/8aG^*$ by Mindlin (Mindlin, 1949) vs. displacement of glass δ for the driving velocities $U = [0.01 - 10]$ mm/s. (f) The averaged static friction coefficient $\mu_s \equiv F_{t,s}/F_n$ as a function of U. The error bar shows the range of the maximum and minimum values for 4 repetitions.

tion: slip occurs, the tangential force drops as the gel deformation recovers, the surface re-sticks, force re-builds up and it repeats these slip-stick behavior. For higher $U \geq 0.1$ mm/s, this stick-slip oscillation disappears,

and we have full sliding after $F_{t,s}$. In the fully sliding regime, the kinetic friction is lower than $F_{t,s}$ except for $U = 10$ mm/s, where the kinetic friction is comparable to $F_{t,s}$. Fig. 4.3(e) shows the relative displacement without slippage $F_t/8aG^*$ predicted by CM model over the displacement of glass. The filtered data are used in the figure. The displacement of the glass is simply computed by multiplying time by the driving velocity. The figure includes all four repetitions for all driving velocity cases and shows good repeatability. The slopes of Fig.4.3(e) especially in the initial regime of loading are close to 1 across all cases. This indicates that the CM model performs well in the presliding regime. According to CM model for linear elastic frictional contact, the contact stiffness is given as $k_c = 8aG/(2-\nu)$, where ν is the Poisson's ratio (Johnson, 1987), assuming the glass in contact is rigid compared to the gel. By this equation, the shear modulus is given as around 2.2 kPa. This value is close to the modulus found in other works for similar gelatin (Lee and Eriten, 2024; Baumberger et al., 2002) in magnitude. The displacement necessary to acquire fully sliding regime (d_s) is driving-velocity-dependent. For $U = 0.01$ mm/s and 0.1 mm/s, around 4-5 mm of displacement is needed to have full sliding, while around 6 mm of displacement is necessary for full sliding at $U = 1$ mm/s. Especially for highest driving velocity $U = 10$ mm/s, it is required to have around 12 mm of displacement, which is similar to the initial contact radius $a \approx 14$ mm. The area under the curve prior to full sliding represents the mechanical energy input into the system. A portion

of this energy is stored in the gel as strain energy, while the remainder is dissipated. Energy dissipation may arise from frictional losses due to microslip, as well as from bulk viscoelastic or poroelastic relaxation mechanisms. However, as shown in the force–displacement curve in Fig. 4.3(e), the bulk material response under shear exhibits limited rate dependence. This observation suggests that bulk viscoelasticity in the gel is minimal for a given driving velocity range, and that poroelastic diffusion is too slow to contribute significantly within the experimental timescale. For instance, diffusion across the contact region of radius $a \approx 14$ mm would require approximately $\tau_P \sim a^2/D \approx 2 \times 10^7$ s, assuming a diffusivity of $D \sim 10^{-11}$ m^2/s for a gelatin (Baumberger et al., 2002).

In Fig. 4.3(f), the static friction coefficient $\mu_s = F_{t,s}/F_n$ is shown as a function of the driving velocity U. The error bars represent the maximum and minimum values of μ_s obtained from four repetitions. From 0.01 mm/s to 0.1 mm/s, μ_s is almost unchanged. After that, μ_s increases with U. Similar velocity-strengthening in friction was observed in other types of gels, e.g., polyacrylamide (PAAm), polyacrylic acid (PAA), and agarose hydrogel (Shoaib et al., 2018; Cuccia et al., 2020; Gong, 2006; Kim and Dunn, 2020). The velocity dependence of friction coefficient was also observed by Baumberger et al. (Baumberger et al., 2002, 2003). They studied the flat gel-on-glass contact with different concentrations and driving velocities. In their experiments, stick-slip oscillation occurs $U < 125\,\mu m/s$ and disappears for $U \gtrsim 125\,\mu m/s$. The kinetic friction coefficient

μ they reported is around 0.59 at 1 mm/s sliding velocity with the normal stress 1.65 kPa (5 w/v%), while the kinetic friction coefficient μ in our experiments at the same velocity is 0.47. The difference might be due to the different gel concentration, normal stress, geometry, and boundary conditions.

According to the repulsion–adsorption model of gel friction in the attractive regime (Gong and Osada, 1998; Gong, 2006), there are two primary contributions to friction in gels: elastic stretching of adsorbed polymer chains (elastic friction) and lubrication by hydrated polymer chains (lubricated friction). Based on scaling arguments, a characteristic velocity that marks the transition between these two regimes is introduced as $v_f \sim R_f/\tau_f \sim k_BT/\eta R_f^2$, where R_f and τ_f are the blob size of the C^* gel and the characteristic lifetime of polymer chain adsorption, respectively (De Gennes, 1979; Gong and Osada, 1998). Here, k_B, T, and η denote the Boltzmann constant, absolute temperature, and solvent viscosity, respectively. For polymer gels, C^* gels is the critical polymer concentration needed to form a continuous network during gelation, and the blob is In gel friction, blob helps describe the how the polymer chains stretch and move when the gel slides against a surface. The blob size R_f gives a measure of how much of the chain is involved in this interaction. When $v/v_f \ll 1$, where v is the sliding velocity, polymer chains have sufficient time to adsorb onto the opposing surface, and elastic friction dominates. Conversely, when $v/v_f \gg 1$, lubricated friction becomes dominant. For

gelatin, using $k_B = 1.38 \times 10^{-23}$ J/K, $T = 296$ K, $\eta = 1$ mPa $\cdot$ s, and estimating $R_f \sim (k_B T/E)^{1/3} \approx 7$ nm, the characteristic velocity is calculated as $v_f \sim 80$ mm/s, which is significantly higher than the driving velocities $U = [0.01\text{–}10]$ mm/s. Note that blob size is comparable to the mesh size, and the experimental estimation by small-angle X-ray scattering for different types of gels range from a few nanometers to a few tens of nanometers depending on the chemical compositions, concentration, the solvent types, and temperature (Bode et al., 2013; Wisotzki et al., 2017). Moreover, the partial slip rate $|d\boldsymbol{\Delta S}/dt|$ remains below the driving velocity, confirming that the system operates within the elastic friction regime both locally and globally (the slip rate will be discussed in Section 4.3). In this regime, the frictional stress arising from the elastic stretching of adsorbed polymer chains can be modeled as $f_{\mathrm{el}} \sim mv\tau_b$, where m is the number of adsorbing sites per unit area (Schallamach, 1963). τ_b is the characteristic time it takes for a blob to respond to deformation. Here, m and τ_b are velocity-dependent (Gong and Osada, 1998), which introduces the nonlinear behavior in the frictional stress. This model qualitatively predicts that frictional stress increases with sliding velocity, which is consistent with the experimental observations shown in Fig. 4.3. According to the repulsion–adsorption model of gel friction in the attractive regime (Gong and Osada, 1998; Gong, 2006), there are two primary contributions to friction in gels: elastic stretching of adsorbed polymer chains (elastic friction) and lubrication by hydrated polymer chains (lubricated friction). Based on

scaling arguments, a characteristic velocity that marks the transition between these two regimes is introduced as $v_f \sim R_f/\tau_f \sim k_B T/\eta R_f^2$, where R_f and τ_f are the blob size of the C^* gel and the characteristic lifetime of polymer chain adsorption, respectively (De Gennes, 1979; Gong and Osada, 1998). Here, k_B, T, and η denote the Boltzmann constant, absolute temperature, and solvent viscosity, respectively. For polymer gels, C^* gels is the critical polymer concentration needed to form a continuous network during gelation, and the blob is used to describe the structure of chains constrained by the network. In gel friction, blob helps describe the how the polymer chains stretch and move when the gel slides against a surface. The blob size R_f gives a measure of how much of the chain is involved in this interaction. When $v/v_f \ll 1$, where v is the sliding velocity, polymer chains have sufficient time to adsorb onto the opposing surface, and elastic friction dominates. Conversely, when $v/v_f \gg 1$, lubricated friction becomes dominant. For gelatin, using $k_B = 1.38 \times 10^{-23}$ J/K, $T = 296$ K, $\eta = 1$ mPa $\cdot$ s, and estimating $R_f \sim (k_B T/E)^{1/3} \approx 7$ nm, the characteristic velocity is calculated as $v_f \sim 80$ mm/s, which is significantly higher than the driving velocities $U = [0.01\text{–}10]$ mm/s. Note that blob size is comparable to the mesh size, and the experimental estimation by small-angle X-ray scattering for different types of gels range from a few nanometers to a few tens of nanometers depending on the chemical compositions, concentration, the solvent types, and temperature (Bode et al., 2013; Wisotzki et al., 2017). Moreover, the partial slip rate $|d\boldsymbol{\Delta S}/dt|$ remains below the driving

velocity, confirming that the system operates within the elastic friction regime both locally and globally (the slip rate will be discussed in Section 4.3). In this regime, the frictional stress arising from the elastic stretching of adsorbed polymer chains can be modeled as $f_{\mathrm{el}} \sim mv\tau_b$, where m is the number of adsorbing sites per unit area (Schallamach, 1963). τ_b is the characteristic time it takes for a blob to respond to deformation. Here, m and τ_b are velocity-dependent (Gong and Osada, 1998), which introduces the nonlinear behavior in the frictional stress. This model qualitatively predicts that frictional stress increases with sliding velocity, which is consistent with the experimental observations shown in Fig. 4.3.

Displacement field over contact area

As shown in Fig. 4.2, we compute the displacement of the particles by $\boldsymbol{\delta}_i(t) = \mathbf{P}_i(t) - \mathbf{P}_i(0)$. Here, $\mathbf{P}_i(0)$ is the vector of particle i's position at t, and $\mathbf{P}_i(0)$ is its initial position vector at $t = 0$. Fig. 4.4(a-h) shows the components of the displacement vector of particles over the contact area in ξ and η directions δ_ξ and δ_η for $U = [0.01 - 10]$ mm/s. The black scatter dots in Fig. 4.4(a–h) represent the displacement of particles on the glass surface $\boldsymbol{\delta}_G(t) = \mathbf{G}(t) - \mathbf{G}(0)$, illustrating the motion of the glass itself. The slope of the δ_ξ versus time curves matches the driving velocity in all cases, while the slope of δ_η versus time remains close to zero. This indicates that the glass primarily moves in the ξ-direction (or x-direction), which aligns with the direction of the linear actuator. The particle motion

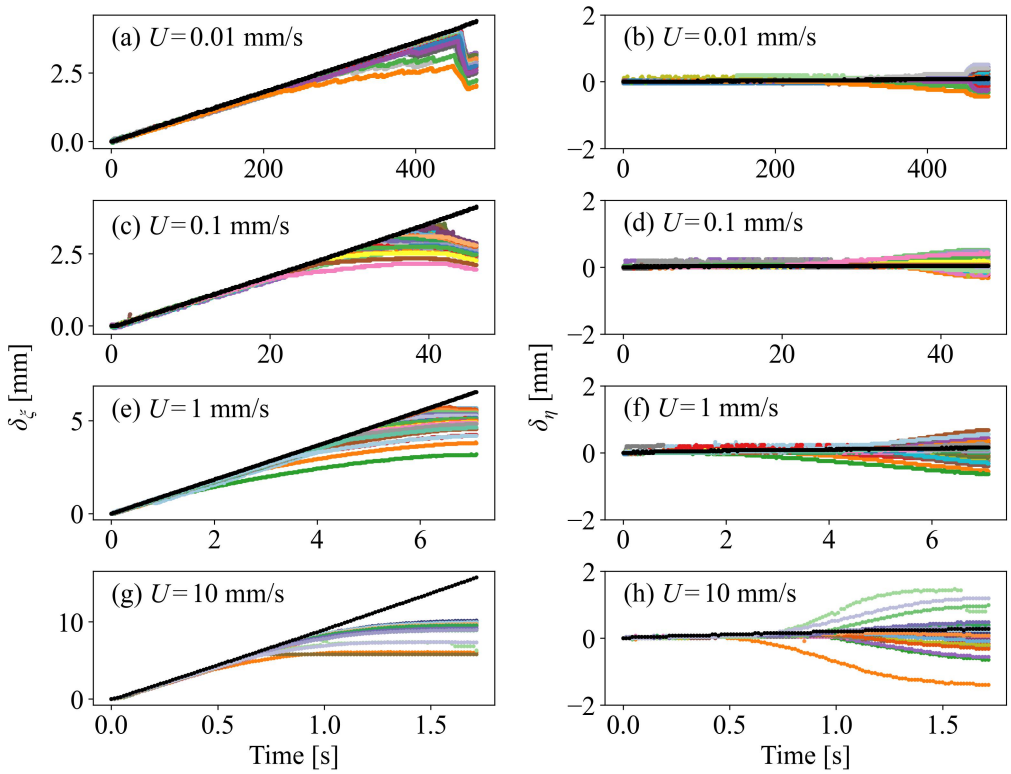

Figure 4.4: The components of the displacement vector of particles in ξ and η directions as a function of time for different driving velocities $U = 0.01, 0.1, 1$, and 10 mm/s. The black curves represent the rigid glass motion.

across the contact area also predominantly occurs in the ξ-direction, but it does not perfectly follow the glass motion. Instead, deviations from the glass trajectory are observed during the loading phase. These deviations begin at different times for different particles. For instance, in Fig. 4.4(a), the orange-colored particle begins to slip around 100 seconds, while others slip later. (The dependence of the particle location on the displacement in

ξ and η directions are discussed in Appendix B.2.) This staggered onset of deviation is evidence of partial slip occurring across the contact area. As slipping begins, particles also start to move in the η-direction. However, the displacement in the η-direction remains significantly smaller than that in the ξ-direction. The displacement in η-direction δ_η is highly dependent on the driving velocity. At $U = 0.01$, 0.1, and 1 mm/s, it is less than 1 mm, while some particles show relative large $\delta_\eta > 1$ mm at $U = 10$ mm/s.

Partial slip

As illustrated in Fig. 4.2, the local slip vector $\mathbf{\Delta S}_i$ is computed by subtracting the glass motion vector $\mathbf{G}$ from the motion vector of each particle $\mathbf{P}_i$. The magnitude of this slip vector, denoted as $|\mathbf{\Delta S}_i|$, quantifies the extent of local slip. Figure 4.5 presents the time evolution of the slip magnitude for individual particles under various driving velocities, ranging from $U = 0.01$ mm/s to 10 mm/s. In the initial stages of pre-sliding regime, there is no noticeable slip across the contact area for any of the tested cases. At later stages, the slip of individual particles commences at different times, highlighting the non-uniform onset of local slip. The slope of each curve represents the local slip rate. During pre-sliding, the maximum observed local slip rates are approximately 0.005, 0.05, 1, and 10 mm/s for driving velocities of $U = 0.01$, 0.1, 1, and 10 mm/s, respectively. In other words, local slip rates are bounded by the corresponding driving velocity. In summary, both the slip magnitude and slip rate vary from particle to

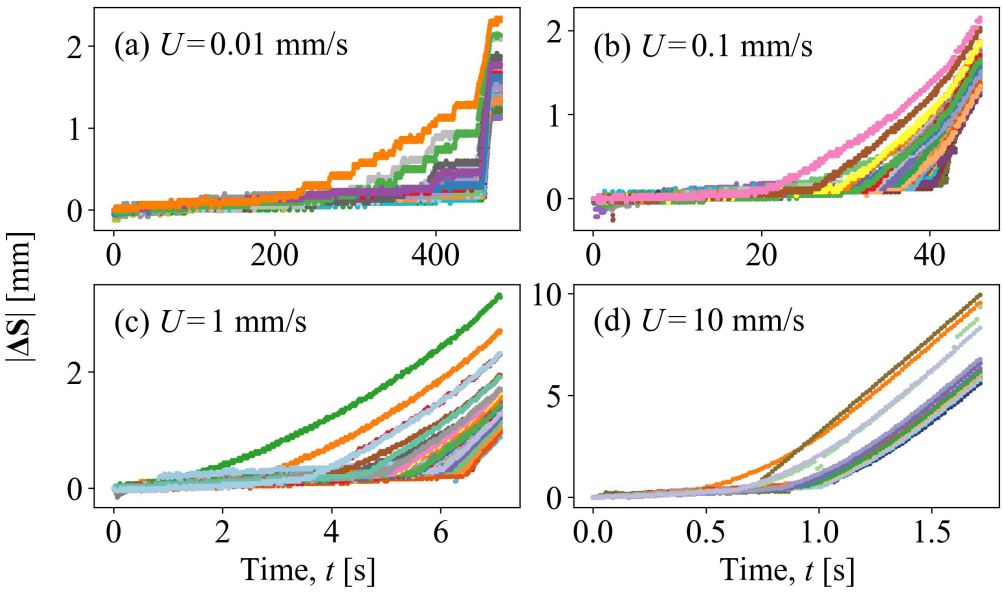

Figure 4.5: The magnitude of the slip vector as a function of time for different driving velocities $U = 0.01, 0.1, 1$ and $10\,\mathrm{mm/s}$.

particle, underscoring the heterogeneous nature of stick to slip transition across the gel interface. In Fig. 4.5(a), for $U = 0.01\,\mathrm{mm/s}$, the stick-slip oscillation is observed up to the second phase of sticking. Partial slip develops progressively until the system transitions into the fully sliding regime, at which point the slip amount increases abruptly. This abrupt change in slope at the onset of full sliding is evident across all particles. Following this transition, the system enters the second stick phase, during which the slope of the slip amount decreases. For $U = 0.1$ and $1\,\mathrm{mm/s}$, similar trends are observed in the transition from partial to full slip apart, as seen in the $U = 0.01\,\mathrm{mm/s}$ case. However, a few particles exhibit a

sharp change in slope, while most show smoother transitions. In contrast, the case of $U = 10\,\mathrm{mm/s}$ displays a distinct behavior. Most particles exhibit a significant amount of slip even before the onset of full sliding at approximately $t_s \approx 1.6\,\mathrm{s}$, which corresponds to the peak in F_t. This might imply that we have full sliding at around $t \approx 1\,\mathrm{s}$, as all particles over the contact surface begin to slip. However, to maintain consistency with standard frictional definitions, we define the onset of full sliding as the moment when the tangential force F_t reaches its maximum, rather than relying solely on slip estimation.

Fig. 4.6 illustrates the evolution of the local slip and contact area during built-up of tangential force at a driving velocity of $U = 0.01$ mm/s. For each time frame from (A) $t = 0$ to (E) $t = t_s$—where t_s marks the onset of full sliding— the magnitude of local slip for each particle is denoted by the color bar and the evolution of the contact area by the dashed circle. The time points (A) through (E) in Fig. 4.6 are equally spaced. During the pre-sliding regime at $U = 0.01$ mm/s, the contact area remains circular with a maximum reduction of about 4% at the onset of sliding (E). At the early stages loading; namely from (A) $t = 0$ to (B) $t = 0.25t_s$ most of the particles exhibit negligible slip, indicating that the majority of the contact area remains adhered to the glass. As the loading progresses toward the onset of full sliding, slip begins to accumulate near the contact edges. In frames (D) and (E), the slip magnitude $\boldsymbol{\Delta S}i$ increases significantly near the periphery, while particles near the center continue to exhibit minimal

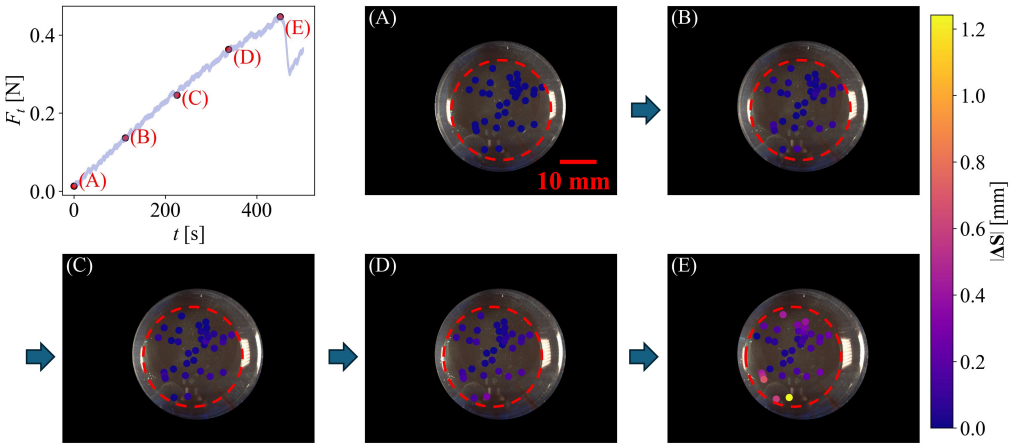

Figure 4.6: The evolution of frictional force F_t in the pre-sliding regime from (A) to (E) and its corresponding location and slip amount at $U = 0.01$ mm/s. (A) and (E) correspond to the onset of shearing and full sliding, respectively. The points (A) to (E) are equidistant.

slip. This behavior indicates that the sticking region initially coincides with the entire contact area a, but gradually shrinks as the tangential force F_t approaches the static friction threshold Ft, s.

Fig. 4.7 presents the evolution of the contact area and slip magnitudes at three key time points—$t = 0$, $t = 0.75t_s$, and $t = t_s$—for driving velocities of $U = 0.1$, 1, and 10 mm/s. At driving velocity of $U = 0.1$ mm/s, the change in contact area is minimal, with less than 4% reduction as in $U = 0.01$ mm/s case. At higher driving velocities—$U = 1$ mm/s and $U = 10$ mm/s—the contact area shrinks by approximately 7% relative to the initial contact area. As the driving velocity increases, the shape of the real contact area becomes increasingly elliptical, exhibiting anisotropy

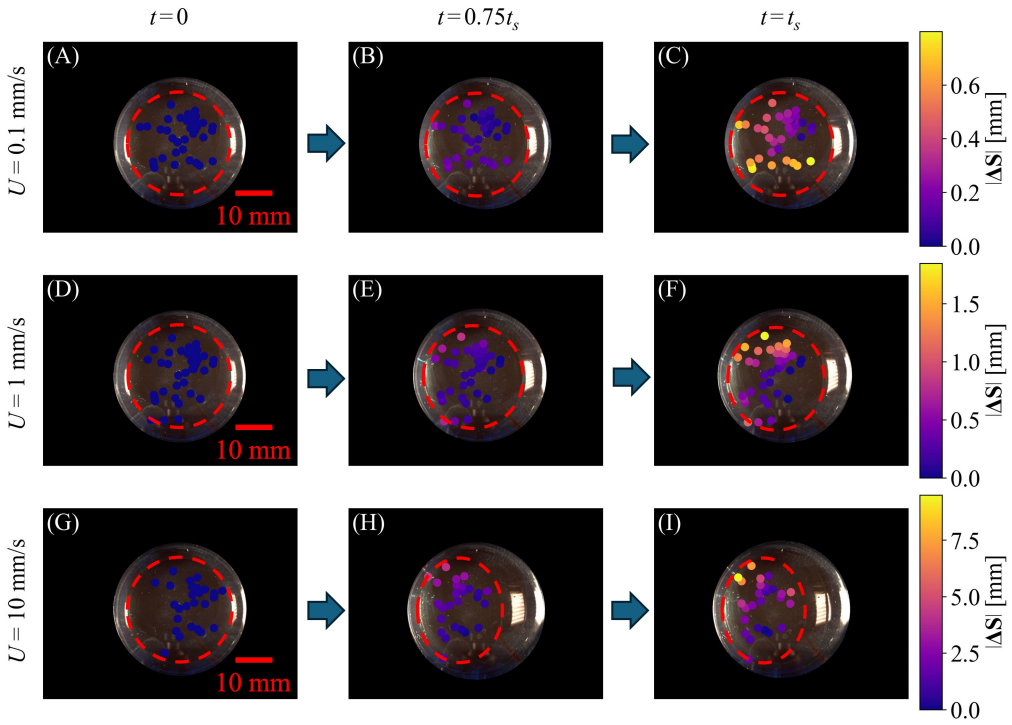

Figure 4.7: The evolution of contact area, particles' location and slip amount at (A-C) $U = 0.1$ mm/s, (D-F) $U = 1$ mm/s and (G-I) $U = 10$ mm/s. (A), (D), and (G) correspond to the onset of shearing at $t = 0$, respectively. (C), (F), and (I) correspond to the onset of full sliding at $t = t_s$. (B), (E), and (H) are at $t = 0.75t_s$.

in shrinkage. More shrinkage occurs along the loading direction (ξ), whereas the contact size in the η-direction remains nearly unchanged. This shear-induced reduction in contact area and corresponding anisotropy is also observed and studied in soft elastomeric contacts (Papangelo et al., 2019; Sahli et al., 2019; Lengiewicz et al., 2020; Misra and Huang, 2011; Delavoipière et al., 2018). For one of the plausible arguments for shear-

induced anisotropy in contact area, Papangelo et al. employed the Linear Elastic Fracture Mechanics (LEFM) to the mode-mixity frictional contact (mode I, II, and III) and showed the interfacial toughness of mode I + III (opening & out-of-plane shear) is higher than the toughness of mode I + II (opening & in-plane shear). This difference in interfacial toughness to the different mode of fracture results in contact area shrinks in in-plane fracture and anisotropic contact area during shearing.

This partial slip in frictional contacts is first modeled by Cattaneo-Mindlin (Cattaneo, 1996; Mindlin, 1949). To compare the average slip that we measured to the one predicted by that model, we compute average slip measured at t over the contact area as $\overline{|\mathbf{\Delta S}|}_e = 1/N \sum_i^N |\mathbf{\Delta S}|$, and the theoretical average slip amount as $\overline{\Delta S}_t = 1/(a-c) \int_c^a \Delta S_\xi dr$ from Eq. 4.2. As in Cattaneo-Mindlin theory, we assume that the contact radius remains the same during tangential loading. Fig. 4.8 shows the comparison between the experimental average slip amount and the theoretical slip amount. The black dashed line shows the line with a slope 1. Although the theoretical prediction of the slip amount captures the experimentally estimated value within one order of magnitude, the theoretical average slip, $\overline{\Delta S}_t$, is consistently higher than the experimental value, $\overline{|\mathbf{\Delta S}|}_e$. This discrepancy can be attributed to both experimental limitations and assumptions in the theory which are violated in the experiments (e.g., large deformation, contact area changes, presence of adhesion, and large a/R). First, regarding $\overline{|\mathbf{\Delta S}|}_e$, significant slip may occur near the periphery of the

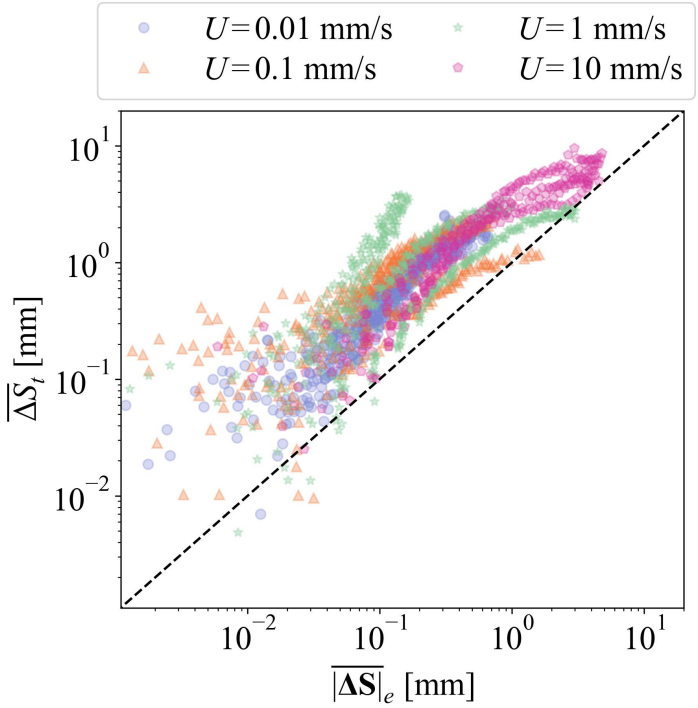

Figure 4.8: Comparison between the theoretical average slip amount $\overline{\Delta S_t}$, based on the Cattaneo-Mindlin theory (Mindlin, 1949; Cattaneo, 1996), and the experimentally estimated average slip amount $\overline{|\mathbf{\Delta S}_e|}$ for different driving velocities $U = [0.01 - 10]$ mm/s. The black dashed line represents the line of unity slope (slope = 1), and the red vertical dashed line indicates the spatial resolution limit of the imaging module.

contact. Particles located at the contact edge are often excluded from our analysis if they escape the contact region during pre-sliding. To ensure consistency in tracking, such particles are omitted. However, it is important to note that slip typically initiates at the contact edge and reaches its maximum there, which may lead to an underestimation of the total slip. Second, gel friction exhibits strong slip-rate dependence, as shown in

Fig. 4.3 in the fully sliding regime. The slip rate is not uniform across the contact area, as illustrated in Fig. 4.6 and Fig. 4.7. In fact, the local slip rate is generally smaller than or equal to the driving velocity U, which may also contribute to the discrepancy between theoretical and experimental slip values. According to the behavior in Fig. 4.3(f), the local friction coefficient μ may be smaller than or equal to the static friction coefficient μ_s. This slip rate dependent friction may overestimate the theoretical slip amount in Fig. 4.8. However, in our estimation for $\overline{\Delta S}_t$, we assume that the contact area is constant during pre-sliding, but it decreases by at most 20%. The change in a may lead to higher value of $\overline{\Delta S}_t$. In addition to this, the effects of geometric nonlinearity due to large deformations, as well as potential material nonlinearity of the gelatin, are not reflected in the theoretical analysis. Nevertheless, the qualitative comparison between $\overline{\Delta S}_t$ and $\overline{|\boldsymbol{\Delta S}|}_e$ shows that Cattaneo-Mindlin (Mindlin, 1949; Cattaneo, 1996) model captures well the partial slip behavior in gelatin.

Revisiting evolution of slip and contact area

Figure 4.9 illustrates three distinct regimes of shear-induced changes in contact area and slip magnitudes for $U = [0.01 - 10]$ mm/s: Regime A, early stage of tangential loading where nearly all particles are fully stuck and contact area remains constant; Regime B, increasing tangential loading that features partial slip and measurable reduction in contact area, and Regime C, where all particles slip at similar velocities and contact area

equilibrates to a reduced value. The left y-axis in those figures represents

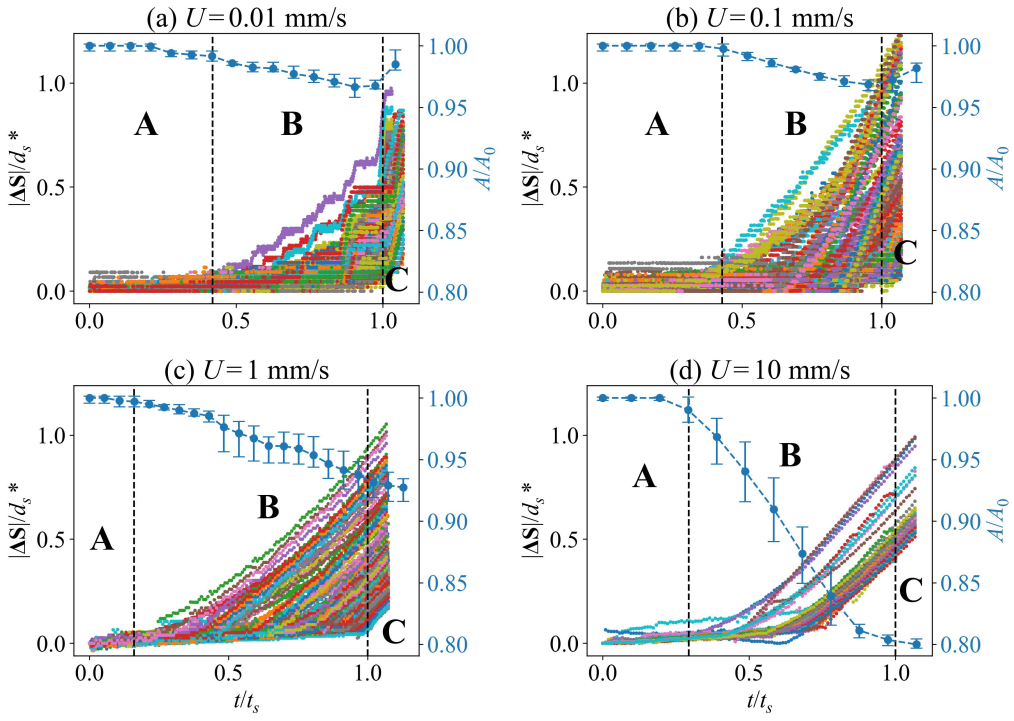

Figure 4.9: The magnitude of the slip vector normalized by the relative displacement without slippage and the contact area evolution normalized by the initial contact area A_0 as a function of time normalized by t_s for different $U = [0.01 - 10]$ mm/s. t_s is the onset of full sliding. A fully stuck regime; B partial slip regime, C full sliding.

the magnitude of the particle slip, $|\mathbf{\Delta S}|$, normalized by macroscopic shear d_s^*, where $d_s^* = \mu_s F_n / 8 a_0 G^*$, and G^* is the contact shear modulus given by $G^* = (2 - \nu)/G$. Macroscopic shear d_s^* is the maximum shear that a fully-adhered interface can experience at each driving velocity. Hence, normalized particle slip values are confined to [0, 1] range. The right

y-axis shows the evolution of the contact area, normalized by the initial contact area A_0, while the x-axis denotes time normalized by t_s, the time of the onset of full sliding. In Regime A, the contact area remains nearly constant, and the slip magnitude is negligibly small ($|\boldsymbol{\Delta S}|/d_s^* \leq 0.05$). This behavior resembles the stick-zone observed in probe-tack adhesion tests for viscoelastic materials, where changes in contact area are minimal during the initial stages of unloading (Lee and Eriten, 2024; Violano et al., 2021b; Müser and Persson, 2022). In Regime B, a significant amount of local slip commences and accumulates, accompanied by a noticeable reduction in contact area. This behavior is in contradiction with the predictions of both the classical Cattaneo-Mindlin model (Mindlin, 1949; Cattaneo, 1996) and the slip-based failure model by Savkoor and co-workers (Savkoor and Briggs, 1977; Savkoor, 1992). In the Cattaneo-Mindlin model, the contact area remains unchanged, and slip initiates at the contact edge as loading increases. In the slip-based failure model, peeling is assumed to precede slippage, with the contact area shrinking due to adhesive interactions near the edge. Slippage then propagates inward from the edge while maintaining a circular contact shape.

Contact area shrinkage exhibits a clear rate-dependence, as shown in Fig. 4.9. At low sliding speeds ($U = 0.01$ and 0.1 mm/s), the contact area changes minimally—by no more than 4%. In contrast, at higher speeds ($U = 1$ and 10 mm/s), the contact area reduces significantly, by approximately 7% and 20%, respectively. This trend contrasts with

the findings of Papangelo (Papangelo, 2021), who developed an analytical model based on Linear Elastic Fracture Mechanics (LEFM). In his model, rate-dependent effects are introduced through interfacial adhesion mechanisms, such as the Gent and Schultz law (Gent and Schultz, 1972). Papangelo observed that slower shear rates lead to greater contact area reduction up to 50% of its initial contact area, while at higher rates, the contact area remains nearly constant—close to the JKR value—because the system lacks time to respond. Additionally, higher loading rates increase the mechanical energy required to transition from full stick to gross sliding, indicating a toughening of the interface and a greater resistance to sliding initiation. In contrast, our experimental results show the opposite trend in contact area evolution: faster loading rates lead to greater contact area shrinkage. However, the energy-related behavior is consistent with Papangelo's model. Specifically, we observe that higher loading rates require more mechanical energy to transition from full stick to gross sliding, indicating a toughening of the interface and increased resistance to sliding initiation.

We next adopted an energetic approach to evaluate the contributions of slippage and peeling to friction during pre-sliding, as illustrated in Figure 4.10. We define two non-dimensional parameters, Φ and Θ, to quantify the relative contributions of slippage and peeling:

$$\Phi \equiv \frac{\frac{1}{2}\mu_s F_n \overline{\Delta S_{\tilde{\xi}}}}{\frac{1}{2}\mu_s F_n d_s^*}, \tag{4.3}$$

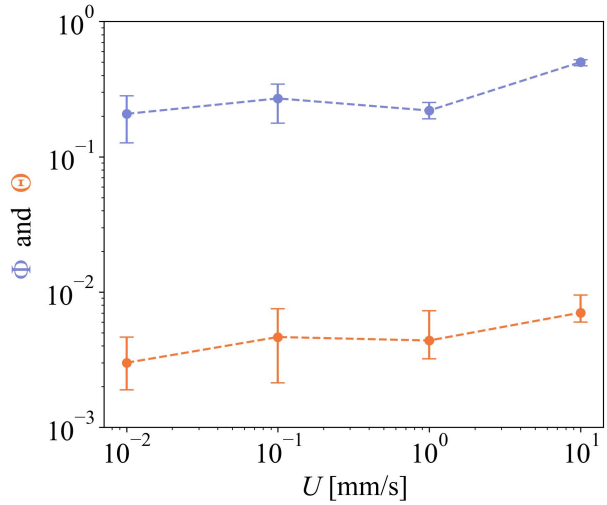

Figure 4.10: Φ and Θ as a function of the driving velocity U. Φ is the ratio of the energy dissipation by the partial slip to the strain energy. Θ is the ratio of the surface energy for area reduction in pre-sliding to the strain energy.

$$\Theta \equiv \frac{(\beta\Delta\gamma)\Delta A}{\frac{1}{2}\mu_s F_n d_s^*}, \tag{4.4}$$

Here, $\Delta\gamma \approx 0.07$ mJ/m^2 is the thermodynamic work of adhesion for gelatin (Lee and Eriten, 2024), and β is the enhancement factor of adhesion due to crack velocity. Since direct measurement of surface energy is challenging due to its strong rate dependence and complex mode mixity fracture, we use a power-law relation from our previous study (Lee and Eriten, 2024), assuming mode-independence of rate-dependent fracture: $\beta \sim (V_c/V_{c,0})^{0.39}$, where $V_{c,0} \approx 0.05$ mm/s is the lowest observed crack velocity. The average crack velocities V_c in regime B for driving velocities $U = 0.01, 0.1, 1, 10$ mm/s are approximately $1.5 \times 10^{-3}, 1.7 \times 10^{-2}, 1.9 \times 10^{-1}, 2.5$

mm/s, respectively. For $U = 0.01$ and 0.1 mm/s, $V_c < V_{c,0}$, so $\beta \to 1$. For $U = 1$ and 10 mm/s, β is estimated to be 1.7 and 4.6, respectively. The term d_s^* denotes the relative shear displacement without slippage, estimated using the CM model, and $\overline{\Delta S_\xi}$ is the average partial slip displacement in the ξ-direction. As shown in Figure 4.10, across all driving velocities ($U = 0.01$–10 mm/s), $\Phi \gg \Theta$, indicating that energy dissipation due to slippage dominates over peeling. The ratio Θ/Φ remains nearly constant at approximately $0.8, 0.8, 1.8, 1.2\%$ for increasing U, suggesting that pre-sliding friction in gelatin is primarily governed by slippage rather than peeling across the tested velocity range.

4.4 Conclusion

This study explored the rate-dependent frictional behavior of gelatin in the pre-sliding regime using a custom-built friction tester with *in-situ* contact imaging. By tracking the motion of surface defects, we quantified local slip, displacement fields, and contact area evolution under varying shear velocities. Our results reveal three distinct regimes of interfacial behavior—fully sticking, partial slip, and full sliding—whose transitions are strongly influenced by the driving velocity. Notably, we observed significant contact area shrinkage at higher velocities, accompanied by anisotropic deformation aligned with the shear direction. These findings deviate from classical friction models, such as the CM model and Savkoor-type model, which

assume constant contact area or different failure mechanisms. While the Cattaneo-Mindlin model captures the qualitative features of partial slip, it underestimates the slip magnitude due to its neglect of rate-dependent friction and evolving contact geometry. Our comparison between theoretical and experimental slip further highlights the need for models that incorporate interfacial adhesion dynamics, slip-rate dependence, and contact area evolution. Importantly, we show the ratio of dissipated to stored energy and the ratio of surface energy to stored energy, indicating that slippage is much more dominant than the peeling. These insights advance our understanding of pre-sliding friction in soft, hydrated materials and underscore the limitations of classical models in such systems. Future work may focus on incorporating time-dependent adhesion and poroelastic effects into predictive models, and exploring how gel composition or surface chemistry modulates interfacial mechanics.

5 CHAPTER 5. CONCLUSIONS AND FUTURE RESEARCH

5.1 Summary and Conclusions

The primary objective of this dissertation is to investigate the tribological behavior of gelatin—specifically its adhesion and friction characteristics—and their rate dependency, which arises from gelatin's complex structure and composition. Gelatin, a representative physical hydrogel, consists of polypeptide chains forming a triple-helix structure and is swollen with water. This unique configuration results in complex bulk viscoelastic and poroelastic properties, as well as intricate interfacial bond dynamics, all of which contribute to the strong rate-dependence observed in its adhesion and friction behavior.

In the initial phase of this research, a custom-built probe-tack tester with *in-situ* imaging was developed to investigate the effects of unloading rate and dwelling time on gelatin adhesion. The results demonstrated that the unloading rate has a dominant influence on the apparent work of adhesion, increasing it by up to tenfold, while dwelling time contributed an additional 40% increase. The suction effect, driven by poroelastic diffusion during loading and dwelling, was identified as the primary mechanism behind the dwelling time dependency. The Persson and Brener model (Persson and Brener, 2005) for viscoelastic crack propagation captured the rate-dependent behavior well, validating the use of viscoelastic frac-

ture mechanics in poroviscoelastic systems. This chapter established the foundational understanding of how time-dependent bulk and interfacial processes interact in soft adhesive contacts. An intriguing observation in this study was the monotonic acceleration of the crack during unloading, which serves as the motivation for the second phase of this research.

Building on these findings, Chapter 3 focused on the transient adhesion behavior of gelatin during peeling. Using force-displacement data and *in-situ* imaging, the study revealed that while crack velocity increases monotonically during unloading, the energy release rate exhibits a non-monotonic trend. This behavior was attributed to crack acceleration, viscoelastic dissipation, and size effects. The JKR theory (Johnson et al., 1971) was applied to estimate energy release rates, and de Gennes' viscoelastic crack propagation model (de Gennes, 1996), incorporating a standard linear solid, was used to simulate the observed behavior. Although the model qualitatively captured the experimental trends, it failed to fully explain the non-monotonic energy release, suggesting that interfacial rate-dependency must be considered alongside bulk viscoelasticity. This chapter highlighted the importance of transient dynamics and boundary effects in understanding soft material adhesion.

In the final chapter of this dissertation, the focus shifted to frictional behavior in the pre-sliding regime. A custom friction tester with *in-situ* imaging was developed to study how driving velocity affects static friction and interfacial slip in gelatin. The experiments showed that static friction

force increases with velocity (velocity-strengthening behavior), and that contact area reduction becomes more pronounced at higher velocities. Tracer particles embedded in the gelatin surface enabled visualization of displacement fields, revealing partial slip and the evolution of contact area from circular to elliptical. Three distinct regimes were identified: a fully stuck regime with negligible slip and area change, a partial slip regime with moderate slip and reduction in the contact area, and a fully sliding regime with large slip and negligible area change. Comparisons with the Cattaneo-Mindlin theory (Cattaneo, 1996; Mindlin, 1949) showed qualitative agreement, despite the model's assumptions of elasticity and constant contact area. The findings suggest that energy dissipation is dominated by the partial slip rather than the peeling.

Collectively, this dissertation advances the understanding of how viscoelastic and poroelastic relaxation mechanisms, along with interfacial dynamics, influence adhesion and friction in soft materials. The integration of *in-situ* imaging provided critical insights into transient interfacial phenomena that are often inaccessible through force measurements alone. The findings underscore the need for comprehensive models that incorporate both bulk and interfacial rate-dependent behavior to accurately describe the contact mechanics of soft, multiphasic materials like gelatin.

5.2 Preliminary Results

Rate-dependent adhesion in polyacrylamide hydrogel

Using the same setup employed for adhesion tests on 5 wt% gelatin, a separate configuration is used to conduct adhesion tests on 8 wt% polyacrylamide (PAAm) hydrogel, as illustrated in Fig. 2.1(a). Notably, both hydrogels exhibit comparable stiffness values ($E \sim$ 10–20 kPa) and similar thermodynamic work of adhesion ($\Delta\gamma \sim$ 0.06–0.07 J/m^2). The unloading rate V_u is varied from 0.01 to 10 mm/s, and the material is in contact with a spherical shape of glass probe. In the PAAm hydrogel, N,N'-methylenebisacrylamide (MBAA or BIS) serves as the chemical crosslinker, while ammonium persulfate (APS) is used as the free radical initiator. PAAm hydrogel represents a typical chemical gel, whereas gelatin is classified as a physical gel. Chemical gels are generally characterized by lower bulk viscoelasticity compared to physical gels, owing to the presence of strong covalent bonds within their polymer networks. This preliminary experiment aims to investigate the distinct rate-dependent adhesive behaviors exhibited by physical and chemical gels. Fig. 5.1 presents the enhancement of work of adhesion, defined as $\beta = G/\Delta\gamma$, as a function of the unloading rate V_u for both 5 wt% gelatin (Lee and Eriten, 2024) and 8 wt% PAAm hydrogel. The dwelling time, loading rate, and loading displacement is 0.5 s, 10 mm/s and 0.5 mm, respectively, across all

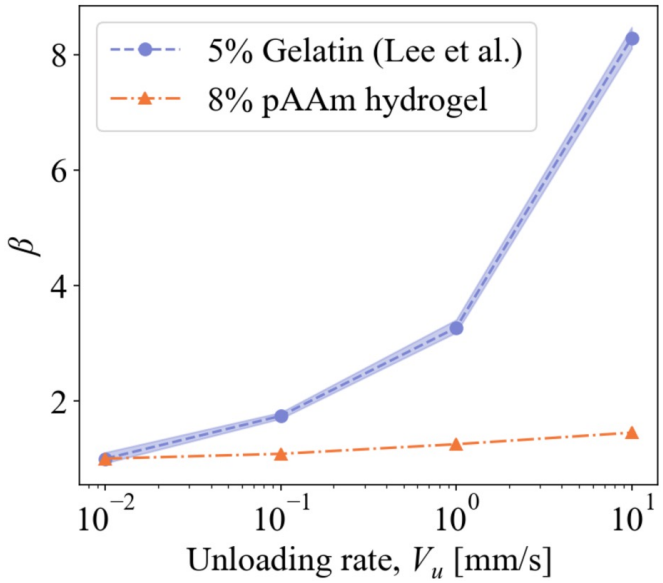

Figure 5.1: The enhancement of work of adhesion $\beta = G/\Delta\gamma$ as a function of the unloading rate V_u for 5 w/v% gelatin (Lee and Eriten, 2024) and 8 w/v% PAAm hydrogel.

test conditions. At the slowest unloading rate, the thermodynamic work of adhesion ($\Delta\gamma$) is estimated to be 0.07 J/m^2 for gelatin and 0.06 J/m^2 for PAAm hydrogel. The apparent work of adhesion is calculated as the work of separation per unit contact area. Notably, the work of adhesion increases by approximately eightfold for gelatin, whereas only a 40% increase is observed for PAAm hydrogel. This discrepancy may be attributed to differences in bulk viscoelasticity between chemical and physical gels.

Additionally, the glass substrate used in the tests is primarily composed of silica (SiO_2) with surface silanol groups ($-$Si–OH), rendering it hydrophilic and capable of forming hydrogen bonds with other functional

groups. In the case of PAAm hydrogel, the polymer chains contain amide side groups ($-CONH_2$), which can form hydrogen bonds with the silanol groups on the glass surface. Gelatin, however, possesses a greater variety of functional groups—including amine ($-NH_2$), carboxyl ($-COOH$), and hydroxyl ($-OH$) groups—enabling more extensive hydrogen bonding with the glass. These molecular interactions may explain why gelatin exhibits a slightly higher thermodynamic work of adhesion than PAAm hydrogel, as well as a more pronounced rate-dependent adhesive behavior. Nevertheless, further investigation is required to determine the contributions of bulk viscoelasticity and interfacial dynamics to the rate-dependent adhesion observed in different types of hydrogels.

Effect of sample thickness on adhesion behavior in gelatin

A 5 wt% gelatin sample is prepared with a reduced thickness to investigate the influence of sample geometry on rate-dependent and poroelastic-diffusion-dependent adhesion. Adhesion tests are conducted using the same setup shown in Fig. 2.1, with contact area evolution monitored via the integrated imaging module. To examine the effect of unloading rate on adhesion, the rate is varied from 0.01 to 10 mm/s. Additionally, the influence of dwelling time is assessed by varying it from 0.5 s to 200 s. The gelatin sample has a radial dimension of 50 mm and a thickness of 5 mm, resulting in a thickness-to-contact-radius ratio close to 1. This geometric configuration invalidates the half-space assumption, as the sample

thickness is comparable to the contact radius. Consequently, the poroelastic time constant is reduced relative to that of a half-space, since fluid diffusion predominantly occurs in the radial direction rather than the axial direction. Fig. 5.2(a) presents the enhancement of work of adhesion, defined as $\beta = G/\Delta\gamma$, as a function of the normalized crack velocity $V_c/V_{c,0}$ for gelatin samples of varying thickness. In this study, the ther-

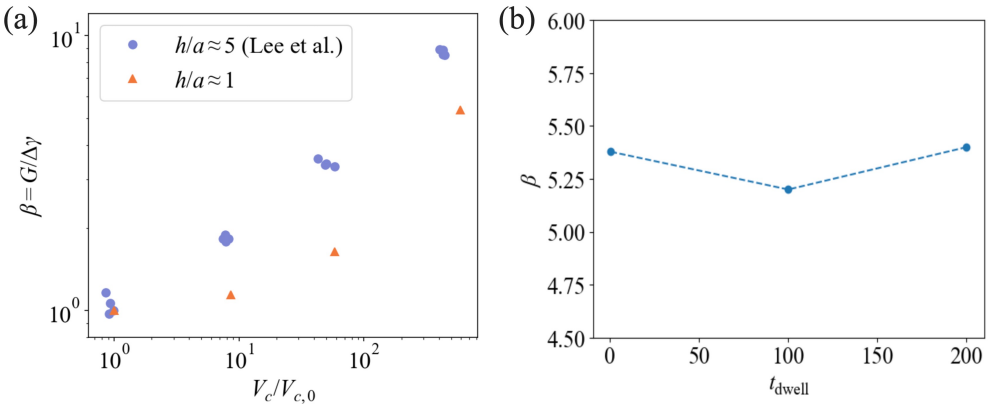

Figure 5.2: (a) The enhancement of work of adhesion $\beta = G/\Delta\gamma$ as a function of the crack velocity normalized by the slowest crack velocity $V_c/V_{c,0}$. (b) The enhancement of work of adhesion as a function of the dwelling time t_{dwell} for thin layer of gelatin with $h/a \approx 1$.

modynamic work of adhesion remains nearly identical across samples, with $\Delta\gamma = 0.07$ J/m^2. While the crack velocity is largely unaffected by the sample thickness, the enhancement of work of adhesion is significantly influenced by it. Specifically, a 5 fold increase is observed for the thin gelatin layer, whereas the thicker gelatin sample exhibits an 8 fold increase with increasing crack velocity (or unloading rate) (Lee and Eriten,

2024). Fig. 5.2(b) illustrates the enhancement of work of adhesion as a function of dwelling time t_{dwell} for the thin gelatin layer with a thickness-to-contact-radius ratio of $h/a \approx 1$. While the thick gelatin sample shows approximately a 40% increase in adhesion as dwelling time increases from 0.5 s to 200 s, the thin layer exhibits negligible sensitivity to dwelling time. This behavior may be due to the absence of a pressure gradient in the longitudinal direction within the thin gelatin layer. These preliminary findings clearly demonstrate the finite-size effects on both rate-dependent and poroelastic-diffusion-dependent adhesion in gelatin. Further investigation using samples with thicknesses approaching the size of the process zone near the crack tip could provide deeper insight into size effects and help determine the respective contributions of bulk viscoelasticity and interfacial dynamics to rate-dependent adhesion in gelatin.

5.3 Future Research

Determining bulk and interfacial contributions to rate-dependent adhesion in gels

Through the work presented in this dissertation, both experimental and theoretical results suggest that rate-dependent adhesion and friction in gelatin arise not only from bulk viscoelasticity but also from the rate-dependent nature of the interface. However, gelatin typically contains a

low solid content—usually less than 20 w/v%—and experimental observations, including rheological measurements and relaxation tests, consistently show a low loss tangent ($\tan\delta < 0.2$) (Ross-Murphy, 1992, 1991) and negligible viscoelastic relaxation ($E_\infty/E_0 \approx 1$) (Lee and Eriten, 2024; Yengul et al., 2019; Mitchell, 1980). According to classical viscoelastic crack propagation models, such minimal bulk viscoelasticity cannot account for the 8 to 10 fold increase in adhesion observed with increasing unloading rates, as reported in Chapter 2. In contrast, PAAm hydrogel exhibits an even smaller loss tangent ($\tan\delta \ll 10^{-2}$) (Calvet et al., 2004), and this difference in viscoelasticity may help explain the contrasting rate-dependent adhesion behaviors observed in the preliminary results of Section 5.2. Adhesion tests on these two distinct gel types, which exhibit clear differences in rheological properties, provide valuable insight into the contribution of bulk viscoelasticity to rate-dependent adhesion in gelatin. Furthermore, using thin gel layers with thicknesses comparable to or smaller than the process zone near the crack tip may help isolate bulk viscoelastic effects and allow for focused investigation of interfacial contributions. In this context, understanding the rheological behavior of the gels becomes essential. However, characterizing the rheology of gelatin presents significant challenges. At very low frequencies ($f < 0.001$ Hz), issues such as thermal drift, mechanical instability, and dehydration complicate measurements. At high frequencies ($f > 1000$ Hz), inertial artifacts and limitations in data acquisition become problematic. To

overcome these limitations, the time–temperature superposition principle—often modeled using the Williams–Landel–Ferry (WLF) equation (Williams et al., 1955)—is commonly employed in rheology. However, gelatin is a thermoreversible material that transitions to a sol state near its melting point ($32\ ^{\circ}C$) (Yoshimura et al., 2000), making it unsuitable for temperature-based shifting. This thermoreversibility significantly hinders the ability to fully characterize gelatin's rheological properties, which are critical for understanding the role of bulk viscoelasticity in rate-dependent adhesion.

Rate-dependent adhesion and friction for multi-asperity contact

In this dissertation, the primary focus has been on spherical contact between a sphere and a flat surface. This configuration serves as an idealized model for single-asperity contact, which is analogous to the interaction between individual surface asperities in real-world contact scenarios. However, in practical applications, surfaces are typically rough and composed of numerous asperities. Therefore, understanding multi-asperity contact is essential for accurately modeling and predicting real contact behavior (Pradhan et al., 2025). Moreover, multi-asperity contact can be leveraged as a design parameter. By controlling the distribution of asperity heights, spacing, and sizes, it is possible to tailor macroscopic properties such as the

resultant adhesive force or friction coefficient to meet specific performance requirements (Aymard et al., 2024). Theoretical approaches such as the Greenwood–Williamson model (Greenwood and Williamson, 1966) offer a statistical framework for analyzing and designing multi-asperity contacts. Alternatively, numerical methods like the boundary element method (BEM) or finite element modeling (FEM), when integrated with adhesive interfacial models and/or rate-and-state friction model, provide powerful tools for simulating and optimizing contact mechanics in complex systems (Lee and Eriten, 2023).

A APPENDIX A*

(*This appendix is documented for the supplementary material for Chapter 2.)

A.1 Relaxation Time Constants

The single poroelastic time constant (τ_{PE}) and the single viscoelastic time constant (τ_{VE}) are estimated from 16 relaxation tests. Fig. A.1 depicts a representative poroviscoelastic relaxation as a function of time. Initially,

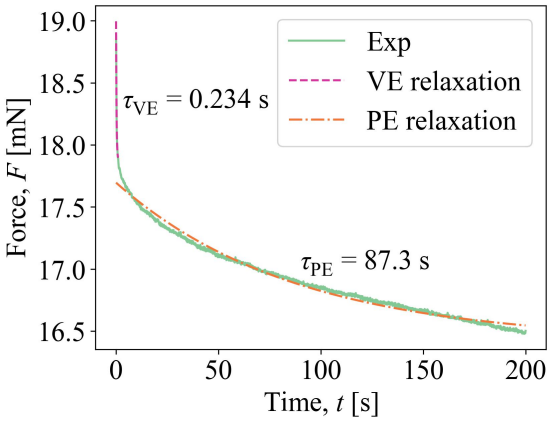

Figure A.1: Representative relaxation curve from the adhesion experiments with a holding time of $t_{dwell} = 200$ s. The curve illustrates two relaxation time constants:τ_{VE}, which covers the initial relaxation from 0 to 1 s, and τ_{PE}, which captures the broader range of relaxation from 0 to 200 s.

we apply a Gaussian filter with $\sigma = 15$ to eliminate noise. Subsequently, we fit the filtered curve to Eq. (1), where τ denotes a relaxation time

constant, and F_∞ and F_0 are constants.

$$F(t) = F_\infty + F_0 e^{-t/\tau} \tag{A.1}$$

Typically, poroelastic relaxation occurs much slower than viscoelastic relaxation. For a typical gelatin, τ_{VE} is less than 1 s. The poroelastic relaxation time constant can be expressed as $\tau_{\mathrm{PE}} \sim a^2/D_{\mathrm{eff}}$. For a hydrogel swollen with a water solvent, D_{eff} is on the order of 10^{-7} m^2/s to 10^{-10} m^2/s (Esteki et al., 2020; Hu et al., 2010; Reale and Dunn, 2017). This results in $\tau_{\mathrm{PE}} \sim 84 - 84000s$ which is significantly larger than τ_{VE}. Here, the contact radius $a \approx 2.9$ mm, which is imaged by the imaging module (see §2.3 of the main text for details). The two relaxation time constants, τ_{PE} and τ_{VE}, are distinct. Therefore, we assume that the viscoelastic effect is dominant at the initial region of the relaxation curve. This assumption is supported by the observable sudden drop in the early stage of the curve, as shown in Fig. A.1. We use this observation to estimate τ_{PE} and τ_{VE}. The entire relaxation curve relaxed for 200 s is fitted to Eq. A.1 to obtain τ_{PE}. We then fit the initial relaxation curve (being relaxed for 1 s) to Eq. A.1 and estimate τ_{VE}. The estimated poroelastic relaxation time constants, τ_{PE}, ranges from 73.2 to 111 s, with an average of 87.0 s. The estimated viscoelastic relaxation time constants,τ_{VE}, ranges from 0.186 to 0.239 s, with an average of 0.222 s.

A.2 Vertical Extension

Soft materials, such as gelatin, due to their high compliance and strong adhesion, can form a pillar shape with a length h (referred to as vertical extension) when two interfaces are separated. If the unloading rate is sufficiently slow compared to the viscoelastic relaxation, the vertical extension h can be estimated using Eq. A.2.

$$h = \Delta t_u V_u - \delta_l \tag{A.2}$$

Here, Δt_u is the duration of unloading from the start to full separation, and $\delta_l = 0.5$ mm is the loading displacement in the adhesion experiments. However, if the interfaces are separated quickly, Eq. A.2 may no longer hold, as the interfaces can separate before the material fully recovers (viscoelastically). In such cases, we experimentally measure the vertical extension h and validate our estimation. Fig. A.2(a) presents the duration of unloading Δt_u normalized by τ_{VE} as a function of V_u. The shaded area indicates the range of maximum and minimum values. $\Delta t_u / \tau_{\mathrm{VE}}$ provides a measure of how quickly we unload the indenter compared to the viscoelastic relaxation. For $V_u = \{0.01, 0.1, 1\}$ mm/s cases, the unloading is slow enough that the deformed material has sufficient time to recover while we unload the probe. On the other hand, for fast unloading cases such as $V_u = 10$ mm/s, the material may not have enough time

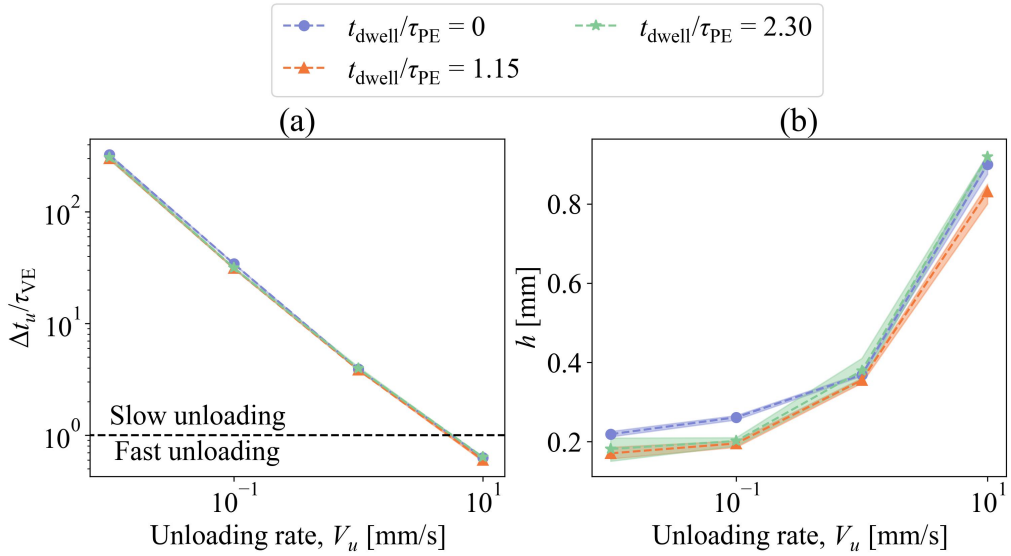

Figure A.2: (a) The duration of unloading, from the start of unloading to full separation, normalized by the viscoelastic relaxation time $\Delta t_u/\tau_{VE}$. (b) The estimated vertical extension h. The shaded area in both figures represents the range between the maximum and minimum values.

to recover viscoelastically during unloading. If we estimate the vertical extension h using Eq. A.2 for $V_u = 10$ mm/s cases, the crack tip opening is likely to be underestimated. Therefore, for the fastest unloading case $V_u = 10$ mm/s, the vertical extension is estimated using Eq. A.2 and validated by experimental measurements using the imaging module. Fig. A.2(b) displays the estimated vertical extension h. The vertical extension h at $t_{dwell}/\tau_{PE} = 0$ and $V_u = 10$ mm/s is estimated to be 0.900 mm. Fig. A.3 illustrates the evolution of the vertical extension captured by the imaging module from the side view. Fig. A.3(A) and (D) are the tilted side views of

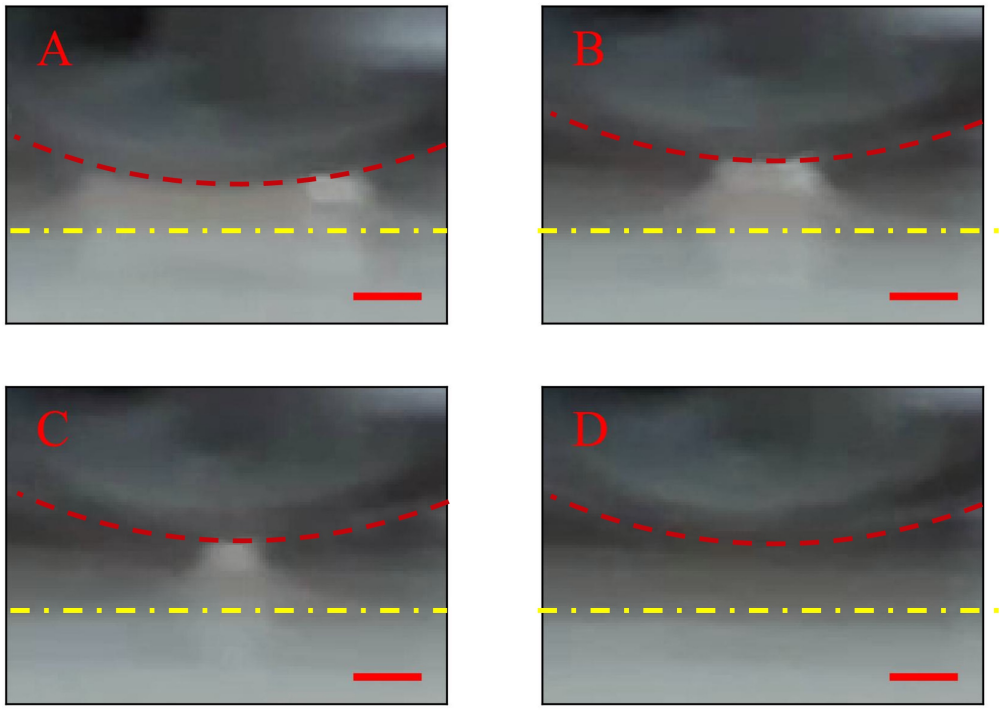

Figure A.3: Evolution of the vertical extension viewed from the side for $V_u = 10\,\mathrm{mm/s}$ and $t_{\mathrm{dwell}} = 0.5\,\mathrm{s}$ case at the instant of (A) pull-off, (B) and (C) right before the full separation, and (D) right after the full separation. The red dashed lines denote the contour of the probe, while the yellow dashed lines represent the baseline of the vertical extension. (Scale bar: 1 mm)

the contact at the instant of pull-off and immediately after full separation, respectively. Fig. A.3(B) and (C) are the images right before the full separation with time interval of 1/240 s. The images are captured with a spatial resolution of 44 ¯m. The crack-tip radius of 0.85 mm can be fitted to the curved visible portion of the contact edge and that radius is close to the maximum vertical extension. Besides, the crack tip shape is maintained during unloading. Similar analysis for other unloading rate cases is not possible due to smaller vertical extensions ($h < 400$ ¯m), 3 dimensional geometry of contact and tilted side view. The experimentally measured vertical extension is $h = 0.903$ mm, which closely matches the estimation. This suggests that the deformed material has either almost or fully recovered because the unloading duration at $V_u = 10$ mm/s is comparable to τ_{VE}.

B APPENDIX B*

(*This appendix is documented for the supplementary material for Chapter 4.)

B.1 Defects on Gels

Fig. B.1 shows the images of gel and the gel surface with defects. The

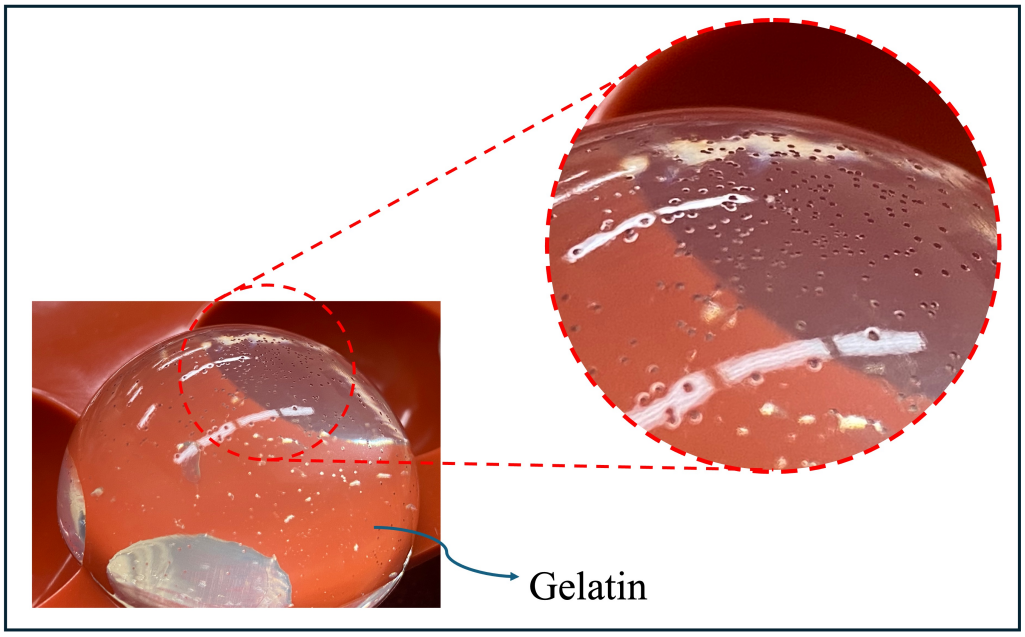

Figure B.1: The real image of gelatin sample and the gel surface with defects. The radius of the sample R is 18 mm.

radius of the gelatin sample R is 18 mm. The defects may be originated from the silicone mold. To validate this, the microscopic image of the gel

surface and the mold surface are taken as shown in Fig. B.2. The shape of

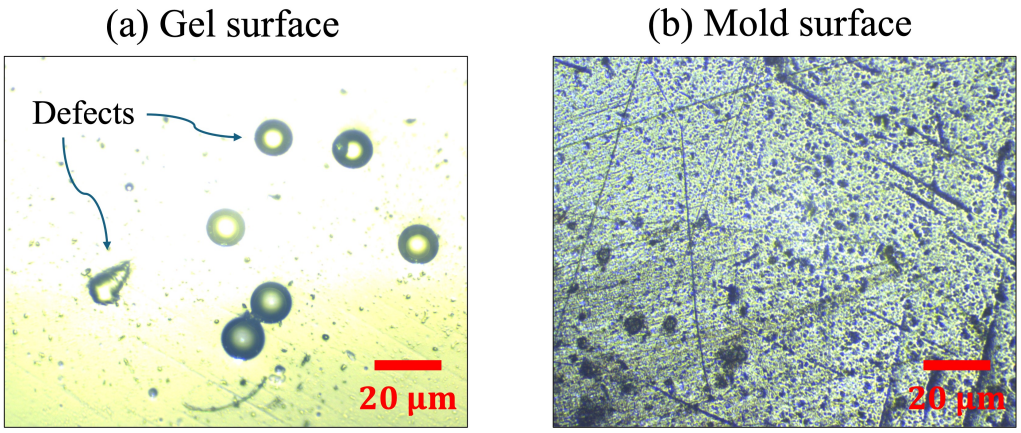

Figure B.2: The microscopic images of the gel surface and the mold surface. The scale bar in the image is 20 μm.

defects on the gel are mostly circular with the diameter ranging from 10 to 20 μm. The sketch-like lines are also observable in diagonal direction in Fig. B.2(a). These defects and lines are likely to be molded from the silicone mold shown in Fig. B.2(b).

B.2 Dependence of Displacement on the Location of Particles

Fig. B.3(a-d) shows the movement of particles at $U = 0.01$ mm/s and its corresponding coordinates. The figures show the dependence of particles' movement on its positions (e.g., dependence on ξ and η). In Fig. B.3(a-b),

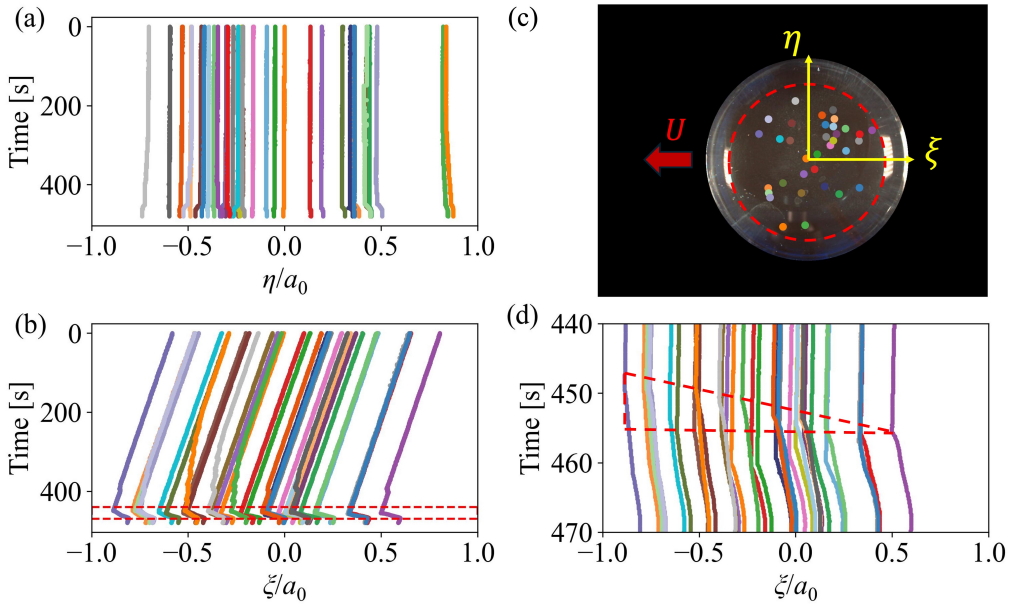

Figure B.3: The change of particles location normalized by the initial contact radius in the initial configuration: (a) η component; (b) ξ component. (c) shows the particles initial location and the contact edge with the red dashed line in the initial configuration. The initial contact radius a_0 is around 14 mm. (d) shows the ξ component of particles location near the transition from the partial slip to the fully sliding.

it shows the coordinates of the particles normalized by the initial contact area, η/a_0 and ξ/a_0 over time up to second phase of stick-slip oscillation. Note that the origin of the axes ξ and η is the center of the initial contact area at $t = 0$ as shown in Fig. B.3(c), which shows the initial positions of the particles over the contact area. In Fig. B.3(a-b), the particles move mostly in the direction parallel to the one of driving velocity, i.e., ξ-direction in presliding regime. In presliding regime, the particles move mostly in the

negative ξ-direction monotonously as the most of particles on gels stick to the glass (micro-slip or partial slip will be discussed in the following section), and the tangential force increases. The particles start sliding, and the particles move backward in positive ξ-direction as the particles recover. Fig. B.3(d) shows the zoomed-in version of B.3(c) at around the static friction force in Fig. 4.3(a). The sliding starts initially near the leading edge ($\xi/a_0 = -1$) at around 437 s and ends lastly near the following edge ($\xi/a_0 = 1$) at around 455 s. The transition from stick to full sliding, marked by a change in slope and indicated by the red dashed line in Fig. B.3(d), propagates from the leading edge to the following edge at a speed of 2 mm/s. This velocity is on the same order of magnitude to the slip-pulse velocity (≈ 8 mm/s) found in Ref(Baumberger et al., 2002) for flat-flat contact with 5 w/v% gelatin and glass.

Baumberger et al.(Baumberger et al., 2002, 2003) Ben-David et al.(Ben-David et al., 2010), and Rubinstein et al.(Rubinstein et al., 2004) observed experimentally that the frictional slip or rupture is initiated from the front edge (or leading edge) and propagates to the following edge in a form of slip-pulse in gelatin(Baumberger et al., 2002, 2003) and brittle polymer(polymethyl-methacrylate, PMMA)(Rubinstein et al., 2004; Ben-David et al., 2010). Especially, Baumberget et al.(Baumberger et al., 2002) and Brochard-Wyart and de Gennes(Brochard-Wyart and de Gennes, 2007) postulate that the slip-pulse in gels can be characterized by the poroelastic nature of gels and the velocity of slip-pulse is given by, $V_{\text{slip}} \sim D/\zeta$,

where D and ζ are the diffusion coefficient and a mesh size, respectively. Baumberger et al. (Baumberger et al., 2002) showed in his experiments for 5 v/w% gelatin using images that the slip-pulse velocity is around 8 mm/s, which is in a good agreement with the theoretical one $D/\zeta \sim 10$ mm/s.

REFERENCES

Afferrante, Luciano, and Guido Violano. 2022. On the effective surface energy in viscoelastic hertzian contacts. *Journal of the Mechanics and Physics of Solids* 158:104669.

Ahmed, J. 2017. Rheological properties of gelatin and advances in measurement. In *Advances in food rheology and its applications*, 377–404. Elsevier.

Argatov, II, IA Lyashenko, and VL Popov. 2023. Rate-dependent jkr-type decohesion of a cylindrical punch from an elastic substrate. *Physica Scripta* 98(5):055905.

Argatov, Ivan I, Iakov A Lyashenko, and Valentin L Popov. 2024. Ad hoc modeling of rate-dependent adhesion in indentation relaxation testing. *Materials* 17(16):3944.

Asawalertsak, Naris, Franziska Heims, Alexander Kovalev, Stanislav N Gorb, Jonas Jørgensen, and Poramate Manoonpong. 2023. Frictional anisotropic locomotion and adaptive neural control for a soft crawling robot. *Soft Robotics* 10(3):545–555.

ASTM International. 2018. ASTM E1820-18: Standard Test Method for Measurement of Fracture Toughness. Tech. Rep., ASTM International, West Conshohocken, PA.

Aymard, Antoine, Emilie Delplanque, Davy Dalmas, and Julien Scheibert. 2024. Designing metainterfaces with specified friction laws. *Science* 383(6679):200–204.

Baumberger, Tristan, Christiane Caroli, and David Martina. 2006a. Fracture of a biopolymer gel as a viscoplastic disentanglement process. *The European Physical Journal E* 21:81–89.

———. 2006b. Solvent control of crack dynamics in a reversible hydrogel. *Nature materials* 5(7):552–555.

Baumberger, Tristan, Christiane Caroli, and Olivier Ronsin. 2002. Self-healing slip pulses along a gel/glass interface. *Physical review letters* 88(7): 075509.

———. 2003. Self-healing slip pulses and the friction of gelatin gels. *The European Physical Journal E* 11:85–93.

Baumberger, Tristan, and Olivier Ronsin. 2009. From thermally activated to viscosity controlled fracture of biopolymer hydrogels. *The Journal of chemical physics* 130(6).

Ben-David, Oded, Gil Cohen, and Jay Fineberg. 2010. The dynamics of the onset of frictional slip. *Science* 330(6001):211–214.

Benkherourou, Mohamed, P-Y Gumery, Léone Tranqui, and Philippe Tracqui. 2000. Quantification and macroscopic modeling of the nonlinear

viscoelastic behavior of strained gels with varying fibrin concentrations. *IEEE transactions on biomedical engineering* 47(11):1465–1475.

Benson, JM, AC Moore, J Schrader, and DL Burris. 2024. Adhesion–lubrication paradox of articular cartilage. *Langmuir* 40(27):13810–13818.

Bode, Franziska, Marcelo Alves Da Silva, Paul Smith, Christian D Lorenz, Seth McCullen, Molly M Stevens, and Cécile A Dreiss. 2013. Hybrid gelation processes in enzymatically gelled gelatin: impact on nanostructure, macroscopic properties and cellular response. *Soft Matter* 9(29): 6986–6999.

Brochard-Wyart, F, and P G de Gennes. 2007. Naive model for stick-slip processes. *The European Physical Journal E* 23:439–444.

Budelli, Eliana, Javier Brum, Miguel Bernal, Thomas Deffieux, Mickaël Tanter, Patricia Lema, Carlos Negreira, and Jean-Luc Gennisson. 2016. A diffraction correction for storage and loss moduli imaging using radiation force based elastography. *Physics in Medicine & Biology* 62(1):91.

Calvet, Damien, Joyce Y Wong, and Suzanne Giasson. 2004. Rheological monitoring of polyacrylamide gelation: Importance of cross-link density and temperature. *Macromolecules* 37(20):7762–7771.

Cattaneo, Cs. 1996. Sul contatto de due corpi elastici: Distribuzione locale deglisforzi. *Rendiconti dell'Accademia nazionale dei Lincei* 6:342–349.

Cedano-Serrano, Francisco J, Ugo Sidoli, Alla Synytska, Yvette Tran, Dominique Hourdet, and Costantino Creton. 2019. From molecular electrostatic interactions and hydrogel architecture to macroscopic underwater adherence. *Macromolecules* 52(10):3852–3862.

Chan, Edwin P, Yuhang Hu, Peter M Johnson, Zhigang Suo, and Christopher M Stafford. 2012. Spherical indentation testing of poroelastic relaxations in thin hydrogel layers. *Soft Matter* 8(5):1492–1498.

Cheng, Alexander H-D. 2016. *Poroelasticity*, vol. 27. Springer.

Corvera-Paredes, Beatriz, Aidee I Sánchez-Reséndiz, Dora I Medina, Rosa S Espiricueta-Candelaria, Sergio Serna-Saldívar, and Cristina Chuck-Hernández. 2022. Soft tribology and its relationship with the sensory perception in dairy products: A review. *Frontiers in Nutrition* 9:874763.

Creton, Costantino, and Matteo Ciccotti. 2016. Fracture and adhesion of soft materials: a review. *Reports on Progress in Physics* 79(4):046601.

Cuccia, Nicholas L, Suraj Pothineni, Brady Wu, Joshua Méndez Harper, and Justin C Burton. 2020. Pore-size dependence and slow relaxation of hydrogel friction on smooth surfaces. *Proceedings of the National Academy of Sciences* 117(21):11247–11256.

Dalbe, Marie-Julie, Stéphane Santucci, Pierre-Philippe Cortet, and Loïc Vanel. 2013. Strong dynamical effects during stick-slip adhesive peeling. *Soft Matter* 10(1):132–138. 1311.3423.

Dalisay, Jon Dewitt E., Lejie Liu, Melih Eriten, Lawrence A. Bergman, and Alexander F. Vakakis. 2022. Characterization of visco-hyperelastic behavior of open cell polyurethane foam through transient shear testing. *International Journal of Solids and Structures* 241:111482.

De Gennes, Pierre-Giles. 1971. Reptation of a polymer chain in the presence of fixed obstacles. *The journal of chemical physics* 55(2):572–579.

De Gennes, Pierre-Gilles. 1979. *Scaling concepts in polymer physics*. Cornell university press.

Delavoipière, Jessica, Yvette Tran, Emilie Verneuil, Bertrand Heurtefeu, Chung Yuen Hui, and Antoine Chateauminois. 2018. Friction of poroelastic contacts with thin hydrogel films. *Langmuir* 34(33):9617–9626.

Derjaguin, Boris V, Vladimir M Muller, and Yu P Toporov. 1975. Effect of contact deformations on the adhesion of particles. *Journal of Colloid and interface science* 53(2):314–326.

Dieterich, James H. 1979. Modeling of rock friction: 1. experimental results and constitutive equations. *Journal of Geophysical Research: Solid Earth* 84(B5):2161–2168.

Dugdale, Donald S. 1960. Yielding of steel sheets containing slits. *Journal of the Mechanics and Physics of Solids* 8(2):100–104.

Dunn, Alison C, Angela A Pitenis, Juan M Urueña, Kyle D Schulze, Thomas E Angelini, and W Gregory Sawyer. 2015. Kinetics of aque-

ous lubrication in the hydrophilic hydrogel gemini interface. *Proceedings of the Institution of Mechanical Engineers, Part H: Journal of Engineering in Medicine* 229(12):889–894.

Dunn, Alison C, John A Tichy, Juan M Urueña, and W Gregory Sawyer. 2013. Lubrication regimes in contact lens wear during a blink. *Tribology International* 63:45–50.

Erfkamp, Jan, Margarita Guenther, and Gerald Gerlach. 2019. Piezoresistive hydrogel-based sensors for the detection of ammonia. *Sensors* 19(4): 971.

Esfahani, Amir Monemian, Jordan Rosenbohm, Bahareh Tajvidi Safa, Nickolay V Lavrik, Grayson Minnick, Quan Zhou, Fang Kong, Xiaowei Jin, Eunju Kim, Ying Liu, et al. 2021. Characterization of the strain-rate–dependent mechanical response of single cell–cell junctions. *Proceedings of the National Academy of Sciences* 118(7):e2019347118.

Esteki, Mohammad Hadi, Ali Akbar Alemrajabi, Chloe M Hall, Graham K Sheridan, Mojtaba Azadi, and Emad Moeendarbary. 2020. A new framework for characterization of poroelastic materials using indentation. *Acta biomaterialia* 102:138–148.

Ferry, John D. 1980. *Viscoelastic properties of polymers*. John Wiley & Sons.

de Gennes, PIERRE-GILLES. 1996. Soft adhesives. *Langmuir* 12(19): 4497–4500.

Gent, AN, and J Schultz. 1972. Effect of wetting liquids on the strength of adhesion of viscoelastic material. *The Journal of Adhesion* 3(4):281–294.

Gong, Jian Ping. 2006. Friction and lubrication of hydrogels—its richness and complexity. *Soft matter* 2(7):544–552.

Gong, Jianping, and Yoshihito Osada. 1998. Gel friction: a model based on surface repulsion and adsorption. *The Journal of chemical physics* 109(18): 8062–8068.

Greenwood, JA. 2004. The theory of viscoelastic crack propagation and healing. *Journal of Physics D: Applied Physics* 37(18):2557.

Greenwood, JA, and KL Johnson. 1981. The mechanics of adhesion of viscoelastic solids. *Philosophical Magazine A* 43(3):697–711.

———. 2006. Oscillatory loading of a viscoelastic adhesive contact. *Journal of colloid and interface science* 296(1):284–291.

Greenwood, James A, and JB Pl Williamson. 1966. Contact of nominally flat surfaces. *Proceedings of the royal society of London. Series A. Mathematical and physical sciences* 295(1442):300–319.

Greenwood, Jim A, and John H Tripp. 1967. The elastic contact of rough spheres. *J. Appl. Mech.* 34(1):153–159.

Haiat, G, MC Phan Huy, and E Barthel. 2003. The adhesive contact of viscoelastic spheres. *Journal of the Mechanics and Physics of Solids* 51(1): 69–99.

Hamilton, G_M_. 1983. Explicit equations for the stresses beneath a sliding spherical contact. *Proceedings of the Institution of Mechanical Engineers, Part C: Journal of Mechanical Engineering Science* 197(1):53–59.

Han, Guebum, Utku Boz, Melih Eriten, and Corinne R Henak. 2020a. Glycosaminoglycan depletion increases energy dissipation in articular cartilage under high-frequency loading. *Journal of the mechanical behavior of biomedical materials* 110:103876.

Han, Guebum, Utku Boz, Lejie Liu, Corinne R Henak, and Melih Eriten. 2020b. Indenter–foam dampers inspired by cartilage: Dynamic mechanical analyses and design. *Journal of Vibration and Acoustics* 142(5):051113.

Han, Guebum, and Melih Eriten. 2018a. Effect of relaxation-dependent adhesion on pre-sliding response of cartilage. *Royal Society open science* 5(5):172051.

———. 2018b. Effect of relaxation-dependent adhesion on pre-sliding response of cartilage. *R. Soc. Open Sci.* 5172051.

Han, Guebum, Melih Eriten, and Corinne R Henak. 2019. Rate-dependent crack nucleation in cartilage under microindentation. *Journal of the Mechanical Behavior of Biomedical Materials* 96:186–192.

———. 2020c. Rate-dependent adhesion of cartilage and its relation to relaxation mechanisms. *Journal of the mechanical behavior of biomedical materials* 102:103493.

He, Lang, Sheng Li, Chengzhi Xu, Benmei Wei, Juntao Zhang, Yuling Xu, Beirong Zhu, Yang Cao, Xilin Wu, Zhijin Xiong, et al. 2020. A new method of gelatin modified collagen and viscoelastic study of gelatin-collagen composite hydrogel. *Macromolecular Research* 28(9):861–868.

Hellwig, Johannes, Samantha Micciulla, Julia Strebe, and Regine von Klitzing. 2016. Separation of storage and loss modulus of polyelectrolyte multilayers on a nanoscale: A dynamic afm study. *Langmuir* 32(41): 10505–10512.

Hertz, Heinrich. 1881. The contact of elastic solids. *J Reine Angew, Math* 92:156–171.

Higgs, Paul G, and Simon B Ross-Murphy. 1990. Creep measurements on gelatin gels. *International Journal of Biological Macromolecules* 12(4): 233–240.

Hsu, Shan-hui, and Alexander M Jamieson. 1993. Viscoelastic behaviour at the thermal sol-gel transition of gelatin. *Polymer* 34(12):2602–2608.

Hu, Yuhang, Xuanhe Zhao, Joost J Vlassak, and Zhigang Suo. 2010. Using indentation to characterize the poroelasticity of gels. *Applied Physics Letters* 96(12).

Hudson, Christopher B. 1994. Gelatine—relating structure and chemistry to functionality. In *Food hydrocolloids: Structures, properties, and functions*, 347–354. Springer.

Hui, Chung-Yuen, Da-Ben Xu, and Edward J Kramer. 1992. A fracture model for a weak interface in a viscoelastic material (small scale yielding analysis). *Journal of applied physics* 72(8):3294–3304.

International, ASTM. 2016. Standard specification for rubber—concentrated, synthetic latex. ASTM Standard D1076-16. West Conshohocken, PA: ASTM International.

Jha, Anushka, Preetika Karnal, and Joelle Frechette. 2022. Adhesion of fluid infused silicone elastomer to glass. *Soft Matter* 18(39):7579–7592.

Johnson, Kenneth Langstreth. 1987. *Contact mechanics*. Cambridge university press.

Johnson, Kenneth Langstreth, Kevin Kendall, and aAD Roberts. 1971. Surface energy and the contact of elastic solids. *Proceedings of the royal society of London. A. mathematical and physical sciences* 324(1558):301–313.

Khakalo, Alexey, Ilari Filpponen, and Orlando J Rojas. 2017. Protein adsorption tailors the surface energies and compatibility between polylactide and cellulose nanofibrils. *Biomacromolecules* 18(4):1426–1433.

Kim, Jiho, and Alison C Dunn. 2020. Generalized rate-and-state model linking rheology and soft matter tribology. *Extreme Mechanics Letters* 41: 101013.

Knauss, W G. 1969. Stable and Unstable Crack Growth in Viscoelastic Media. *Transactions of the Society of Rheology* 13(3):291–313.

Knauss, Wolfgang G. 2015. A review of fracture in viscoelastic materials. *International Journal of Fracture* 196:99–146.

Kokol, Vanja, Yasir Beeran Pottathara, Mohor Mihelčič, and Lidija Slemenik Perše. 2021. Rheological properties of gelatine hydrogels affected by flow-and horizontally-induced cooling rates during 3d cryo-printing. *Colloids and Surfaces A: Physicochemical and Engineering Aspects* 616:126356.

Labonte, David, and Walter Federle. 2015. Rate-dependence of 'wet'biological adhesives and the function of the pad secretion in insects. *Soft Matter* 11(44):8661–8673.

Lai, Yang, Dongjing He, and Yuhang Hu. 2019. Indentation adhesion of hydrogels over a wide range of length and time scales. *Extreme Mechanics Letters* 31:100540.

Lai, Yang, and Yuhang Hu. 2021. The relation between adhesion properties and network properties of hydrogels: A study based on an indentation adhesion method. *Mechanics of Materials* 159:103877.

Lake, Graham J, and Allen G Thomas. 1967. The strength of highly elastic materials. *Proceedings of the Royal Society of London. Series A. Mathematical and Physical Sciences* 300(1460):108–119.

Lakes, Roderic S. 2009. *Viscoelastic materials*. Cambridge university press.

Lee, Wonhyeok, and Melih Eriten. 2023. Real area of contact and tractions on the patterned surfaces generated by spinodal decomposition and amplified instability. *Frontiers in Mechanical Engineering* 9:1253207.

———. 2024. Poroviscoelastic relaxations and rate-dependent adhesion in gelatin. *Soft Matter* 20(23):4583–4590.

Lengiewicz, Jakub, Mariana de Souza, Mohamed A Lahmar, Cédric Courbon, Davy Dalmas, Stanislaw Stupkiewicz, and Julien Scheibert. 2020. Finite deformations govern the anisotropic shear-induced area reduction of soft elastic contacts. *Journal of the Mechanics and Physics of Solids* 143: 104056.

Li, Jianyu, AD Celiz, J Yang, Q Yang, I Wamala, W Whyte, BR Seo, NV Vasilyev, JJ Vlassak, Z Suo, et al. 2017a. Tough adhesives for diverse wet surfaces. *Science* 357(6349):378–381.

Li, Jianyu, Widusha RK Illeperuma, Zhigang Suo, and Joost J Vlassak. 2014. Hybrid hydrogels with extremely high stiffness and toughness. *ACS Macro Letters* 3(6):520–523.

Li, Ningbo, Sarocha Prodyawong, Zhongqi He, Xiuzhi S Sun, and Donghai Wang. 2017b. Effect of drying methods on the physicochemical properties and adhesion performance of water-washed cottonseed meal. *Industrial Crops and Products* 109:281–287.

Liu, Lejie, Karthik Yerrapragada, Corinne R Henak, and Melih Eriten. 2022. Contact nonlinearity in indenter-foam dampers. *Journal of Vibration and Acoustics* 144(5):051003.

Liu, Zheyu, Hongyu Lu, Yelong Zheng, Dashuai Tao, Yonggang Meng, and Yu Tian. 2018. Transient adhesion in a non-fully detached contact. *Scientific reports* 8(1):6147.

Ma, Hui, Zhenyu Liu, Xingqi Lu, Shengting Zhang, Chenlong Tang, Yifan Cheng, Hui Zhang, Guangli Liu, Cong Sui, Chengbiao Ding, et al. 2024. 3d printed multi-coupled bioinspired skin-electronic interfaces with enhanced adhesion for monitoring and treatment. *Acta Biomaterialia* 187:183–198.

Maghami, Ali, Qingao Wang, Michele Tricarico, Michele Ciavarella, Qunyang Li, and Antonio Papangelo. 2024. Bulk and fracture process zone contribution to the rate-dependent adhesion amplification in viscoelastic broad-band materials. *Journal of the Mechanics and Physics of Solids* 193: 105844.

Mandriota, Cosimo, Nicola Menga, and Giuseppe Carbone. 2024. Enhancement of adhesion strength in viscoelastic unsteady contacts. *Journal of the Mechanics and Physics of Solids* 192:105826.

Maugis, D, and M Barquins. 1978. Fracture mechanics and the adherence of viscoelastic bodies. *Journal of Physics D: Applied Physics* 11(14):1989.

Maugis, Daniel. 1992. Adhesion of spheres: the jkr-dmt transition using a dugdale model. *Journal of colloid and interface science* 150(1):243–269.

McCartney, LN. 1977. Crack propagation, resulting from a monotonic increasing applied stress, in a linear viscoelastic material. *International Journal of Fracture* 13:641–654.

McGhee, Eric O., Samuel M. Hart, Juan Manuel Urueña, and W. Gregory Sawyer. 2019. Hydration Control of Gel-Adhesion and Muco-Adhesion. *Langmuir* 35(48):15769–15775.

Meier, Yuki A, Kaihuan Zhang, Nicholas D Spencer, and Rok Simic. 2019. Linking friction and surface properties of hydrogels molded against materials of different surface energies. *Langmuir* 35(48):15805–15812.

Michalska-Sionkowska, Marta, Oliwia Warżyńska, Beata Kaczmarek-Szczepańska, Krzysztof Łukowicz, Anna Maria Osyczka, and Maciej Walczak. 2021. Preparation and characterization of fish skin collagen material modified with β-glucan as potential wound dressing. *Materials* 14(6):1322.

Michel, Raphaël, Léna Poirier, Quentin van Poelvoorde, Josette Legagneux, Mathieu Manassero, and Laurent Corté. 2019. Interfacial fluid transport is a key to hydrogel bioadhesion. *Proceedings of the National Academy of Sciences* 116(3):738–743.

Mindlin, Raymond David. 1949. Compliance of elastic bodies in contact. *JOURNAL OF APPLIED MECHANICS*.

Misra, Anil, and Shiping Huang. 2011. Effect of loading induced anisotropy on the shear behavior of rough interfaces. *Tribology International* 44(5):627–634.

Mitchell, JR. 1980. The rheology of gels. *Journal of Texture studies* 11(4): 315–337.

Müller, C, and MH Müser. 2023. How short-range adhesion slows down crack closure and contact formation. *The Journal of Chemical Physics* 159(23).

Müser, Martin H, and Bo NJ Persson. 2022. Crack and pull-off dynamics of adhesive, viscoelastic solids. *Europhysics Letters* 137(3):36004.

Naassaoui, Imen, Olivier Ronsin, and Tristan Baumberger. 2018. A poroelastic signature of the dry/wet state of a crack tip propagating steadily in a physical hydrogel. *Extreme Mechanics Letters* 22:8–12.

Nam, Sungmin, Junzhe Lou, Sangmin Lee, Jan-Marc Kartenbender, and David J Mooney. 2024. Dynamic injectable tissue adhesives with strong

adhesion and rapid self-healing for regeneration of large muscle injury. *Biomaterials* 309:122597.

Nia, Hadi Tavakoli, Iman S Bozchalooi, Yang Li, Lin Han, Han-Hwa Hung, Eliot Frank, Kamal Youcef-Toumi, Christine Ortiz, and Alan Grodzinsky. 2013. High-bandwidth afm-based rheology reveals that cartilage is most sensitive to high loading rates at early stages of impairment. *Biophysical journal* 104(7):1529–1537.

Normand, Valéry, and Jean-Claude Ravey. 1997. Dynamic study of gelatin gels by creep measurements. *Rheologica acta* 36:610–617.

Northrop, John H, and M Kunitz. 1926. The swelling pressure of gelatin and the mechanism of swelling in water and neutral salt solutions. *The Journal of General Physiology* 10(1):161–177.

Ohmori, T. 1989. Collective diffusion coefficient in polyacrylamide gels. *Kobunshi Ronbunshu* 46:639–641.

Ottone, Mariel L, Marta B Peirotti, and Julio A Deiber. 2005. Modeling the rheology of gelatin gels for finite deformations. part 2. viscoelastic solid model. *Polymer* 46(13):4938–4949.

Papangelo, Antonio. 2021. On the effect of shear loading rate on contact area shrinking in adhesive soft contacts. *Tribology letters* 69(2):48.

Papangelo, Antonio, J Scheibert, R Sahli, G Pallares, and Michele Ciavarella. 2019. Shear-induced contact area anisotropy explained by a fracture mechanics model. *Physical Review E* 99(5):053005.

Penke, Brigita, Stephen Kinsey, Stephen J Gibbs, Timothy S Moerland, and Bruce R Locke. 1998. Proton diffusion andt1relaxation in polyacrylamide gels: A unified approach using volume averaging. *Journal of magnetic resonance* 132(2):240–254.

Persson, BNJ. 2017. Crack propagation in finite-sized viscoelastic solids with application to adhesion. *Europhysics Letters* 119(1):18002.

———. 2021. On opening crack propagation in viscoelastic solids. *Tribology Letters* 69(3):115.

Persson, BNJ, and EA Brener. 2005. Crack propagation in viscoelastic solids. *Physical Review E—Statistical, Nonlinear, and Soft Matter Physics* 71(3):036123.

Persson, Bo NJ. 1998. On the theory of rubber friction. *Surface science* 401(3):445–454.

Persson, Bo NJ, and Erio Tosatti. 2013. *Physics of sliding friction*, vol. 311. Springer Science & Business Media.

Poppe, Jan. 1992. Gelatin thickening and gelling agents for food. *London: Blackie Academic and Professional*.

Pradhan, A, MH Müser, N Miller, JP Abdelnabe, L Afferrante, and D Albertini. 2025. The surface-topography challenge: A multi-laboratory benchmark study to advance the characterization of topography. *Tribol. Lett.*(*submitted*).

Reale, Erik R, and Alison C Dunn. 2017. Poroelasticity-driven lubrication in hydrogel interfaces. *Soft matter* 13(2):428–435.

Rockwell, Paige N, James E Maneval, Brandon M Vogel, and Erin L Jablonski. 2023. Water diffusion and uptake in injectable ettmp/pegda hydrogels. *The Journal of Physical Chemistry B* 127(22):5055–5061.

Ross-Murphy, SB. 1991. Incipient behaviour of gelatin gels. *Rheologica Acta* 30:401–411.

Ross-Murphy, Simon B. 1992. Structure and rheology of gelatin gels: recent progress. *Polymer* 33(12):2622–2627.

Rubinstein, Shmuel M, Gil Cohen, and Jay Fineberg. 2004. Detachment fronts and the onset of dynamic friction. *Nature* 430(7003):1005–1009.

Ruina, Andy. 1983. Slip instability and state variable friction laws. *Journal of Geophysical Research: Solid Earth* 88(B12):10359–10370.

Sahli, R, G Pallares, A Papangelo, M Ciavarella, C Ducottet, N Ponthus, and J Scheibert. 2019. Shear-induced anisotropy in rough elastomer contact. *Physical Review Letters* 122(21):214301.

Sauer, Roger A. 2016. A survey of computational models for adhesion. *The Journal of Adhesion* 92(2):81–120.

Saulnier, F, Thierry Ondarçuhu, A Aradian, and Elie Raphaël. 2004. Adhesion between a viscoelastic material and a solid surface. *Macromolecules* 37(3):1067–1075.

Savkoor, AR, and GAD0364 Briggs. 1977. The effect of tangential force on the contact of elastic solids in adhesion. *Proceedings of the Royal Society of London. A. Mathematical and Physical Sciences* 356(1684):103–114.

Savkoor, Arvin R. 1992. Models of friction based on contact and fracture mechanics. In *Fundamentals of friction: macroscopic and microscopic processes*, 111–133. Springer.

Schallamach, A. 1963. A theory of dynamic rubber friction. *Wear* 6(5): 375–382.

Schapery, RA. 1989. On the mechanics of crack closing and bonding in linear viscoelastic media. *International Journal of Fracture* 39:163–189.

Schapery, Richard A. 1975. A theory of crack initiation and growth in viscoelastic media: I. theoretical development. *International Journal of fracture* 11:141–159.

Schulze, Kyle D, Samuel M Hart, Samantha L Marshall, Christopher S O'Bryan, Juan M Urueña, Angela A Pitenis, W Gregory Sawyer, and

Thomas E Angelini. 2017. Polymer osmotic pressure in hydrogel contact mechanics. *Biotribology* 11:3–7.

Serrano, Francisco Javier Cedano. 2019. From molecular architecture and electrostatic interactions to underwater adherence of hydrogels. Ph.D. thesis, Sorbonne université.

Shen, Tong, and Franck J Vernerey. 2020. Rate-dependent fracture of transient networks. *Journal of the Mechanics and Physics of Solids* 143: 104028.

Shintake, Jun, Vito Cacucciolo, Dario Floreano, and Herbert Shea. 2018. Soft robotic grippers. *Advanced materials* 30(29):1707035.

Shoaib, Tooba, and Rosa M Espinosa-Marzal. 2018. Insight into the viscous and adhesive contributions to hydrogel friction. *Tribology Letters* 66(3):96.

Shoaib, Tooba, Joerg Heintz, Josue A Lopez-Berganza, Raymundo Muro-Barrios, Simon A Egner, and Rosa M Espinosa-Marzal. 2018. Stick–slip friction reveals hydrogel lubrication mechanisms. *Langmuir* 34(3):756–765.

Shui, Langquan, Laibing Jia, Hangbo Li, Jiaojiao Guo, Ziyu Guo, Yilun Liu, Ze Liu, and Xi Chen. 2020. Rapid and continuous regulating adhesion strength by mechanical micro-vibration. *Nature communications* 11(1): 1583.

Smith, Andrew M, and James A Callow. 2006. *Biological adhesives*, vol. 23. Springer.

Tabor, D. 1977. Surface forces and surface interactions. In *Plenary and invited lectures*, 3–14. Elsevier.

Tricarico, Michele, Michele Ciavarella, and Antonio Papangelo. 2025. Enhancement of adhesion strength through microvibrations: Modeling and experiments. *Journal of the Mechanics and Physics of Solids* 196:106020.

Vandenberghe, Els, MN Charalambides, IK Mohammed, Bart De Ketelaere, Josse De Baerdemaeker, and Johan Claes. 2017. Determination of a critical stress and distance criterion for crack propagation in cutting models of cheese. *Journal of Food Engineering* 208:1–10.

VanDonselaar, Kurt R, Daniel A Bellido-Aguilar, Maryam Safaripour, Hyemin Kim, James J Watkins, Alfred J Crosby, Dean C Webster, and Andrew B Croll. 2023. Silicone elastomers and the persson-brener adhesion model. *The Journal of Chemical Physics* 159(18).

Violano, G, A Chateauminois, and L Afferrante. 2021a. Rate-dependent adhesion of viscoelastic contacts, part i: Contact area and contact line velocity within model randomly rough surfaces. *Mechanics of Materials* 160:103926.

Violano, Guido, and Luciano Afferrante. 2022. Size effects in adhesive contacts of viscoelastic media. *European Journal of Mechanics-A/Solids* 96: 104665.

Violano, Guido, Antoine Chateauminois, and Luciano Afferrante. 2021b. A jkr-like solution for viscoelastic adhesive contacts. *Frontiers in Mechanical Engineering* 7:664486.

Wahl, K.J., S.A.S. Asif, J.A. Greenwood, and K.L. Johnson. 2006. Oscillating adhesive contacts between micron-scale tips and compliant polymers. *Journal of Colloid and Interface Science* 296(1):178–188.

Wang, Ruican, and Richard W Hartel. 2022. Confectionery gels: Gelling behavior and gel properties of gelatin in concentrated sugar solutions. *Food Hydrocolloids* 124:107132.

Wang, Zhongchao, Xiao Han, Weiwei Xiao, Pin Wang, Jinghan Wang, Dan Zou, Xiao Luo, Liang Shi, Jiaqi Wu, Ling Guo, et al. 2024. Mussel-inspired adhesive drug-loaded hydrogels for oral ulcers treatment. *Acta Biomaterialia* 187:98–109.

Williams, Malcolm L, Robert F Landel, and John D Ferry. 1955. The temperature dependence of relaxation mechanisms in amorphous polymers and other glass-forming liquids. *Journal of the American Chemical society* 77(14):3701–3707.

Winter, H Henning, and Francois Chambon. 1986. Analysis of linear viscoelasticity of a crosslinking polymer at the gel point. *Journal of rheology* 30(2):367–382.

Winter, HH. 1987. Evolution of rheology during chemical gelation. In *Permanent and transient networks*, 104–110. Springer.

———. 2001. Physical and chemical gelation. *Encyclopedia of materials: science and technology* 6991–6999.

Wisotzki, Emilia I, Paolo Tempesti, Emiliano Fratini, and Stefan G Mayr. 2017. Influence of high energy electron irradiation on the network structure of gelatin hydrogels as investigated by small-angle x-ray scattering (saxs). *Physical Chemistry Chemical Physics* 19(19):12064–12074.

Wu, Sijin, Xuewei Zhou, Zhicheng Jin, and Haiming Cheng. 2023. Collagenases and their inhibitors: a review. *Collagen and Leather* 5(1):19.

Xu, Ke, Limeng Wang, Wangjie Shan, Ke Gao, Jiping Wang, Qi Zhong, and Wenlong Zhou. 2024. Highly stretchable and self-adhesive wearable biosensor based on nanozyme-catalyzed conductive hydrogels. *ACS Applied Polymer Materials* 6(4):2188–2200.

Yamamoto, Tetsurou, Takayuki Kurokawa, Jamil Ahmed, Gen Kamita, Shintaro Yashima, Yuichiro Furukawa, Yuko Ota, Hidemitsu Furukawa, and Jian Ping Gong. 2014. In situ observation of a hydrogel–glass interface during sliding friction. *Soft Matter* 10(30):5589–5596.

Yaqoob, MA, A Winogrodzka, HR Fischer, ERM Gelinck, MB De Rooij, and DJ Schipper. 2013. Pre-sliding behaviour of single asperity contact. *Tribology letters* 49:553–562.

Yengul, Sanjay S, Paul E Barbone, and Bruno Madore. 2019. Dispersion in tissue-mimicking gels measured with shear wave elastography and torsional vibration rheometry. *Ultrasound in medicine & biology* 45(2): 586–604.

Yerrapragada, K, D Chawla, CR Henak, and M Eriten. 2023. Fracture-induced acoustic emissions in gelatin. *Experimental Mechanics* 63(3): 485–494.

Yi, Jiawei, Wissem Haouas, Michaël Gauthier, and Kanty Rabenorosoa. 2024. A pdms/silicon adhesion control method at millimeter-scale based on microvibration. *Advanced Intelligent Systems* 2400394.

Yoshida, H, T Hatakeyama, and H Hatakeyama. 1993. Characterization of water in polysaccharide hydrogels by dsc. *Journal of Thermal Analysis and Calorimetry* 40(2):483–489.

Yoshimura, Keiji, Mariko Terashima, Daiki Hozan, Takahito Ebato, Yoshihiro Nomura, Yasuhiro Ishii, and Kunio Shirai. 2000. Physical properties of shark gelatin compared with pig gelatin. *Journal of agricultural and food chemistry* 48(6):2023–2027.

Yousefi-Mashouf, Hamid, Lucie Bailly, Laurent Orgéas, and Nathalie Henrich Bernardoni. 2023. Mechanics of gelatin-based hydrogels during finite strain tension, compression and shear. *Frontiers in Bioengineering and Biotechnology* 10:1094197.

Zhang, Teng, Hyunwoo Yuk, Shaoting Lin, German A Parada, and Xuanhe Zhao. 2017. Tough and tunable adhesion of hydrogels: experiments and models. *Acta Mechanica Sinica* 33:543–554.

Zhang, Xiaogang, Yali Zhang, and Zhongmin Jin. 2022. A review of the bio-tribology of medical devices. *Friction* 10(1):4–30.

Zhang, Zheng, Timothy Chao, and Shaoyi Jiang. 2008. Physical, chemical, and chemical- physical double network of zwitterionic hydrogels. *The Journal of Physical Chemistry B* 112(17):5327–5332.